UNIVERSITY OF CALIFORNIA SAN DIEGO

Physics of plasma transport and divertor detachment in novel divertor configurations

A dissertation submitted in partial satisfaction of the
requirements for the degree Doctor of Philosophy

in

Engineering Sciences (Mechanical Engineering)

by

Rebecca Lee Masline

Committee in charge:

Sergei I. Krasheninnikov, Chair
Farhat N. Beg
Patrick H. Diamond
Christopher G. Holland
George R. Tynan

2023

The Dissertation of Rebecca Lee Masline is approved, and it is acceptable in quality and form for publication on microfilm and electronically.

University of California San Diego

2023

DEDICATION

To Gordon Freeman

EPIGRAPH

Fusion: Imagine you have two big macs. You fuse them together to form a double BM. Since a double BM only have three slices of bread the extra piece of bread is the energy release.

— Anonymous, ID:KLq8yG6C No.257303284, 05/13/20, Sweden

TABLE OF CONTENTS

LIST OF FIGURES

LIST OF TABLES

ACKNOWLEDGEMENTS

To Professor Sergei I. Krasheninnikov, for everything. It is a strong testament to his unparalleled brilliance and exceptional patience that he has managed to extract anything coherent from me, let alone an entire dissertation. I look forward to spending my career continuing to crusade under the righteous banner of divertor physics.

To Professor Patrick H. Diamond, who introduced me to many complicated and wild subjects in the world of plasma physics and fluid mechanics. He has been patient and understanding of my deficiencies (me being an engineer), and has helped me develop my voice in scientific writing and nurtured my artistic skills through his brave and consistent patronage of my terrible Photoshop work.

To Dr. Andrei Kukushkin, who installed his personal version of the SOLPS 4.3 code for me and provided the wisdom to use it. Though my interaction with him was limited to me receiving his much-anticipated emails filled with answers to my silly questions, his positivity and optimism for the success of my project was the only thing that prevented me from quitting altogether when I thought it was impossible to continue, which happened many more times than I'd care to admit. He leaves behind a tremendous record of scientific work that has been hugely influential on me as a scientist and communicator. Every person who I have interacted with who has known this man corroborates everything I experienced - it is extremely rare to be universally loved and respected by so many, particularly in the often finicky field of fusion research. His influence on me and many others was profound, and he will be missed by many.

To everyone who put up with me before, during, and after the pandemic and made me so happy; in particular, my sweet little dog Valky, my lifelong friend Tara Hitchcock, the wonderful Dr. Oak Nelson, my brother Andrew "Ace" Masline and the Crimeboys, my kindred spirit in the fusion community Dr. Shawn Zamperini (who also brought me the amazing Jessica Flester), my support group of Dr. Sam Frank and Dr. Sara Ferry, Alexey Knyazev and Dr. Robin Heinonen and whatever they consider to be a sandwich, and my dear friend Michael Bergmann - who has, by no fault of his own, managed to only appear and reappear in my life during spells of my personal drama and chaos, and yet, despite my grumpiness, never abandoned me: you are truly one of my most cherished friends, and thank you for always being there for me. You can have all the brain cells now, I will no longer be needing them.

And of course, lastly, to my parents, without whom I would not be possible, and to Bonnia Ewing, my Grammy, whose self-awareness, practicality, and sharp wit inspire me always. I am so proud to write our shared name on this document.

Chapters 1 and 2, in part, appeared as a part of a series of lecture notes prepared for the PHYS 218C course taught by Professor Patrick H. Diamond at UC San Diego in Spring 2021. The dissertation author was the author of this material.

Chapter 4, in part, is a reprint of the material as it appears in "Influence of the inverse sheath on divertor plasma performance in tokamak edge plasma simulations" in *Contributions to Plasma Physics*, 60(5-6), p.e201900097 by R. Masline, R.D. Smirnov, and S.I. Krasheninnikov (2020), and in "Simulations of divertor plasmas with inverse sheaths" in *Physics of Plasmas*, 27(9), p.092505 by R. Masline, R.D. Smirnov, and S.I. Krasheninnikov (2020). The dissertation author was the primary investigator and author of this material.

Chapter 5, in full, is a reprint of the material as it appears in "Energy and particle balance during plasma detachment in a long-leg configuration", in *Nuclear Fusion*, 63 066017 by R. Masline and S.I. Krasheninnikov (2023). The dissertation author was the primary investigator and author of this material.

Chapter 6, in full, has been submitted for publication of the material as it may appear in "Mechanisms behind impurity spreading in a channeled, long-leg divertor configuration", submitted to *Physics of Plasmas* by R. Masline and S.I. Krasheninnikov (March 2023). The dissertation author was the primary investigator and author of this material.

This work was supported by the U.S. Department of Energy, Office of Science, Office of Fusion Energy Sciences under Award No. DE-FG02-04ER54739 at UCSD.

VITA

2018	Bachelor of Science, Chemical Engineering, *magna cum laude* University of California San Diego
2020	Master of Science, Engineering Sciences (Mechanical Engineering) University of California San Diego
2019–2021	Teaching Assistant, Dept. of Mechanical and Aerospace Engineering University of California San Diego
2018–2023	Graduate Student Researcher, Dept. of Mechanical and Aerospace Engineering University of California San Diego
2023	Doctor of Philosophy, Engineering Sciences (Mechanical Engineering) University of California San Diego

PUBLICATIONS

R. Masline and S.I. Krasheninnikov, "Mechanisms behind impurity spreading in a channeled, long-leg divertor configuration." Submitted to *Physics of Plasmas*, March 2023.

R. Masline and S.I. Krasheninnikov, "Energy and particle balance during plasma detachment in a long-leg divertor configuration." *Nuclear Fusion*, 63(6), p.066017 (2023).

R. Masline, I. Bykov, R.A. Moyer, A. Wingen, J. Guterl, D. Rudakov, W.R. Wampler, H.Q. Wang, J.G. Watkins, and D.M. Orlov. "Misalignment of magnetic field in DIII-D assessed by post-mortem analysis of divertor targets." *Nuclear Fusion*, 63(1), p.016012 (2023).

R. Masline, R.D. Smirnov, and S.I. Krasheninnikov. "Simulations of divertor plasmas with inverse sheaths." *Physics of Plasmas*, 27(9), p.092505 (2020).

Y. Zhang, S.I. Krasheninnikov, **R. Masline**, R.D. Smirnov. "Neutral impact on anomalous edge plasma transport and its correlation with divertor plasma detachment." *Nuclear Fusion*, 60(10), p.106023 (2020).

R. Masline, R.D. Smirnov, and S.I. Krasheninnikov. "Influence of the inverse sheath on divertor plasma performance in tokamak edge plasma simulations." *Contributions to Plasma Physics*, 60(5-6), p.e201900097 (2020).

J.G. Watkins, H.Q. Wang, J.L. Barton, A. Wingen, D. Pace, A. Moser, I. Bykov, **R. Masline**, D.M. Thomas, and H.Y. Guo. "Toroidal variation of the strike point in DIII-D." *Nuclear Materials and Energy*, 18, pp.46-49 (2019).

ABSTRACT OF THE DISSERTATION

Physics of plasma transport and divertor detachment in novel divertor configurations

by

Rebecca Lee Masline

Doctor of Philosophy in Engineering Sciences (Mechanical Engineering)

University of California San Diego, 2023

Sergei I. Krasheninnikov, Chair

In this dissertation, we investigate two proposed features aimed at improving the performance of the divertor exhaust system in tokamak nuclear fusion devices. Specifically, we assess the influence of the "inverse" plasma sheath and long-leg divertor configurations on the divertor plasma using numerical simulations. First, we investigate the "inverse" plasma sheath, which has been suggested to prevent the flow of ions to the wall and promote divertor detachment. We use the UEDGE code to simulate the physics of both the inverse and standard (Bohm) sheath regime at the divertor targets. Our results show

little difference in the overall plasma state, but an increase in electron heat flux to the divertor targets. Additionally, we observe a bifurcation behavior related to plasma recombination effects, and present an analytical model of this behavior. Second, we evaluate the long outer divertor leg, which is designed to increase volumetric dissipation, enhance turbulence spreading, and extend the distance between the material surface and the fragile core plasma. Using the SOLPS4.3 code, we assess the transition to the detached divertor regime, with scans on plasma density, transport coefficients, and multiple impurity species. Our results show a significant contribution to the energy balance from cross-field transport to the side walls and considerable recycling of impurities along the long leg, enabling delocalization of the radiated heat flux. Overall, this dissertation provides important insights into the physics associated with these proposed divertor features. The results suggest that the inverse plasma sheath may not have a significant impact on divertor plasma detachment, while the long-leg divertor configuration has potential to improve divertor performance by reducing impurity radiation localization and enhancing energy dissipation through cross-field transport. These findings contribute to the ongoing efforts to develop more efficient and effective divertor exhaust systems for tokamak fusion devices.

Chapter 1

Introduction

1.1 Magnetic confinement fusion

An ever-growing demand for energy and concerns with climate change have emphasized the need for clean sources of energy. One such path to this goal is through nuclear fusion, a process by which energy is released when two small atoms are fused together to form a single, heavier nucleus. For this process to happen, since each nucleus is positively charged, the kinetic energy of the particles must be large enough to overcome the strong repulsive electric forces from the interaction of the positive nuclei. Such a process requires a fuel to be subjected to high temperatures and pressures, which are often difficult to achieve on Earth. A method to achieve these conditions to harness the energy of the nuclear fusion process takes advantage of the property that material exposed to such high temperatures will be stripped of electrons and form plasma - in this case, a quasi-neutral, fluid-like collective of positively charged ions and negatively charged electrons. These charged particles can be manipulated and confined by via the Lorentz force by applying strong external magnetic fields to the plasma, an approach known as "magnetic confinement". This external magnetic field, when applied in a toroidal configuration, improves particle confinement; a tokamak is a toroidally symmetric device with an (ideally [1]) axisymmetric toroidal magnetic field designed to apply this technique.

A tokamak is a toroidal (donut-shaped) magnetic confinement device for plasma, first conceptualized by Andrei Sakharov and Igor Tamm in the 1950s. The word "tokamak" comes from a Russian acronym of the description of the device, transliterated to English as "**to**roidal'naya **ka**mera s **ma**gnitnymi **k**atushkami",

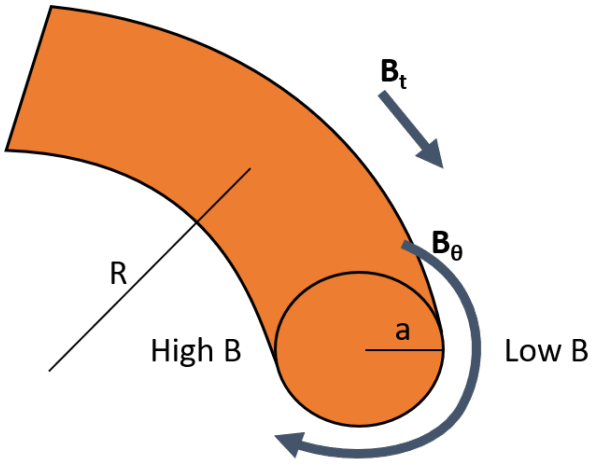

Figure 1.1. The geometry and fields of a tokamak device.

meaning "toroidal chamber with magnetic coils". The geometry of a tokamak is shown in Figure 1.1. A typical tokamak has an aspect ratio R/a of ∼3-4. The tokamak has a strong, externally applied toroidal field B_t, which is stronger on the inside and weaker on the outside. This inhomogeneity in the field strength is important because particles can be magnetically trapped, allowing them to oscillate around the closed magnetic field lines until they (hopefully) fuse and release energy. A poloidal field B_θ results from current; the source of this current can be inductive, from a transformer, non-inductive current drive, or the "bootstrap", ∇P-driven (self) current from the plasma. The toroidal field B_t is always much stronger than the poloidal field B_θ.

Developing a tokamak device requires facing many complex engineering challenges, as harnessing the fusion process is much more complicated than simply "plasma + magnetic field". A tokamak requires a complex system of magnetic coils (both in toroidal and poloidal dimensions), high-precision diagnostics to assess plasma performance, external heating systems to initiate the reaction, structural elements that must withstand the extreme magnetic forces during plasma discharges, and myriad other factors that contribute to the complexity of "unlocking" fusion as a viable source of energy [2]. The vessel used to confine this fuel must withstand the extreme conditions of the fusion reaction; although the fuel is isolated in a vacuum chamber and embedded into the strong magnetic field, the confinement of the fusion fuel is still not perfect. Material surfaces are exposed to constant bombardment from particles that travel across the closed magnetic field lines, either through "classical" collisional transport that knocks particles and energy from their paths along the field lines or associated with electromagnetic fluctuations driven by

various plasma instabilities. This "anomalous" plasma leakage impinges upon the vessel walls and can erode the material surfaces, causing damage (which can require time-consuming and costly replacement) and releasing material particles that can penetrate the core plasma. The fusion-grade plasma is fragile, and sensitive to the presence of these impurities (which can be any non-hydrogenic species), since impurities are strong radiators that can cool the plasma and quench the fusion reaction entirely. As such, protection of these material surfaces is essential; to do this, the temperature in the vicinity of the target must be below the erosion threshold of ~ 1 eV, while the core plasma must remain at $\sim 10^4$ eV to maintain a decent rate of fusion reactions. In a tokamak, this requirement is facilitated by the use of a magnetic divertor, where special magnetic coils are used to divert the magnetic field lines at the edge of the fusion device away from the core plasma and into some partially closed volume. Here, the plasma can be cooled to acceptable temperatures, while preventing impurities from traveling back into the core plasma. The divertor is the subject of this work, which will focus on using computer simulations to understand the underlying physics behind two novel techniques that have been proposed as possible methods to enhance the protection of material surfaces in the divertor.

Chapter 1, in part, appeared as a part of a series of lecture notes prepared for the PHYS 218C course taught by Professor Patrick H. Diamond at UC San Diego in Spring 2021. The dissertation author was the author of this material.

1.2 Outline of the dissertation

1.2.1 Summary

In this dissertation, we investigate two proposed features aimed at improving the performance of the divertor exhaust system in tokamak nuclear fusion devices. After introducing some essential physics of the edge and divertor plasmas relevant for this work (Chapters 2 and 3), we assess the influence of the "inverse" plasma sheath (Chapter 4) and long-leg divertor configurations on the divertor plasma using numerical simulations (Chapters 5 and 6). We investigate the "inverse" plasma sheath, which has been suggested to prevent the flow of ions to the wall and promote divertor detachment. We use the UEDGE code to simulate the physics of both the inverse and standard (Bohm) sheath regime at the divertor targets. Our results show little difference in the overall plasma state, but an increase in electron heat flux to

the divertor targets. Additionally, we observe a bifurcation behavior related to plasma recombination effects, and present an analytical model of this behavior. Next, we evaluate the physics of the long outer divertor leg, which is designed to increase volumetric dissipation, enhance turbulence spreading, and extend the distance between the material surface and the fragile core plasma. Using the SOLPS4.3 code, we assess the transition to the detached divertor regime, with scans on plasma density, transport coefficients, and multiple impurity species. Our results show a significant contribution to the energy balance from cross-field transport to the side walls and considerable recycling of impurities along the long leg, enabling delocalization of the radiated energy from the impurity. Overall, this dissertation provides important insights into the physics associated with these proposed divertor features. The results suggest that the inverse plasma sheath may not have a significant impact on divertor plasma detachment, while the long-leg divertor configuration has potential to improve divertor performance by reducing impurity radiation localization and enhancing energy dissipation through cross-field transport. These findings contribute to the ongoing efforts to develop more efficient and effective divertor exhaust systems for tokamak fusion devices.

1.2.2 Chapter 2: Tokamak edge plasma

In this section, we will discuss some phenomena seen in edge plasmas that is relevant to the thesis. The problem of plasma material interactions is introduced, and the physics of the plasma sheath and its influence on the edge plasma are briefly explained. The tokamak divertor is described, and the detachment of the divertor plasma is discussed, including the "high-recycling" regime, the fundamental physics underlying the process of detachment, and physical manifestations of plasma detachment. Several alternative divertor configurations, which are magnetic configurations with novel features relative to standard divertor configurations, are introduced, and the supposed benefits of these novel improvements are addressed.

1.2.3 Chapter 3: Modeling the SOL

Some of the (many) fundamental assumptions and limitations made in plasma edge modeling are described. The formulation and basis for the fluid model of the edge plasma is detailed, as well as some of the corrections for some plasma phenomena that are not described by the fundamental equations. The various treatments for neutral particles and impurity radiation are described, and the two different edge

modeling software packages (UEDGE and SOLPS) shown in this work are presented. Further details about the fundamental equations solved by these codes is provided in Appendix A and Appendix B.

1.2.4 Chapter 4: Simulations of divertor plasmas with inverse sheaths

Recently, it was proposed that under the presence of strong secondary electron emission, an "inverse sheath" could form at the plasma edge, a regime with a monotonic positive potential at the material surface that would block incoming ion flux from hitting the target [3, 4]. This was suggested as a novel mechanism for protecting material surfaces, since ion flux would be repelled away from the material surface and the emission of secondary electrons could provide a cooling effect to the divertor plasma [5]. Effects of this regime were investigated in a DIII-D-like configuration using the UEDGE code with modified boundary conditions at the plasma edge to emulate the physics of the inverse sheath. An analytical description of a bifurcation observed in the solution set is described.

1.2.5 Chapter 5: Energy and particle balance in a long-leg divertor configuration

It is feasible that long divertor legs, designed to optimize volumetric losses, could be subject to complications resulting from cross-field anomalous transport in the long divertor leg, the physics of which is not yet fully understood. Cross-field particle transport in divertor legs is known to be prevalent in both conventional and alternative divertor configurations, but the full scope of the impact of this transport is still unclear [6]. Simulations offer powerful tools to assess detachment phenomena, as many of the important factors contributing to the achievement of the detached regime and the factors contributing to its stability are control parameters in the simulation space, allowing for different physics mechanisms to be targeted and directly assessed. We have used the high-fidelity SOLPS4.3 code to follow the approaches of [7, 8] with more robust analysis and more developed numerical modeling techniques to fully and thoroughly assess the physics of the detached divertor regime in long-leg divertor configurations, with considerable focus on the spreading of radiation across the leg and the impact of anomalous transport in the long leg, to investigate this phenomenon.

1.2.6 Chapter 6: Mechanisms behind impurity spreading in a channeled, long-leg divertor configuration

Since divertor detachment has a strong dependence on impurity radiation and volumetric plasma recombination, there has been considerable research effort devoted to optimizing these dissipative processes. These processes are, in and of themselves, highly intertwined, since higher power dissipation from more effective impurity radiation can improve the efficiency of recombination processes by allowing for access to lower temperatures, which has emphasized the vital importance of impurity radiation on power dissipation and divertor detachment [9]. Ideally, this impurity radiation should not reduce the confinement in the core plasma, avoid contamination of the core plasma with impurities, and avoid dangerous concentrated, local heating of plasma-facing materials by spreading out the area of the radiation region. From this perspective, long leg divertors are desirable because they will increase the distance between the divertor targets and core plasma, as the impurity radiation region could be spread across the full divertor leg and away from the X-point. However, experimental data from AUG and JET show that impurity radiation is usually strongly localized to the X-point and outer divertor target [10, 11], which is not suitable for reactor conditions. Numerical simulations have indicated a more favorable distribution of radiation along the long leg divertors [7, 8]. The simulations shown in [7] showed a spread in both impurity and neutral radiation loss across the leg, indicating the possibility that the radiation spread could be due to strong plasma recycling to the side walls, but the physical reason for this phenomenon was not investigated and remains unclear. In this section, we repeat similar simulations to those shown in Chapter 5, but with fixed deuterium particle count and varying impurity content, performing a scan with neon and a scan with nitrogen, to assess impurity radiation distribution and spread along the long divertor leg.

Chapter 2

Tokamak edge plasma

A major area of study in magnetic fusion devices is the complex and multifaceted edge plasma, and despite many years of extensive study, there are significant gaps in the understanding of the physics in nearly every aspect of this region. Study of the physics of the edge plasma is primarily focused on two key areas of research: the management of heat and particle fluxes exhausted from the core plasma (including protection of first-wall, plasma facing materials), and maintaining good confinement of the plasma core. This work will focus on the physics of managing the heat and particle exhaust from the core plasma and the protection of the plasma facing materials from these harsh conditions.

The geometry of the tokamak is shown in Figure 2.1. The axis of symmetry for the torus is on the left. The solid black line represents the first wall of the tokamak. Both the toroidal magnetic field (B_ϕ) and toroidal current density (J_ϕ) are both into the paper. The yellow, green, and thick dark purple lines in the figure are magnetic flux surfaces. The yellow lines are closed magnetic flux surfaces, while the green lines are open magnetic flux surfaces that peel away from the plasma and touch the divertor target or the walls of the device. The thick purple line is the last closed flux surface (LCFS), or the "separatrix", that separates the regions of open and closed magnetic field lines that has a null point where it crosses itself, called the X-point. This X-point is formed by special poloidal field coils, called shaping coils. These poloidal field coils run a current through the coil that is parallel to the main plasma current, which creates a null in the magnetic field at the X-point. At this point, the poloidal field vanishes, and there is finite poloidal field throughout the rest of the system. There can be one X-point at the bottom or the top of the device, two X-points at the top and bottom, or multiple X-points throughout the device. The plasma

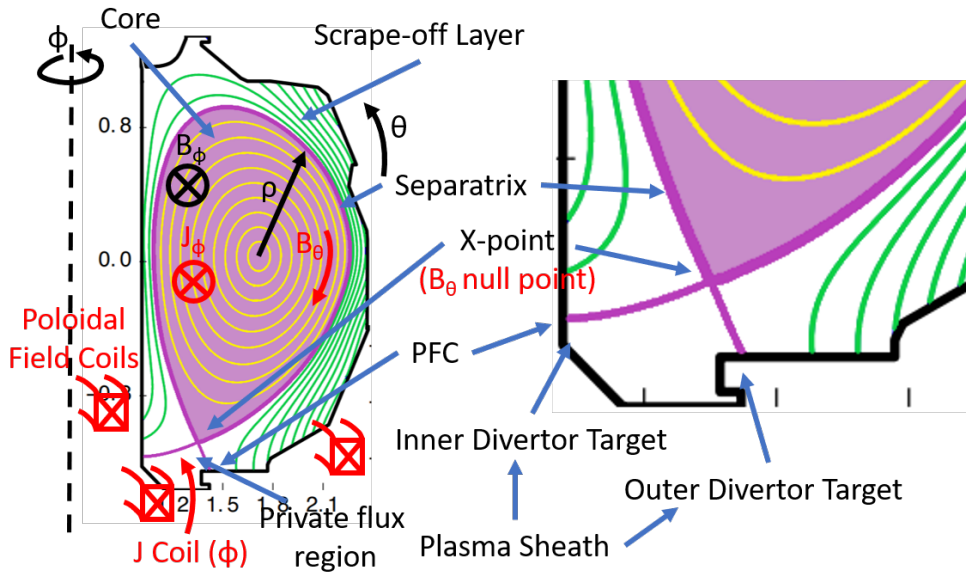

Figure 2.1. Cartoon of a tokamak plasma, focusing on the edge region. The plasma is in purple, the vacuum is white, and the material surfaces are shown in the black outline. Red annotations denote magnetics, while black annotations denote coordinates. Closed field lines are shown in yellow, open field lines are shown in green, and the last closed flux surface (separatrix) is shown in dark purple.

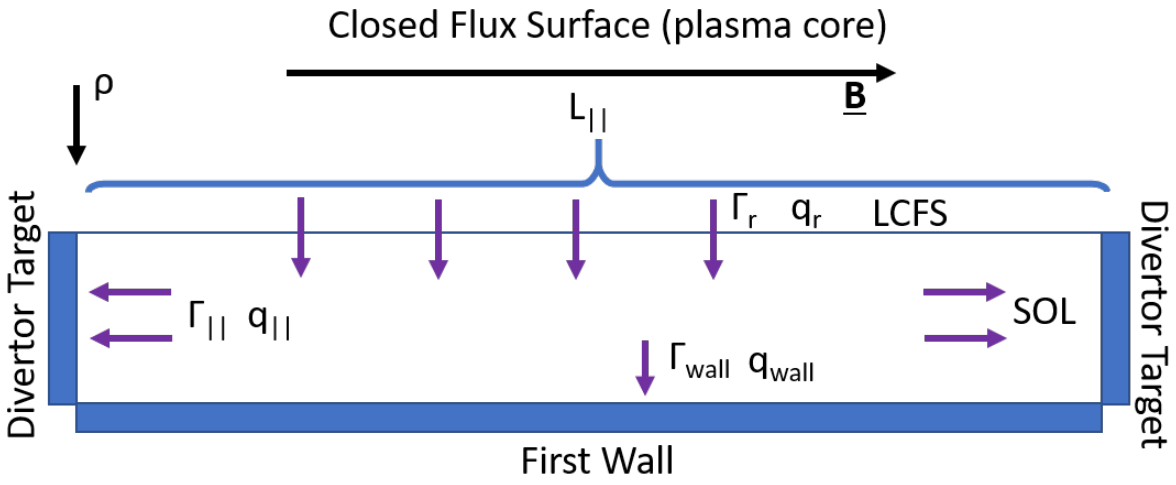

Figure 2.2. Alternative view of the last-closed flux surface, core, and SOL, where the edge of the plasma has been "peeled off" the tokamak and flattened into new coordinates. These new coordinates show the poloidal direction as the horizontal axis and the radial direction as the vertical axis. The field line terminates at each of the two divertor targets. Fluxes are drawn as purple arrows.

can be shaped, stretched, and pulled into these different shapes for different reasons, often to improve magnetohydrodynamic stability or heat dissipation.

The open field lines that intersect the material surfaces form what is called the "scrape-off layer", or "SOL", which is all the plasma in the region outside of the last closed flux surface ("LCFS"). The scrape-off layer region encompasses the area where the plasma interacts with material surfaces, which include the divertor targets and the walls of the machine. In this region, the interactions between the intense plasma and the material surface are complex - the materials themselves can influence the behavior of the plasma, and the plasma also has an effect on the materials.

The geometry of the SOL is intricate, and a simplified version is shown in Figure 2.2. This structure shows the polodial direction as the horizontal axis, and the radial direction as the vertical axis, as though the SOL were "peeled off" the poloidal section and flattened out, from divertor target to divertor target. The symbol ρ is the normalized magnetic flux, going from 0 at the magnetic axis to 1 at the LCFS. The boundaries are defined by the divertor targets in the poloidal/horizontal direction, and the LCFS at the upper boundary and the first wall at the lower boundary in the vertical direction. Between these regions is

the SOL.

Plasma ionization and plasma heating usually occur in the core. This creates an influx of particles and heat from the core plasma into the SOL, γ_r and q_r, respectively. The core plasma is fueling the scrape off layer across the LCFS. Once the plasma reaches the SOL region, a new phenomena can occur: parallel flow can bring the particles along the lines of the magnetic field (in the horizontal direction, in this sketch) and the plasma will flow into the divertor target plates. The flux can also travel across the magnetic surface, through turbulent or "anomalous" transport. Some of the fluxes make it to the wall, but the rest is swept through by the parallel flow and into the divertor target. In a non-diffusive approximation, the cross-field flux can be represented as a turbulent flux,

$$\Gamma_r \simeq \langle \tilde{n}\tilde{v}_r \rangle + \Gamma_r^{\text{neo}}, \tag{2.1}$$

where $\langle \tilde{n}\tilde{v}_r \rangle$ is a time average or a poloidal surface average of the density fluctuation times the radial velocity fluctuation, and maybe a neoclasscal contribution Γ_r^{neo} from trapped particles. Similarly, the heat flux

$$q_{e,i_r} \simeq \frac{3}{2} T_{e,i} \langle \tilde{n}\tilde{v}_r \rangle + \frac{3}{2} n_{e,i} \langle \tilde{T}_{e,i}\tilde{v}_r \rangle + q_{e,i_r}^{\text{neo}}, \tag{2.2}$$

where the first term accounts for the convection piece of the heat flux, where the particles carry a finite amount of energy, the second term represents a conduction piece due to the correlations between the velocity fluctuations and the temperature fluctuations, and the third term can account for the neoclassical component of the heat flux. Usually, the turbulent contributions are much larger than the neoclassical contribution. A diffusive approximation of the cross-field plasma flux can also be used, which will be described later in this work.

2.1 Plasma-material interactions

2.1.1 Material erosion and impurity

The open field lines in the SOL carry immense heat and particle fluxes. There are enormous heat fluxes to the divertor targets, and some heat flux to the first wall, although usually, the radial heat fluxes to the first wall are much lower than the parallel heat flux to the divertor targets. There are also high particle fluxes to the divertor target; the divertor target is impacted by ions from the plasma approximately once every microsecond, and this constant bombardment from plasma ions and the target surface damages and erodes the material of the divertor plate.

Plasma ions impinge on the material surface at a finite energy, typically $\sim$100eV, and implant into the first 1-100 Angstroms of the material surface. They can come to rest in the material, forming trapped gas, or they can be bounced back into the plasma, typically neutralized and recycled back into the volume as neutral atoms. The ions can also "kick out" atoms of the material surface in a process called physical sputtering. Depending on the material, the plasma can also cause chemical sputtering, where the plasma forms molecules with atoms on the material surface that are released by thermal properties into the plasma. The plasma can also be permanently trapped in the material and form bubbles and blisters, diffuse deep into the material and eventually reach the cooling channels located about a centimeter below the surface, or become trapped in defects in the material created by the fusion neutrons themselves, known as radiation defect trapping. All of these processes lead to the retention of fusion fuel, particularly tritium.

2.1.2 Plasma sheath

The plasma sheath is a region directly next to the material target, between the plasma and the material surface. Here, the dynamics of the plasma change as electrons (which have a much higher thermal speed than ions, since they are lighter) rush towards and impact the material surface before the ions, breaking the quasineutrality of the bulk plasma. Under these conditions, a plasma sheath forms in the vicinity of the target. This region is characterized by a strong electrostatic field, which will repel most of the free-streaming electron flux and attract ions to fall towards the target. A cartoon of the electric field configuration near the material surface is shown in Figure 2.3 for a "classical" sheath with no secondary electron emission from the material surface. Depending on the conditions at the material surface, there

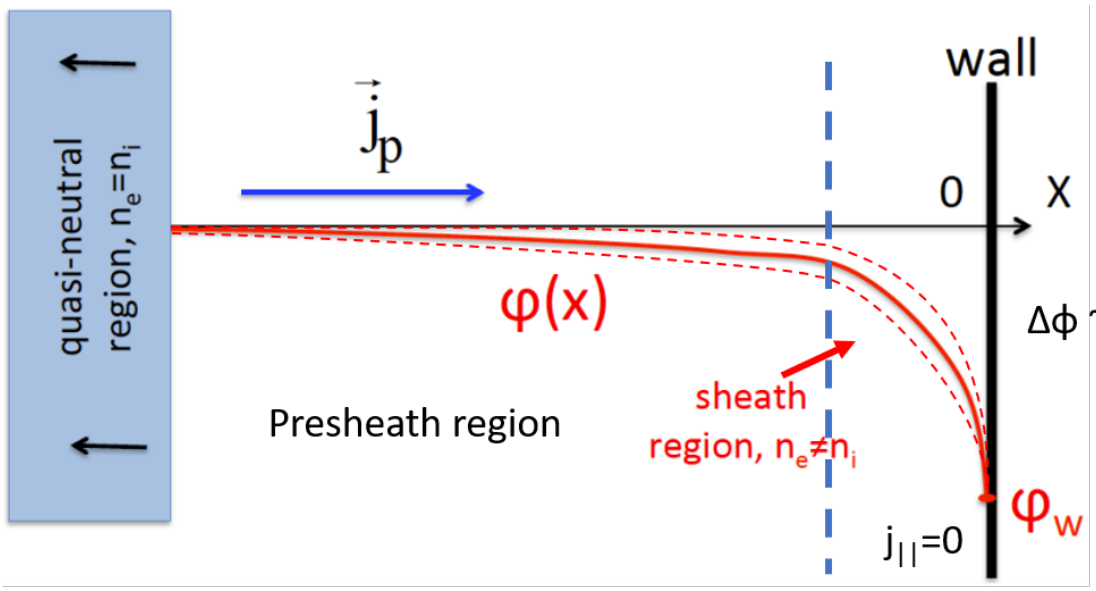

Figure 2.3. Cartoon of the plasma sheath. The potential drop is shown in the red solid line, while the dashed red lines represent the fluctuations in the potential. The quasi-neutral, presheath, and sheath regions are shown. Figure modified from [12].

are several sheath strucures which can form [13]. The classical or "Bohm" sheath forms under typical plasma conditions, where plasma ions are subjected to an increasingly negative potential profile (relative to the bulk plasma) that will accelerate the ions as they approach the material surface [14]. In the presence of secondary electron emission, the potential profile can have narrow positive potential region directly adjacent to the surface if the emission is weak (for a space-charge limited sheath [15]) or the potential profile can be positive and repel ions if the emission is strong (inverse sheath [3]).

The basic model of the sheath assumes that the ions flowing towards the surface are collisionless, and the kinetic energy of the ions will be conserved as they fall down a potential profile. If a material surface is on the righthand side in Figure 2.3, the magnetic field will be going from left to right. Near the plasma edge, there is a potential drop that is very weak in the main plasma and drops off very steeply in a very thin layer close to the target, marked by the blue dashed line in the figure. The thickness of this plasma sheath is $\sim$ 10 Debye lengths, or $\sim$ 10s of microns in a fusion-grade plasma. The so-called "pre-sheath", where the potential drops weakly, can extend a few centimeters or up to a half a meter into the main plasma. The ions will get drawn towards the edge by the weak potential drop in the pre-sheath, and travel along towards the target as the potential drop becomes greater and greater until it hits the sheath

region, where it is accelerated into the target. The potential profile in the sheath region must satisfy the nonlinear differential equation

$$\frac{\mathrm{d}^2\Phi}{\mathrm{d}x^2} = \frac{en_e}{\varepsilon_0}\left[exp\frac{\Phi}{T_e} - \left(1 - \frac{\Phi}{\frac{1}{2}Mu_s^2}\right)^{-1/2}\right]. \tag{2.3}$$

For a stable sheath to exist, the ions must enter the sheath region at the ion acoustic speed, meaning they will become supersonic as they accelerate through the sheath and into the target. They will strike the surface with a certain energy, that is proportional to the electron temperature. Typically, in a fusion-grade hydrogen plasma, this potential drop is approximately 3 times the electron temperature.

2.2 Divertor

It has been well-known since the dawn of the fusion era that the interaction of the plasma and material surfaces is an unavoidable part of tokamak operation: there must be some surface to "guide" the plasma and mitigate heat exhaust [16]. Initial attempts to facilitate this were "limited" tokamaks, where a metal bar or plate would be exposed directly to the plasma. This did not work; issues with impurities and erosion and difficulty achieving the H-mode configuration made the limited tokamak configuration unfeasible for modern experiments.

An improvement to the limited configuration is the diverted configuration, shown in Figure 2.1, which results as a consequence of plasma shaping. In cross-sections with magnetic x-points that give the separatrix two (or more) "legs", the aptly-named "divertor" diverts heat and particle fluxes from the main chamber along these separatrix legs into a separate region of the device, where these fluxes can be handled appropriately via deliberate engineering choices that can take advantage of certain geometric properties, materials, and other physics processes that can improve overall confinement [13]. These coils direct the open field lines away from the closed field lines and core plasma and towards specially-designed targets, reducing the pollution of the core plasma with impurities stemming from plasma-material interactions.

Although a diverted tokamak configuration reduces much of the heat and particle fluxes to the device walls by redirecting it into the divertor region, there are still several engineering concerns for materials

and design of a divertor which must be addressed. In the diverted configuration, heat and particle fluxes exhausted from the core plasma must be directed to some first-wall surface, which must be able to withstand these extreme conditions. These conditions can cause significant erosion of plasma-facing materials, which can cause the release of the eroded material as impurity contamination into the divertor volume. Further, these targets must be able to withstand long exposures to the harsh conditions of the plasma exhaust without needing regular replacement, which can be inconvenient and costly. A divertor also must control particles by providing channels to remove unwanted material from the divertor volume, controlling plasma density and fuelling the plasma, and maintaining neutral pressure in the system [17].

Ultimately, the outstanding question in divertor physics is how to increase the width of the scrape off-layer heat load (denoted as λ_Q). Heat exhausted from the core plasma Q_{SOL} will enter the divertor and travel along the field lines to hit the targets. Localization of these extreme heat loads is very bad for the plasma-facing materials, and it is an active field of research to mitigate these concentrated heat loads through advances in divertor design.

2.2.1 Divertor plasma detachment

Present understanding indicates that the operational regime that is best-suited for handling these extreme conditions by allowing for both heat removal and the suppression of incoming particle and heat fluxes to the material surfaces is the "detached divertor" regime. Virtually all present-day tokamaks and future reactors will operate in this detached divertor regime, where a collection of atomic and radiative processes nearly extinguishes the plasma heat and particle flux before reaching the targets [16].

This scenario is a continuation of the "high-recycling" regime in the dense divertor plasma, where the neutral ionization source in the divertor volume exceeds the hydrogen fueling rate into the tokamak, leading to ionization trapping of neutrals and a fast recycling loop of plasma-neutrals-plasma in the divertor volume [16]. For the simplest case where anomalous cross-field transport is presumed local, the SOL and divertor plasmas can be treated as a self-organized object, where distribution of plasma parameters across the system is dependent on hydrogen (both plasma and neutral) density, impurity content, and input power [18]. This means the upstream plasma is sustained by the loop of plasma recycling processes (namely, neutral ionization in the divertor volume, volumetric recombination of the

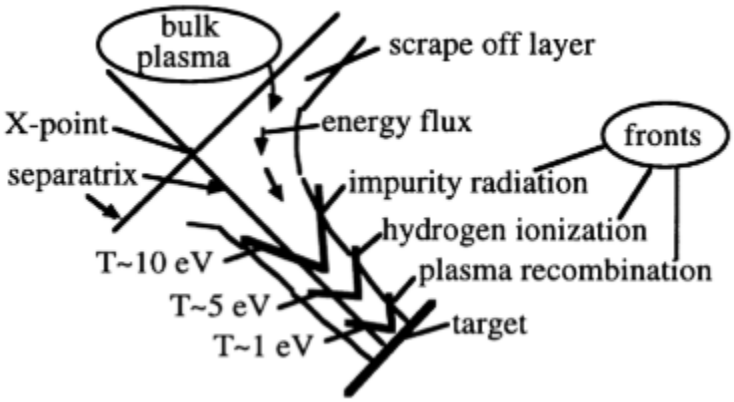

Figure 2.4. Figure from [9]. Schematic view of different regions in a tokamak divertor.

plasma, and plasma neutralization and recycling at material surfaces; the spatial distribution of these "zones", along with their associated temperatures, is shown in Figure 2.4), where ionization is powered by the energy entering the divertor region. Because of this, and the strong dependence of the recycling processes on temperature, these regimes can be highly sensitive to the energy balance in the divertor.

To a certain point, increasing hydrogen particle density increases the plasma flux to the divertor target, but at some value, the plasma flux to the target will saturate and begin to decrease with increasing particle density, "detaching" from the material surface. This is the onset of the so-called "detachment" process, which is characterized by a "rollover" of particle fluxes to material surfaces as an input parameter (such as density or even impurity radiation) is varied, which can be measured experimentally or assessed via physics simulations; experimental measurements of this behavior are shown in Figure 2.5, and simulation results which validate that this phenomenon is a consequence of upstream dissipative processes is shown in Figure 2.6. The important effect of this "rollover" is that it is associated with the neutralization of plasma fluxes and release of potential energy from the neutralization of the ion-neutral pairs in the divertor volume, which would otherwise cause large heat loads to the targets.

At small T_d, this process can be characterized by a simple energy and particle balance [20],

$$\Gamma_W = \frac{Q_{SOL} - Q_{imp}}{E_{ion}} - \Gamma_{rec}, \tag{2.4}$$

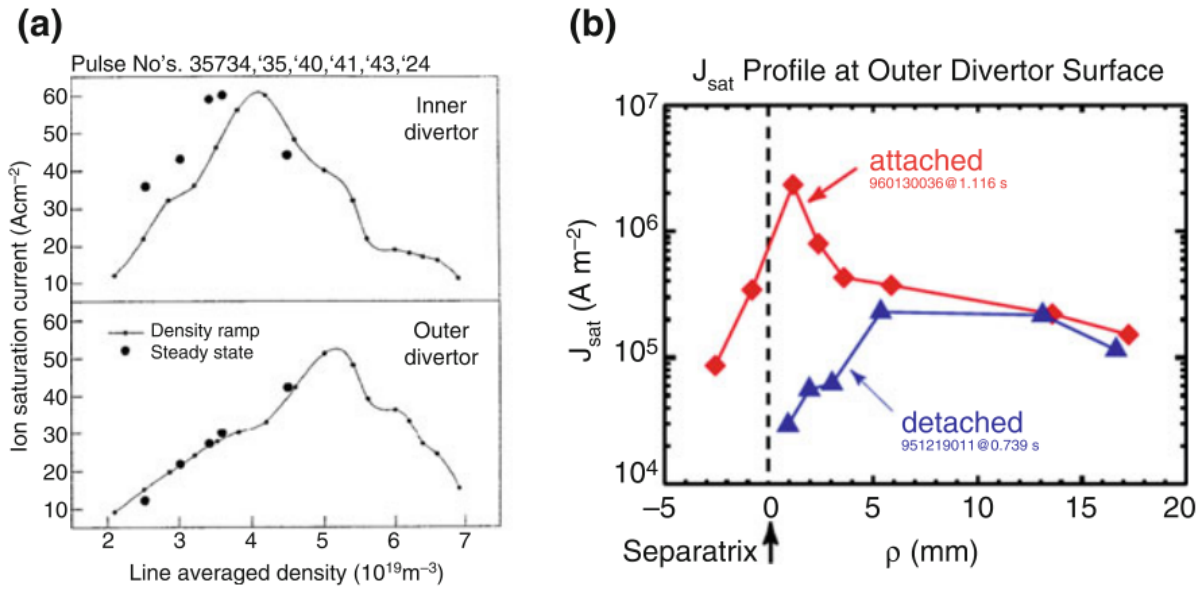

Figure 2.5. Figure from [13]. Specific plasma fluxes on (a) the inner and outer divertor targets in JET versus the line averaged plasma density (Reproduced from [19]) and (b) the outer divertor target in attached and detached regimes in C-Mod tokamak (Reproduced from [17]).

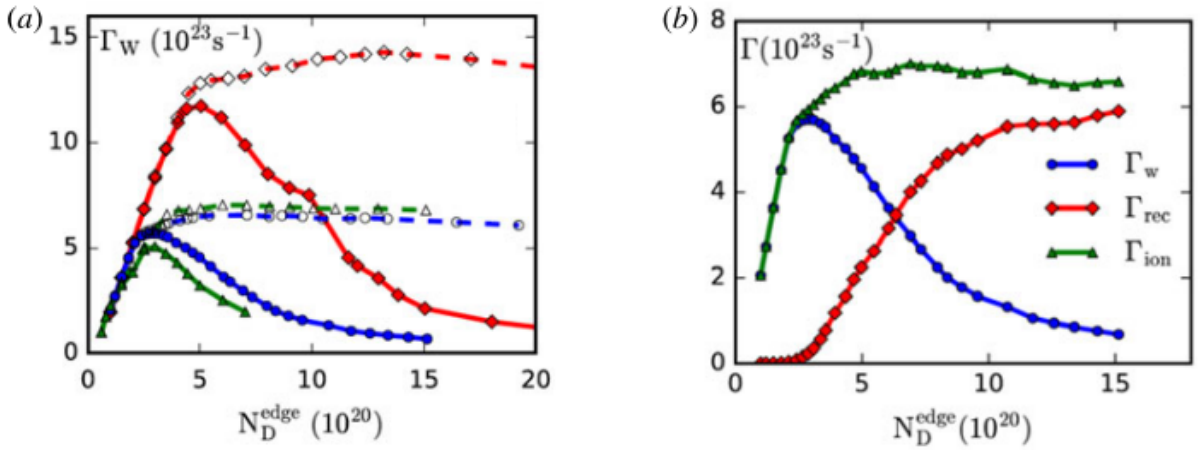

Figure 2.6. Figure from [16]. (a) Dependence of the plasma flux Γ_w on N_D^{edge} for: Q_{SOL} = 8 MW, Q_{imp}=0 (red) Q_{SOL} =4 MW, Q_{imp} =0 (blue) and Q_{SOL} =8 MW, Q_{imp} =4 MW (green) with (solid lines) and without (dashed lines) volumetric plasma recombination; (b) dependence of Γ_{rec}, Γ_{ion} and Γ_w on N_D^{edge} for Q_{SOL} =4 MW and Q_{imp} =0 with volumetric plasma recombination turned on.

where Γ_W is the total plasma flux to the divertor target, Q_{SOL} is the incoming heat flux from the scrape-off layer, Q_{imp} is the impurity radiation loss in the SOL and divertor volumes, E_{ion} is the energy "cost" of hydrogen ionization (approximately 30-40 eV) and Γ_{rec} is the plasma sink from volumetric recombination [13, 16, 21]. This expression describes the key ingredients in accessing the detached divertor regime: the first term characterizes the neutral ionization source from the power available for plasma recycling (the overall input power Q_{SOL}, minus losses to radiation) and the second term simply describes the loss of plasma to the recombination process. This means that, for a given Q_{SOL}, target flux can only be reduced by increasing impurity radiation to reduce the plasma source, or increasing losses to recombination to increase the plasma sink.

2.2.2 Alternative divertor configurations

Many simulations have validated the understanding of the physics of detachment in existing, "standard" flat-plate divertors used in present-day devices and planned for ITER [13, 16]. However, in recent years, several "alternative" magnetic divertor configurations have been suggested to help solve the heat loading issues faced in future reactors. Design choices made in these alternative magnetic configurations is generally guided by the physics principles behind plasma detachment. For example, some of the design elements included in these new designs involve increasing the volume of the divertor, allowing more space for turbulent heat flux spreading and volumetric processes to dissipate incoming power, moving the target further away from the core plasma to protect the core from impurity radiation, or manipulating the field to broaden the magnetic flux tube as it terminates on the divertor plate to delocalize the perpendicular heat flux to the target, among others. Other geometric modifications to the plasma-facing components of the divertor, such as divertor baffling or "closure", can effect plasma conditions in the divertor through neutral-plasma interactions by impacting neutral transport and confinement that can improve access to the dissipative divertor regime [2, 16], though they are not considered alternative magnetic configurations since they do not involve deliberate manipulation the magnetic field.

Many of these factors - and often a combination of several factors - have motivated and contributed to many proposed new magnetic divertor configurations, which have been tested in experiments and assessed in simulations. However, the "big picture" is not so simple; adjusting these design elements could have implications on the divertor plasma conditions and the interplay between these factors could introduce

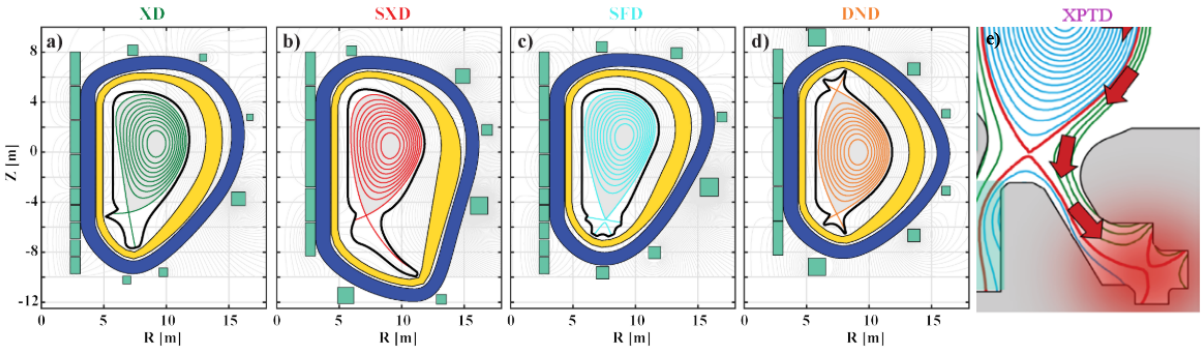

Figure 2.7. Divertor geometries for various proposed alternative divertor configurations, taken from [22] and [23]. (a) shows the X-Divertor configuration (XD), (b) shows the Super-X Divertor configuration (SXD), (c) shows the Snowflake Divertor Configuration (SFD), (d) shows the Double Null Divertor Configuration (DND), and (e) shows the X-Point Target Divertor configuration (XPTD).

other complications. The physics involved in the plasma detachment process will be studied in this work, using a magnetic configuration with a long outer leg and tight baffling along all divertor side walls. Several alternative divertor configurations have been proposed which feature a long outer leg, some of which are described in the following section.

2.2.2.1 X-Divertor

An X-Divertor (XD) is a configuration where a second magnetic X-point is created downstream of the LCFS X-point, beyond the divertor target, shown in Figure 2.7(a) [24]. This will allow for an expansion of the poloidal flux, an increase in the whetted area of the target, and introduce a variation in the field line pitch by decreasing the grazing angle of the field lines at the target. In this configuration, the field lines at the target are "flared" (rather than impacting the target orthogonally, as in the standard configuration), which spreads the incoming heat flux across the entire "flared" section and reduces the peak power loading at the target. This configuration has been tested in experiments - while it was projected that the increased connection length would increase radiated power and enhanced flux expansion would lead to lower target heat fluxes, results were inconsistent. Higher radiation was observed near the X-point in TCV, but increased in the divertor leg and near the target in DIII-D, both showing dangerous localization of radiation losses (albeit in different locations, further emphasizing that the physics mechanisms at play in this process are not wholly understood) [25].

2.2.2.2 Super-X Divertor

The Super-X Divertor (SXD) is similar to the X-Divertor, but with a long divertor leg, and shown in Figure 2.7(b). In this scenario, a second magnetic X-point is placed beyond the divertor target plate, which is located at a much larger strike point radius R_t than the standard configuration [26]. Increasing R_t not only increases connection length and target whetted area, but also enhances the toroidal flux expansion effects at the target in addition to the poloidal flux expansion effects of the second X-point, since the poloidal field $B_\phi \propto 1/R_t$.

2.2.2.3 Snowflake Divertor

The snowflake divertor (SFD) is a configuration where a set of poloidal field coils is used to develop a second order null in the poloidal field in the divertor, which splits the poloidal plane into six (as opposed to four, in the case of the more typical single null X-point divertor) sectors, shown in Figure 2.7(c) [27, 28]. This cartoon does not show a long leg on the snowflake divertor, but long leg snowflake configurations have been demonstrated on TCV [29]. This arrangement, the structure of which is reminiscent of the shape a snowflake, is topologically unstable, but allows for heat load to be spread over a much larger area than a standard divertor by increasing the divertor volume (thus increasing connection length), increasing the total number of active divertors N_{div}, and broadening the power decay width via the enhancement of perpendicular transport induced by the 'churning mode' observed in higher order null configurations [30]. It is possible to access a modified version of this configuration in present-day, conventional-aspect ratio tokamaks and medium-size spherical tokamaks with open divertors as a "SF-minus" or "SF-plus" configuration, where the topologically unstable double null configuration splits into two adjacent single-nulls. Several experimental studies have been conducted on TCV, NSTX, DIII-D, and EAST, which show issues with stability and some difficulty in proper diagnostic assessment, but showed evidence of enhanced transport and power sharing between multiple strike points and a reduction in divertor heat fluxes attributed to an increased connection length and flux expansion [31].

2.2.2.4 Multiple Divertors

Multiple divertor configurations are divertor configurations with multiple "standard" X-point divertors, shown in Figure 2.7(d). This configuration has been realized for many present-day tokamaks and

envisioned for next-generation devices, but is still considered as an "alternative" divertor configuration because incoming SOL power and particle fluxes are split among N_{div} divertors (which can also be positioned at larger strike point radius R_t for a larger whetted area and longer connection length) [25]. Presently, tokamaks are designed with a "double-null" divertor configuration, where up-down symmetric sets of divertor coils can access a standard X-point divertor at both the top and bottom of the device. Future configurations can extend this configuration to include other elements of alternative divertor configurations, outside of the standard X-point divertor configuration.

2.2.2.5 X-Point Target Divertor

The X-Point Target Divertor is a novel divertor concept proposed in the design of the recently conceptualized ADX and ARC tokamak experiments [23, 32]. The XPTD configuration is not accessible in present machines, since accessing this configuration is impossible without very deliberate design choices made in device construction and careful design of control systems, shown in Figure 2.7(e). This configuration uses a second, remote X-point to produce a fully detached, radiating plasma as a virtual target in a secondary chamber located at a large major radius - essentially, intentionally creating an X-point MARFE [33] in a remote chamber within the divertor volume. The goal of this configuration is to take advantage of some of the properties of the other alternative configurations - namely, a longer connection length, large major radius, and tight baffling - to operate with a fully detached divertor, while avoiding any stability-related issues associated often associated with the full detachment of the plasma, since thermal instabilities associated with the motion of the detachment front towards the X-point and issues with PMI would be avoided with the second chamber [34]. Simulations of this configuration indicated promising radiation spread along the divertor leg, but used the "fixed-fraction" impurity model that tends to over-value impurity radiation losses in regions of high electron temperature [8].

Chapter 2, in part, appeared as a part of a series of lecture notes prepared for the PHYS 218C course taught by Professor Patrick H. Diamond at UC San Diego in Spring 2021. The dissertation author was the author of this material.

Chapter 3

Modeling the SOL

> *The object we model is complex, the models we use are not based only on first principles, and the relative importance of the effects can change with the scale of the device. Therefore interpretation of the code results, together with formulation of the model, is the most important part of the modeling process. Eventually, it is the human brain that does the modeling, and the code is a tool, like an axe in hands of a carpenter. Building the experience is therefore essential for the success of modeling, exactly as it is in experiment, and this requires time.*
>
> - [35]

3.1 Transport modeling

A model of the edge plasma in a fusion device must combine plasma fluid theory, atomic and molecular physics, turbulence, materials science, and kinetic theory with numerical techniques capable of calculating conduction and convection with extreme anisotropy [36]. The major difficulty in developing these models is that processes in the edge plasma occur across a wide range of scales, and it is not practical to resolve all processes occurring in the plasma edge solely from first principles. These processes, which range from sub-microsecond collisional processes between neutral gas and plasma, to millisecond-scale turbulence, to several tens of milliseconds for the equilibriation of plasma parameters along the field lines (constrained by the sound-speed and connection length), to the longer-term evolution of the state of material surfaces surrounding the plasma, which can take 100's to 1000's of seconds until saturation is achieved, if ever [13], span more than nine orders of magnitude, and achieving a comprehensive model would be computationally and technically unrealistic. As such, it is necessary to make approximations

and assumptions to simplify the models to approximate the behavior of the plasma, neutrals, and material surfaces at the tokamak edge.

In the highly collisional edge plasma, it is possible to make reasonable predictions for edge plasma behavior, despite these (many) limitations and approximations, by assuming near-Maxwellian distributions for the plasma components to describe them as a fluid and including some "corrections" to emulate anomalous transport. This approach characterizes the large spatiotemporal scale quasi-equilibria and flows of particles and energy in realistic tokamak and divertor geometries, while incorporating additional models for neutrals, atomic and molecular physics, and boundary interactions (including surface effects, the plasma sheath, and puffing and pumping, among others). This is possible because the transport modelling approach is primarily aimed at resolving effects on a time scale that is much longer than the ion gyration time, where the momentum component that is parallel to the magnetic field line is only retained in the momentum equations and perpendicular transport can be simplified with a diffusive approximation across all the equations. These turbulence effects are included through anomalous transport coefficients that emulate the collective effect of small-scale cross-field fluctuations. Various coefficients and other settings can be informed by other, more highly-specialized simulations or real experimental measurements to improve the fidelity of the computational model.

3.2 Braginskii and Braams

The two-dimensional edge plasma model used in most edge codes is based on a formulation (now known as "B2") proposed and implemented by B. J. Braams [37] to model plasma from just inside the separatrix to the outer edge of the scrape-off layer, which uses the two-fluid Navier-Stokes-like characterization of classical multi-species plasma transport theory articulated by S. I. Braginskii and F. J. Hinton [38, 39] for the parallel transport, with additional anomalous components to account for radial transport. This fluid-like model describes the continuity of species, the momentum balance of species, the diffusion of species, and an electron and ion energy balance, where all ions share a common temperature, using equations of a type [40]

$$\frac{\partial U}{\partial t} + \nabla \cdot \overline{\Gamma} = S_0 + S_U, \tag{3.1}$$

where $U \in \{n_i, m_i n_i v_i, \frac{3}{2} n_e T_e, \frac{3}{2} n_i T_i + \sum m_i n_i v_i^2/2\}$ for the particle, momentum, and energy densities, Γ is the flux of the corresponding quantity and S_0 and S_U are effective "source/sink" terms relating to the interactions with neutrals and with charged particles (anything that is not written as a divergence, such as particle sinks/sources or friction forces). The term n_i refers to the ion density (with a separate fluid for each charge state of every plasma species used in the model), m_i is the ion mass, v_i is the fluid velocity along the magnetic field, and $T_{e,i}$ is the electron or ion temperature (where T_i is the same for all ions, a reasonable simplification since temperature relaxation is considerably faster for ions than electrons due to the mass difference). Neutral atoms are either treated as a fluid, following a Navier-Stokes equation and using a common temperature with the ions T_i, or evaluated kinetically, through the S_0 neutral source term with a Monte-Carlo model. Separate electron parallel momentum and continuity equations are not considered because of small electron mass and plasma quasi-neutrality. These equations are solved numerically on a grid of quadrilateral cells that are aligned with the curvilinear geometries of the magnetic flux surfaces and divertor targets that represents a presumed axisymmetric radial cross-section of the tokamak in the poloidal plane.

Atomic and molecular processes characterized by S_0 and S_U are considered through temperature and density-dependent reaction rates determined for each process in each computational cell. These rates are retrieved from databases (such as ADAS [41], AMJUEL [42], and HYDHEL [43]) that store a multitude of rate information calculated from collisional radiative model (CRM) calculations of many species over many conditions, and fed back into the continuity equations to calculate sink/source terms. These rates provide information on radiation, ionization, recombination, charge exchange, elastic scattering, and dissociation, which are then fed back into code to determine the sink and source terms in the continuity equations in all species.

Boundary conditions are applied at the divertor targets, radial boundaries, and the core, and can be chosen to replicate specific experiments or other physical considerations. In general, sheath boundary conditions are applied at the divertor targets, decay lengths for all quantities are prescribed at the radial boundaries, and fixed power and particle fluxes are specified at the core boundary to emulate the incoming plasma exhaust, although other different and specialized boundary conditions for the three domains can be used. At all edges of the computational domain, which characterize the targets and radial boundaries,

particle reflection can be characterized through a neutral albedo and recycling coefficient, or optionally, for kinetic treatments of neutral particles, determined with a reflection probability and energy that is calculated using TRIM data [44] (similar to the atomic databases), where all particles not reflected are desorbed as molecules or atomic impurity with the wall temperature [40].

3.2.1 Length scales and the fluid approximation

The fluid approximation of the parallel transport in the edge plasma requires a specific ordering of length scales to be resolved by the code [45]. To apply a fluid model to the edge plasma, all characteristic lengths must be smaller than the plasma gradient length or the parallel connection length, which is normally on the order of several tens of meters. This includes the characteristic length of the sheath (a microscopic scale length of about ten Debye lengths), electron and ion mean free paths (ranging from sub-centimeters to meters), neutral mean free path (centimeters to meters), heat conduction length (typically five times the mean free path length, since the dominant contribution is from the tail electrons or ions). The terms in the Braginskii-like equations are only valid when the Coulomb mean-free path of the particles is much smaller than the scale length variation of the plasma parameters along the field line. In general, the edge plasma follows this ordering, with several notable exceptions that are treated by the code.

At low temperatures, such as near the divertor targets, steeper gradients can result in non-local heat flux contributions that require a non-local description of the heat flux to maintain continuity. At high temperatures, such as near the midplane at the separatrix, the majority of heat is transported by supra-thermal particles, where the heat conduction mean free path is longer than the connection length and the parallel energy transport is non-local. Both of these exceptions are resolved with flux limiters on the parallel heat flux and momentum flux (as viscosity), which are factors applied to the fluxes that limit the flux to a fraction of the free streaming flux, scaled appropriately to match supplementary kinetic simulations. Similar throttles on the parallel fluxes are applied as long mean free path corrections for the classical heat conduction and viscosity in the core, scaled linearly by estimates of periodicity wavenumber and the mean free path of tail electrons that matches scaling observed in simulations of electron heat transport in laser plasmas [45].

In regions where these kinetic corrections become important, the quantitaive conclusions of the fluid codes are somewhat questionable, since the fluid model is no longer strictly valid. However, the considerations of particle, energy, and momentum conservation are still upheld, ensuring that the description of the edge plasma is, at least, qualitatively correct. While these flux limiters are not perfect, particularly in cases of purely predictive modeling where comparisons to experiments are not possible, they provide a reasonable basis for understanding the physics mechanisms in the edge plasma.

3.2.2 Diffusive ansatz for radial transport

Tokamak edge radial transport is anomalous, but self-consistent turbulence is difficult to model, and beyond the scope of the 2D edge plasma formulation characterized in available modeling software. As such, in edge transport codes, the radial component of the transport is determined using a "diffusive ansatz", or the assumption that cross-field particle and energy fluxes are purely diffusive and can be described by a Fick's law:

$$\Gamma_r \sim -D\frac{\mathrm{d}n}{\mathrm{d}r},\ q_r \sim -\chi\frac{\mathrm{d}T}{\mathrm{d}r}, \tag{3.2}$$

which is also sometimes supplemented by a convective flux nu_r to describe inward transport (like impurities or blobs). Physically, this characterization effectively results in a time-averaged approximation of the cumulative effect of various cross-field transport processes.

This assumption is computationally useful because it eliminates the need for numerically intensive turbulence simulations, but makes it difficult to fully reconcile the numerical results calculated using assumptions made in the diffusive ansatz with the known physics of the edge plasma. In the diffusive ansatz, transport is described locally, meaning the fluxes at each point in the numerical grid are dependent only upon the plasma parameters at that spatiotemporal point. This can make the calculation and interpretation of discharges which assume a time-dependent model difficult or impossible to do correctly, since in reality, the character of the turbulence evolves in space and time, and these effects are not captured in the code.

3.3 Treatment of neutral transport

Neutrals play an essential role in the multitude of physics processes occurring in the edge plasma [46]. Because neutrals are not charged, they cannot be affected by the magnetic field, so their transport is different relative to the other charged components of the plasma. However, the distribution of neutrals is dependent on the plasma (and vice versa), so it is necessary to solve the plasma and neutral transport equations together. The simplest way to do this is to use fluid models for neutrals, which treat the neutral particles as a continuous fluid with equations of state and transport to describe their behavior. Usually, these models are easier to implement and computationally efficient, since they share a similar formulation and implementation to the equations describing the plasma, but have limited realistic applicability. Since the fluid formulation assumes short mean-free path of neutrals with respect to neutral-ion or neutral-neutral collisions which can be longer than the scale length of the profiles for the plasma parameters, this approximation is rather dubious outside of regions of high plasma density. Further, the fluid equations are solved on each cell of the computational mesh, which are aligned with the magnetic field; in reality, neutral transport has no preferential direction since the neutral particles are not charged and should be treated with 3-D kinetic calculations, which can be computationally demanding. Significant effort has been devoted to the assessment and optimization of these models [47, 48].

3.3.1 Fluid neutrals

The basis for the validity of the fluid neutral model is that the relaxation of the distribution function of the plasma species atoms evolves towards the plasma ion distribution function through charge-exchange collisions with plasma ions [49], since neutral-neutral collisions are often too rare to establish a Maxwellian distribution of the neutral particles. While the underlying assumptions for the basis of the fluid approximation result in a model that is more more rudimentary than high-fidelity Monte-Carlo approach, some fluid neutral models include considerable complexity and can account for processes like wall reflection and volumetric recombination, and couple to the plasma equations as sources of particles, momentum, and energy. Ultimately, these more complex models show reasonable agreement with the Monte-Carlo approach under some circumstances, particularly when comparing models that only characterize hydrogenic particles [50]. The fluid model struggles to correctly model other cases, where the transport and influence of molecules is likely to be significant, or in the near-separatrix region where the mean-free path

of the neutral particles is larger than the scale length variation in the plasma parameters and the closure assumptions for the fluid equations are violated, or with correctly modeling complex collisional processes in the plasma and with the walls, particularly with the geometric details of the vessel configuration.

3.3.2 Monte Carlo neutrals

The "kinetic" approach most commonly used to describe neutral transport in the edge plasma uses stochastic Monte-Carlo models instead of solving kinetic equations. This direct Monte-Carlo model calculates the trajectories of test particles based on pseudo-random numbers with initial conditions from a fixed plasma background, where the source terms from Eq. (3.1) are calculated by determining their intensity along the particle trajectory and summed over all the trajectories in a cell. This method can include a multitude of species and reactions for the particle trajectories and flexibility with the prescribed collision and interactions between the particle and the background plasma. The geometry of the neutral Monte-Carlo domain can be arbitrarily complex, extending beyond the rather rigid magnetic domain that restricts the plasma calculations to the entirety of the material surfaces and vessel walls. This expanded computational domain allows for neutral transport calculations that include neutral-neutral interactions, radiation transport, and complex channels and surface features in the intermediate area between the plasma and the vessel.

Although its flexibility and customizability make the Monte-Carlo approach appealing for a neutral model in the plasma edge, there are several considerations that can make this approach impractical. By the nature of the randomness of the Monte-Carlo model and the finite number of particles traced, there is always noise present in the solution; increasing the number of text particles will reduce this noise, but increase computation time and create noisy distortion in the calculation of the sources in Eq. (3.1), which introduces a different of numerical problems. Another issue with the Monte-Carlo approach is the treatment of the time-dependence of the solution. For each Monte-Carlo calculation, the standard approach is to assume steady state, since the evolution of the plasma parameters is usually much slower than the relaxation of the neutral distribution. However, in situations where this is not the case, and the evolution of plasma parameters is fast, there can be inconsistencies with coupling the plasma and neutral models, which requires more detailed calculations that incorporate time-dependence in the particle tracing at the expense of increased computational time, which is ultimately the biggest drawback in the

Monte-Carlo approach. A single simulation can take weeks or months, depending on the geometry or reaction details that need to be solved. Parallel computing can speed up computational times, but requires significant computational resources and can complicate the treatment of noise in the simulation. Despite these challenges, however, the Monte-Carlo neutral model often shows good agreement with experimental data, and is the default choice for high-fidelity edge plasma simulations.

3.4 Radiation

3.4.1 Fixed fraction

The most basic model that is most often used in UEDGE is called fixed fraction, where the impurity radiation calculation is dependent on a user-specified percent of an impurity species in the plasma. This approach is computationally convenient, but is limited to one impurity species. The impurity density is modeled by taking the user-specified impurity percentage as a percentage of the electron density, and the impurity charge-exchange rate is determined from look-up table data generated by the MIST code. Impurity emissivity is dependent on using electron temperature, charge-exchange recombination, and neutral hydrogen and impurity lifetime due to convection, and the MIST code uses the neutral hydrogen density (from UEDGE) and a user-specified impurity lifetime to calculate a charge-exchange rate from a non-equilibrium coronal model. The impurity "radiates" as a component of the electron energy equation through this artificial impurity calculation, which accounts for molecular processes like excitation, ionization, and recombination. For very general purposes, this approximation can be "good enough", although it is not very accurate at high temperatures when the relationship between impurity percent and electron density is not as strong (since radiation is less efficient at high temperatures, fixed fraction can give an overapproximation of the actual radiation content).

3.4.2 Multispecies models

A higher-fidelity and more computationally strenuous model can also be used that models individual charge states of impurities and calculates continuity, force, and momentum balances for each species (so each charge state of an impurity now gets its own set of equations). This uses diffusion coefficients and other parameters common with the plasma calculations. It also uses lookup tables for impurity ionization, excitation, radiation, recombination, calculated similarly to the fixed fraction model, and which requires

a set of tables for each impurity species. The model can be simplified by using a single mass-averaged momentum for all species, or by using friction forces determined from analytical expressions and ignoring impurity inertia and viscosities to determine individual impurity parallel velocities.

3.5 Implementations of B2

Several edge plasma transport codes based on the B2 (and later, B2.5) formulation of the edge plasma, including UEDGE [51], SOLPS [45], and EDGE2D [52]; in particular, the SOLPS (Scrape Off Layer Plasma Simulator) code, which relies on the B2-Eirene code package, has risen to prominence and widespread familiarity outside the edge modeling community in recent years due to its selection as the tool of choice for predictive edge modeling in the ITER device [35].

The simulations shown in this work were generated using the UEDGE code and the SOLPS code package. SOLPS and UEDGE share many similarities: both are 2D, multifluid tokamak edge codes, both are used to guide experiments and develop theoretical models, both use similar grids, both are based on the B2 code package, using similar fundamental equations derived from the Braginskii equations. However, there are several differences between the two approaches. SOLPS uses a high-fidelity Monte Carlo, "kinetic" model for neutrals, while UEDGE uses a lower-fidelity fluid model for neutral transport. Despite these differences, UEDGE and SOLPS often show agreement in simulation results [45, 53].

The choice of UEDGE over SOLPS for the first part (the inverse sheath study) of this work is multifaceted; while no edge code is "perfect", there are several reasons why the choice of UEDGE for this study made sense. SOLPS uses a high-fidelity kinetic model for neutrals, but the Monte Carlo technique used by SOLPS also introduces numerical noise, calculates slowly, and requires significant computational resources (which can take months to complete). Since this work depends on analysis of the evolution of plasma states over a parameter scan, the Monte Carlo approach used by SOLPS was impractical for an introductory project. The fluid-neutral model used by UEDGE is significantly faster and more lightweight (UEDGE simulations can be run on a local machine, which proved invaluable to the progress of this work when access to university resources was forbidden), and makes it much more conducive to generating parameter scans. Lastly, from a very practical perspective, members and close collaborators of this research group already use and develop the UEDGE code, and this local expertise

significantly accelerated the "learning curve" of operating the code. UEDGE is also open-source and allowed for both transparent understanding of underlying equations and easy modification to otherwise obscured parameters and equations, since modification to the source code was necessary for implementing the specific conditions needed for our study.

However, the second two parts of this project (the investigation into the physics of perpendicular transport and impurity radiation spread in alternative divertor configurations) necessitated the switch to SOLPS for a higher fidelity model. UEDGE is a useful tool for studying existing tokamak regimes, where the choice of coefficients for the anomalous transport calculations and approximations of various parameters relating to things like viscosity and friction can be benchmarked against experimental data, but struggles with proposed or idealized regimes that cannot be guided by experimental results. Initial computational studies of the long leg divertor geometry using the UEDGE code revealed many numerical problems relating to the neutral model that were not observed in the modeling of the DIII-D-like plasma with an inverse sheath (which were apparently widespread among UEDGE users with similar geometries [54]).

3.5.1 The UEDGE code

Simulations for the first part of this work were carried out using the UEDGE ("Unified Edge") code, a two-dimensional multi-fluid transport code for collisional edge plasmas, which can be used to simulate the physics of the edge and divertor regions of a tokamak device [51]. Fundamental equations of the UEDGE code are detailed in Appendix A.

The UEDGE code uses realistic magnetic equilibrium data and device geometries from poloidal flux surfaces calculated using solutions of the Grad-Shafranov equation [55, 56] from an MHD equilibrium code (such as EFIT [57]). Using this input, UEDGE can generate a curvilinear mesh that is used to solve transport equations with boundary conditions specified by the user. Such boundary conditions and other parameters (such as transport coefficients) can be set with the intent to match experimental profiles or to observe the impact of certain parameters to study specific physics phenomena.

3.5.1.1 Numerical solver

The UEDGE code features a fully-implicit non-linear solver that employs a modified Newton iteration, which solves all equations simultaneously [58, 59]. This method combines the algorithm of Newton's method, which solves the roots of real-valued functions, with Krylov subspace methods, which are iterative methods for solving linear matrix-vector equations and avoiding computationally-heavy matrix-matrix calculations [60]. Combining these two techniques results in increased computational efficiency, as the application of Krylov subspace techniques eliminates the need for the calculation and use of the Jacobian matrix used in Newton's method. This works by minimizing the residual in the Krylov subspace (using only matrix-vector calculations) using Generalized Minimal Residual (GMRES) methods; the linear residual is then calculated using Newton's method and avoids direct calculation of the Jacobian by taking a first-order Taylor series expansion of the Jacobian matrix used in Newton's method in terms of the nonlinear set of residuals of vector-valued functions that resulted from the calculation in the Krylov subspace. This gives a vector that approximates the product of a matrix and a vector, which are then used in the GMRES calculations in the Krylov subspace for the next iteration [60]. The process repeats until convergenge to a user-specified tolerance. Computation can be streamlined by preconditioning the solver matrices, usually with one initial preconditioner determined via a direct banded solver.

3.5.2 SOLPS4.3

The SOLPS code package contains the 2-D multi-fluid plasma edge code B2, like UEDGE, but replaces the fluid neutral transport model with a kinetic treatment of neutral particles by coupling to EIRENE, a 3-D, multi-species kinetic Monte-Carlo neutral code. Equations solved by the B2 code and the reactions calculated in EIRENE are listed in Appendix B. These codes are coupled as B2-Eirene [61, 62], using computational meshes created by the Carre grid generator [63], a graphical display program for setting up new configurations DivGeo ("DG") [64], a plotting program for viewing the plasma state ("b2plot"), and a set of scripts and tools for viewing the time-dependent development of the plasma state. Grids for the SOLPS simulations are created using DivGeo, where a plasma equilibrium can be created from scratch or imported from an MHD solver. This interface is also used to make Eirene grids for the neutral calculations, and realistic vessel geometry can be imported into the grid generator to create these meshes. The b2plot program accesses the raw data from the simulations and formats it somewhat neatly

for post-processing, and can be used to produce 1D and 2D plots, although all plots shown in this work were generated with an original set of post-processing tools that was developed specifically for this work.

3.5.2.1 Numerical Solver

The main complexity in the numerical scheme evaluated by the SOLPS code is the coupling procedure between the implicit B2 fluid code and the explicit Monte-Carlo Eirene code. Like UEDGE, the B2 code is implicit and advances discrete analogs of Eq. (3.1) in time, which poses no problems for a fluid neutral model, since these components are fully compatible. However, when coupled to the explicit Eirene code, the particle trajectories and associated source/sink terms determined in the Monte-Carlo step are calculated using an initial background plasma, but fed into a new plasma state. In other words, the neutral related sources that appear in Eq. (3.1) are always determined from the plasma state at the previous step, when the Monte-Carlo algorithm is initially applied to the simulation, and the plasma state that is consistent with the source/sink terms in the calculation is only available after the calculation for that timestep. This causes a mismatch between the plasma state and the source terms, which introduces an artificial parasitic source/sink term into Eq. (3.1). In the overall energy balance, these parasitic source terms are dwarfed by the magnitude of the input power, volumetric processes, and power to the target plates, and make little impact. Similarly, there is little impact on the momentum balance [13]. However, in the particle balance, these parasitic sources can become significant, particularly in the cases of high recycling or detached divertor regimes, when the effective particle fluxes resulting from recycling fluxes and volumetric terms exceeds any input from the core or a puff by several orders of magnitude. Under these circumstances, the parasitic flux can have a serious impact on the global particle balance, which can complicate or obscure a realistic portrayal of the physics in the model. To compensate for this, correction schemes are be applied, where a factor (usually close to 1, if applied at each timestep) based on a non-linear calculation for the global particle balance at each step are included in the other source terms provide a small percent correction for these particle discrepancies [35]. However, this introduces problems in the "closed box" simulation setup, where the total number of particles in the simulation domain is held constant [65], since there is no "source" to scale that could make up for these particle losses. In this situation, a feedback system (implemented to the SOLPS4.3 code) is used, where a "puffing surface" is defined all along the outboard side of the simulation domain. This puffing surface emits a small flux of neutral particles to

compensate for losses to the parasitic source term, automatically adjusting to maintain a desired particle content that is set by the user. Similarly, an analogous setting at the core adjusts a small flux of plasma particles from the core to help maintain the desired particle content.

Chapter 4

Simulations of divertor plasmas with inverse sheaths

Abstract

The effect of strong electron emission from material surfaces has been proposed to form an “inverse sheath”: a region with positive potential relative to the near-wall plasma which prevents the flow of ions to the wall [3–5]. We assess the viability of this regime in a tokamak device using the 2D edge plasma transport code UEDGE [51]. Since the UEDGE code does not consider the sheath region directly, we apply boundary conditions at the divertor targets which emulate the physics of both "standard" and "inverse" sheath regimes [66]. Using these boundary conditions, we perform scoping studies to assess plasma parameters near the target by varying the density at the core-edge interface. We observe a smooth transition in the resultant profiles of plasma parameters for the standard sheath, and a bifurcation across the simulation set for plasmas with an inverse sheath. The cause of this bifurcation is assessed by performing the parameter scan both with and without impurity radiation; we observe that the bifurcation persists in both cases, indicating that this bifurcation is caused by plasma recombination.

4.1 Introduction

It has been proposed that an "inverse" sheath can form at the plasma-material interface when electron emission from a material surface strongly exceeds the incoming ion flux from the plasma. Under these conditions, zero current at the interface would be maintained through the balance between the flux of emitted electrons and flux of ions and electrons from the bulk plasma [15]:

$$\Gamma_e - \Gamma_{emit} = \Gamma_{ion}, \tag{4.1}$$

where Γ_e is the electron flux from the bulk plasma, Γ_{emit} is the net emitted electron flux, and Γ_{ion} is the ion flux from the bulk plasma.

For large Γ_{emit}, is usually assumed that the low energy emitted electrons create a negative space charge layer near the material surface leading to non-monotonic sheath potential, reflecting most of the emitted electrons back to the surface [15]. However, if this electron emission is strong enough that it matches the influx of electrons from the bulk plasma, zero current could be maintained if there is no incident ion flux from the plasma, which would allow the negative charge layer introduced by the emitted electrons to penetrate into the plasma. In this scenario, this previously-proposed space charge limited sheath does not develop: instead, the so-called inverse sheath forms, where the electron emission current from the material surface effectively replaces the ion current to the target, resulting in a monotonic, positive potential relative to the plasma edge which prevents the flow of ions to the wall [3–5].

It is feasible that next-generation fusion devices could be affected by electron emission, as tokamak divertor targets will be exposed to extreme heat fluxes that could cause significant thermionic electron emission [67] and trigger the formation of an inverse sheath. If an inverse sheath were to form in such a device, it could have a dramatic influence on the performance of a divertor, as mitigation of ion flux to the target could have an effect on material erosion due to the reduction of ion impacts [5], but at the expense of losing a significant source of neutrals from recycling at the target; having a sufficient inventory of neutrals is critical because neutral-induced radiation is an important source of dissipative heat loss in the divertor [16].

To investigate whether this has an effect on divertor plasma performance, simulations of divertor plasmas with inverse sheaths have been performed using the UEDGE code [51, 66]. The standard and inverse sheath regimes were compared by using different boundary conditions at the divertor targets, corresponding to the physics of each sheath. The boundary conditions for the standard sheath were not changed from the default conditions already implemented in the UEDGE code (described in Refs. [66,

68], or Section 4.2 of this paper), while boundary conditions for ion flux and ion heat flux to the wall were set to zero to emulate the mitigation of ion flow to the wall in the inverse sheath. These simulations feature 4 MW input power (split evenly between ions and electrons) through the core-edge interface and a 3% fixed fraction nitrogen impurity, with a DIII-D-like geometry and magnetic configuration at a given core-edge plasma density. Perpendicular transport coefficients were set at a constant 1 m^2/s.

This work is divided into two parts: a case study of two simulations (one with a standard plasma sheath and the other with an inverse sheath) to compare the effects of the plasma sheath on global plasma parameters, and a parameter scan of both standard and inverse regimes to assess the differences in plasma dynamics as density is increased. In the first study, it was observed that relative to the standard sheath, the effects of the inverse sheath are localized to the target plates, without significant impact on overall plasma parameters. In these simulations, both the standard and inverse sheath results showed a cool inner divertor and hot outer divertor; compared to the standard sheath, the inverse sheath had marginally lower electron heat flux to the target at the cool inner divertor, while electron heat flux at the target plate in the hot outer divertor was significantly higher. However, while these results showed a direct effect on plasma parameters at the target plates, the conclusions were limited in that they only featured the results of a single set of input parameters for both the standard and inverse sheath regimes.

In the second portion of the study, we expand upon the work performed in the first part and shown in Ref. [66], conducting a scoping study of plasma parameters in the divertor by varying the density at the core-edge interface (which will be denoted as n_{ce}). Apart from varying n_{ce}, all other input parameters (including impurity fraction) were initially kept the same. The parameter n_{ce} was selected because plasma density in both the divertor and the scrape off layer will change as n_{ce} is varied, which allows for a scan of power dissipation conditions dependent on plasma density.

It is possible that changes in plasma density associated with varying n_{ce} will result in the observation of bifurcation-like transitions in plasma parameters. We note that bifurcations have been observed in plasmas with standard sheaths in both simulations and experiments [69–71]. Such bifurcations are thought to be driven by plasma recombination processes, impurity radiation, drifts, or some interplay between varying transport coefficients; the simulations presented here feature no drifts and use constant transport

coefficients, leaving plasma recombination or impurity radiation as potential candidates which could cause a bifurcation in these simulations.

To assess whether similar bifurcations are observed in plasmas with inverse sheaths, two sets of simulations with standard sheaths (one with impurity radiation and the other without impurity radiation) and two sets of simulations with inverse sheaths (one with impurity radiation and the other without impurity radiation) are presented. We observe that bifurcations in plasma parameters appear in plasmas with inverse sheaths; we consider "bifurcation" to be present when two qualitatively different steady-state numerical solutions exist for similar (or even the same) sets of input parameters. These bifurcations persist both with and without impurity radiation, indicating that these bifurcations are related to the plasma recombination process. Section 4.2 will detail our simulation approach and construction. We present our results in Section 4.4.1, with detailed discussion in Section 4.4.2. In Section 4.6, we will make our concluding remarks.

4.2 Simulation Setup

Numerical simulations of divertor plasmas with inverse sheaths were performed using UEDGE [51]. UEDGE is a 2D multifluid plasma edge code, which solves transport equations for ions and neutrals, including continuity, momentum, and energy balance equations, in a realistic magnetic configuration of a tokamak. Collisional processes, such as elastic scattering, impact ionization, and charge exchange, recombination, and recycling are also included in the model equations. A combined energy equation for ions and neutrals is considered in UEDGE. Processes involving molecules and drifts/electric fields can be included in UEDGE simulations, but have been omitted here due to considerable computational cost.

As detailed in Ref. [66], these simulations were performed using a single-null DIII-D-like magnetic geometry and configuration, with an input power through the core-edge interface of 4 MW split evenly between electrons and ions. All simulations used perpendicular transport coefficients were set at a constant 1 m^2/s; since the goal of this study was to assess the effects of the inverse sheath on divertor plasmas and not to match experimental profiles, constant transport coefficients (with no radial or poloidal dependence) that are typical for tokamaks of this size were used. Simulations with impurity radiation used the fixed fraction impurity model with a 3% nitrogen impurity.

Neutral flux balance at the targets is described using a fixed albedo [72] of 99%, which is a fraction of the neutral flux returning to the plasma that represents wall pumping. Ion flux to the side walls is fully reflected as neutral gas.

The parameter scan was performed by varying the density at the core-edge interface, n_{ce}. To generate the scan across n_{ce}, we start with a steady-state solution, slightly increase or decrease n_{ce}, and converge to a new solution at steady state. Boundary conditions were enforced at the target plates, with unique conditions corresponding to the physics of each sheath (standard or inverse).

The UEDGE code uses Bohm sheath boundary conditions, which we denote as the "standard" case. This corresponds to the ion parallel velocity at the inner and outer divertor targets set to the sound speed [73],

$$j_i = n_i C_s. \tag{4.2}$$

At the target, the energy flux is

$$q_{e,i} = j_i \gamma_{e,i} T_{e,i}, \tag{4.3}$$

where e and i denote electron and ion, respectively, γ is the sheath heat transmission coefficient, and j is the particle flux. The ion flux j_i is used for the flux of both ions and electrons to assure local ambipolarity. Sheath heat transmission coefficients were used as $\gamma_i = 2.5$ and $\gamma_e = 4.0$, which are the standard values in the UEDGE code.

To model the inverse sheath, we use a modified version of the UEDGE code that incorporates new boundary conditions at the target plates which emulate the physics of the inverse sheath, including the mitigation of ion fluxes to the targets and electron emission from the targets [66]. These boundary conditions mimic a fully-developed, sustained inverse sheath, and do not incorporate any complications that might force transitions between regimes or "collapse" of the inverse regime altogether.

In the "inverse" regime, we modify the boundary condition by eliminating ion particle flux and ion heat flux to the targets, setting

$$j_i = 0,\ q_i = 0 \tag{4.4}$$

at the target plates.

For electron heat flux in the inverse regime, we use a convective heat flux boundary condition at the wall which incorporates electron emission [66]. Since ion flux is zero, ambipolarity is guaranteed at the target through equal and opposite fluxes of emitted and bulk plasma electrons, assuming an unlimited source of emitted electrons from the plate. Then, the electron heat flux to the divertor plates can be written as

$$q_e = n_e v_{th,e} \gamma_e (T_e - T_{e,w}), \tag{4.5}$$

where $v_{th,e}$ is the electron thermal velocity in the bulk plasma and $T_{e,w}$ is the temperature of the emitted electrons from the wall, set at 0.03 eV. The energy of emitted electrons from tungsten can be as high as 0.1-0.3 eV [5], but we have chosen to use a lower limit of electron energy equal to the wall temperature to exaggerate the effect of the sub-eV electrons and ensure conditions of the inverse sheath are met.

4.3 Single case comparison

4.3.1 Results

Simulations were carried out in both the standard and inverse sheath domains to assess divertor performance and overall plasma parameters. Since we are looking at the influence of the inverse sheath on detachment, it is important to note the features we are looking for in characterizing what "detachment" actually means in these simulations. Detachment is typically characterized by both a drop in particle and

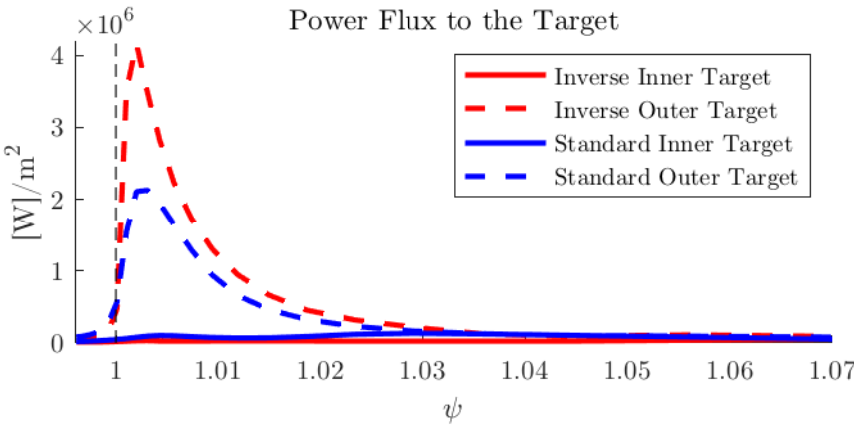

Figure 4.1. Heat flux along the inner and outer target plates for both inverse and standard regimes. Red corresponds to the inverse case, and blue corresponds to the standard case, with solid lines for the inner targets and dashed lines for the outer targets.

heat fluxes to the target [16]. This is true for the standard case, where ions are free to impact the wall, meaning incoming particle flux (or lack thereof) can be used as a metric to indicate plasma detachment. However, in the inverse case, since there is no incoming ion flux to the wall, it cannot be used as an indicator of detachment, so we are relying solely on the heat flux to the target to assess whether the plasma has detached.

The profiles of the simulations for the inverse and standard cases are similar. There is strong asymmetry in both profiles with respect to the inner and outer divertors; shown in Figure 4.1, the inverse and standard cases show signs of a weak detachment (strongest close to the separatrix, then becoming weaker along the target) in the inner divertor, while in both cases the outer divertor is fully attached. This asymmetry is unsurprising because most heat flux travels through the outboard side of the torus due to the effects of the ballooning nature of perpendicular transport, so there is less heat load (and an overall easier transition to detachment) at the inner divertor. Peak heat flux is lower and shifted slightly outward, away from the separatrix, in the standard case because heat transfer is limited by the ion flux; since heat flow in the inverse regime is not limited by the flow of ions, heat flux is larger so the distribution of the heat load will spike adjacent to the separatrix.

Plasma parameters in the divertor region are shown in Figure 4.2. Ion density at the inner target is increased across the plate, shown in Figure 4.2(a), when compared to the standard case, Figure 4.2(d).

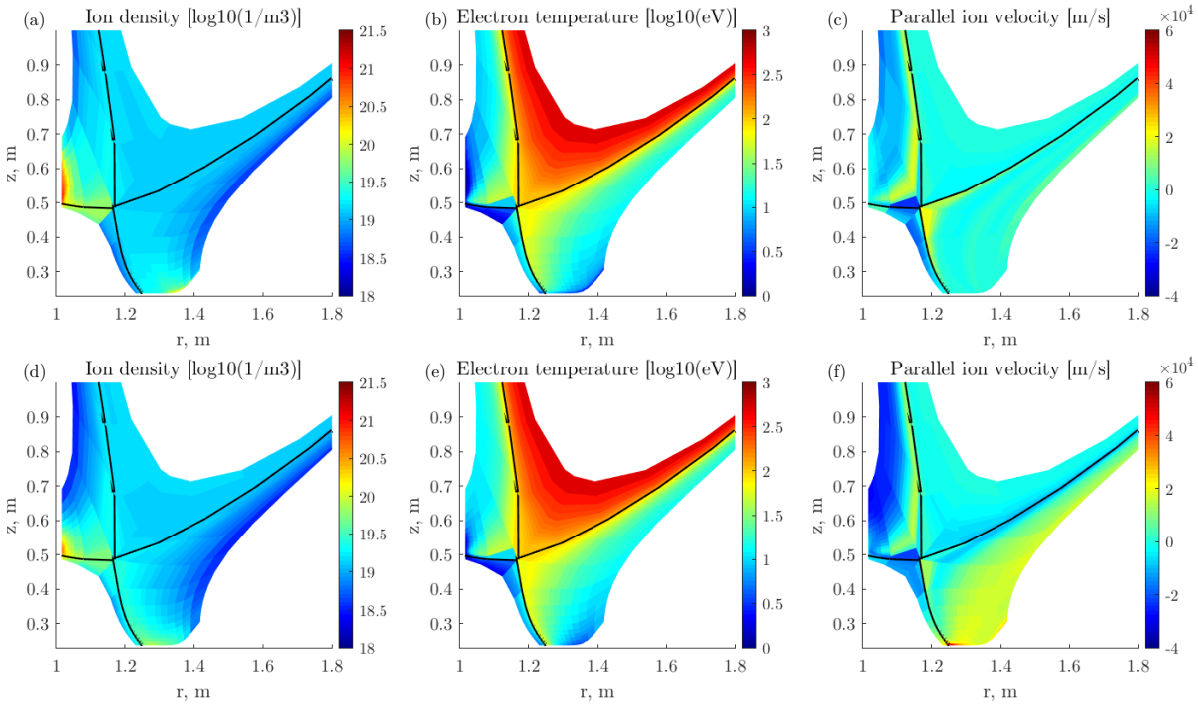

Figure 4.2. Plasma parameters in the divertor region. Figures 4.2(a), 4.2(b), and 4.2(c) show the ion density, electron temperature, and ion velocity rates for the inverse case. Figures 4.2(d), 4.2(e), and 4.2(f) show the same parameters for the standard case.

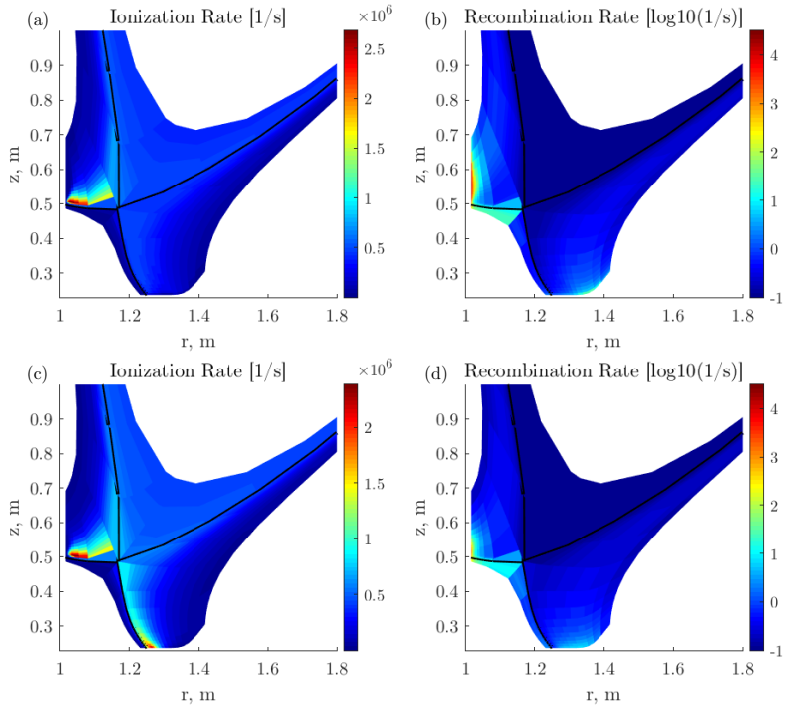

Figure 4.3. Ionizaton and recombination rates in the divertor region. Figures 4.3(a) and 4.3(b) show the ionization and recombination rates for the inverse case, respectively. Figures 4.3(c) and 4.3(d) show the standard case.

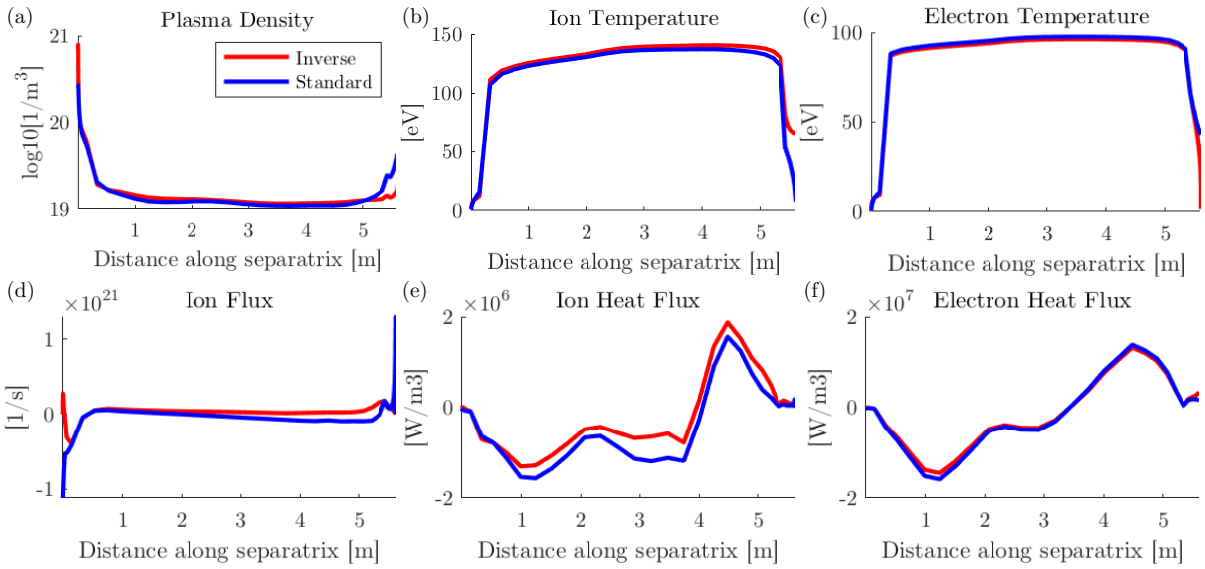

Figure 4.4. Plasma parameters along the field line in the SOL, just outside the separatrix. The field line starts at the inner target and ends at the outer target. Red and blue lines correspond to the inverse and standard cases, respectively.

Other than this feature, however, these profiles for the inverse and standard cases are very similar. Figures 4.2(b) and 4.2(e) show low temperatures throughout the divertor, particularly at the inner plate. Figures 4.4(b) and 4.4(c) also show lowered temperatures in the divertor regions only. This is consistent with the recombination rates shown in Figures 4.3(b) and 4.3(d); there is high recombination at the targets corresponding to the region of sub-eV electron temperature.

Parameters along the field line, taken just outside the separatrix, are shown in Figure 4.4; once again, the inverse and standard cases look similar. As seen in Figure 4.4(d), ion flux to the target drops for inverse sheath and remains high for the standard case, which is consistent with our boundary conditions.

4.3.2 Discussion

We do not observe a substantial improvement on the transition to detachment resulting from the influence of the inverse sheath. The results of our simulations are inconsistent with hypotheses proposed in other studies, where it was suggested that a divertor plasma could detach under inverse sheath conditions because "[a] target plasma of sub-eV temperature will form as long as the plasma is collisional ... and the emission is strong enough to maintain an inverse sheath [5]." However, the transition to detachment is

not that simple because of the strong dependence of detachment on both upstream plasma pressure and incoming heat flux to the divertor. Regardless of the characteristics of the plasma sheath, upstream plasma pressure has a major effect on plasma temperature at the target [13], which is critical in the transition to detachment because temperature must be low enough to "turn on" recombinative processes and detach the plasma. Since we observe a high heat flux in the attached outer divertor and a low heat flux in the weakly detached inner divertor for both cases, it is evident that there is no extreme cooling induced by the inverse regime at the outer target, and the transition to detachment is not affected by the plasma sheath. Further, we do not observe significant differences in other plasma parameters throughout the device, which remain largely the same for both cases.

While the inverse sheath alone cannot produce detachment, we observe a marginal decrease in heat flux to the already detached target, meaning that the detachment that has already been reached can be slightly improved by the conditions induced by the inverse sheath. However, we also note that for these conditions, the inverse sheath has no favorable effect on the attached plasma in the outer divertor. As we have noted, heat loading to the target is increased for this regime due to the unbounded electron flux, which means that the influence of the inverse sheath is actually damaging to the target unless the plasma is already detached.

Although we do not anticipate the inverse sheath can be used as a direct path to detachment, we believe there is merit in the application of this regime to tokamak operation, and these results are substantial enough to warrant further investigation. In our simulations, we observe reduced heat loads at the target for already detached plasma, which is advantageous in a tokamak regime because erosion of material targets is reduced, limiting long-term damage to the machine and minimizing impurity contamination into the confined plasma. While we observe energy loss to the targets via charge exchange with neutrals, this is unavoidable and not a direct issue with the inverse sheath *per se*, and since it is observed under all operating conditions, it is not a limiting concern for the inverse sheath. Because we have observed improved conditions in the case where the plasma is already detached, further work on whether this regime can improve divertor performance will focus on regimes with detached or semi-detached plasmas in both divertors. This will be achieved by exploring different parameter spaces to provide a more robust understanding of how divertor and other operating conditions will be affected with respect to the inverse

sheath.

We have investigated the effect of the newly-proposed inverse sheath on tokamak divertor detachment. Lower heat loads to the target induced by the inverse sheath in detached plasmas are favorable for a fusion device, but we do not see a full transition to detachment due to the ultimate dependence on upstream plasma density and incoming heat flux, rather than the effects of the plasma sheath. We expand our study over a broad range of plasma parameters (in this case, the density) to assess what effect, if any, the inverse sheath has in various stages of plasma detachment.

4.4 Density scan

4.4.1 Results

Results of simulations with impurity radiation are shown in Figure 4.5. Figure 4.5(a,b) show the total heat load to the targets and electron temperature at the targets, just outside the separatrix, across increasing n_{ce} for the standard sheath. Figure 4.5(c,d) show the same quantities for the inverse sheath. There are two "branches" of solutions in the solution set for the inverse sheath, separated by a bifurcation across increasing n_{ce}.

For the standard case, total heat load to the target is consistently higher in the outer divertor, and becomes comprable with the heat load to the inner divertor at higher n_{ce}. Electron temperature at the targets remains higher in the outer divertor than the inner divertor, even at higher n_{ce}. As shown in Figure 4.5(a) and Figure 4.5(b), the variation in plasma parameters is smooth for the standard sheath. Both the total heat load to the target and the electron temperature near the strike point decrease as n_{ce} is increased.

Results for plasmas with an inverse sheath show higher heat load to the outer divertor than the inner divertor at lower values of n_{ce}, and lower heat load to the outer divertor at higher n_{ce}. Electron temperatures at the separatrix are always higher at the outer divertor than the inner divertor in the inverse sheath regime. There is bifurcation in the solution set for plasmas with the inverse sheath, which is visible in Figure 4.5(c) and Figure 4.5(d). At this bifurcation, the heat load to the outer divertor abruptly drops and becomes lower than the heat load to the inner divertor.

Results of simulations without impurity radiation for standard and inverse sheaths are shown in Figure

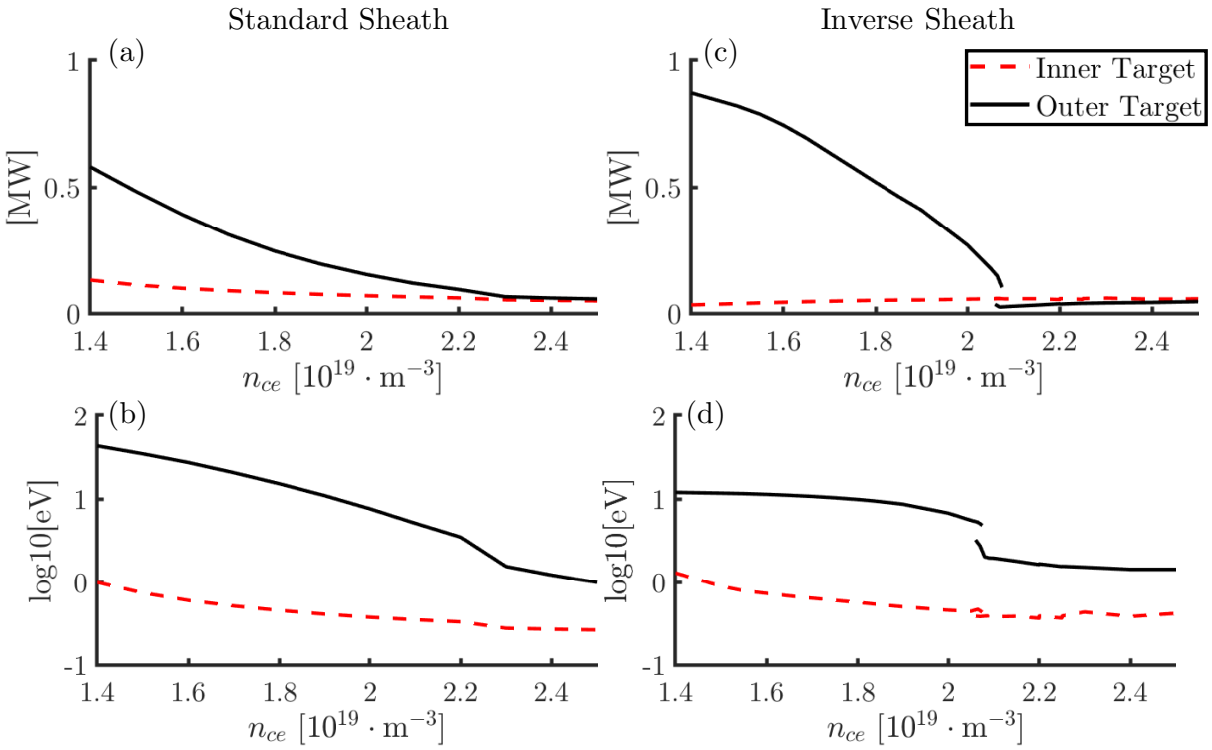

Figure 4.5. Results from the parameter scan for plasmas with a fixed fraction nitrogen impurity radiation of 3%. Figure 4.5(a) shows the total heat load on the target for the standard sheath, while Figure 4.5(b) shows the electron temperature at the strike point for the standard sheath. Figure 4.5(c) and Figure 4.5(d) show the total heat load on the target and the electron temperature at the strike point for the inverse sheath, respectively. The bifurcation is visible in both figures. In both sets of figures, data for the inner targets is shown with dotted red lines and data for the outer targets is shown with solid black lines.

4.6. Each figure shows the variation in the respective plasma parameter across increasing n_{ce}. Figure 4.6(a), Figure 4.6(b), and Figure 4.6(c) show the results for cases with standard sheaths, while Figure 4.6(d), Figure 4.6(e), and Figure 4.6(f) correspond to cases with inverse sheaths.

Each of the inverse sheath solution sets without impurity radiation feature three different "branches", where there are bifurcations between branches in the solution set. Two of the "branches" feature considerable overlap where two distinct solutions exist for the same n_{ce} input value. As n_{ce} is increased, there is a gap between the branches where the bifurcation jumps from the second branch of solutions to the third branch. This behavior is observed in all three of the quantities related to the inverse sheath shown in Figure 4.6, and the recombination rates shown in Figures 4.8 and 4.9.

Figure 4.6(a) and Figure 4.6(d) show the total heat load to the targets for the standard and inverse cases, respectively. The variation of the total heat load is smooth for the standard sheath, with a higher total heat load to the outer divertor and lower heat load to the inner divertor. For the inverse case, there is a bifurcation the variation in the total heat load at both targets. Total heat load to the outer divertor monotonically decreases with increasing n_{ce}, while total heat load to the inner divertor increases slightly before leveling out. At lower n_{ce}, the total heat load to the outer target is higher than at the inner target; as n_{ce} is increased, the total heat load to the inner target becomes higher (but still comparable) than the heat load to the outer target. Despite these differences in trends, if the regimes are compared across n_{ce} (the red dashed line in Figure 4.6(a) to the red dashed line in Figure 4.6(d), and the same for the black solid line in each figure), the magnitude of the total heat load to each target is similar.

The maximum heat flux at the targets for the standard case is shown in Figure 4.6(b), and inverse case in Figure 4.6(e). Similar to the trends for the total heat load to the target for the standard case, the variation in the peak heat flux at the targets smoothly decreases, with consistently higher peak flux to the target in the outer divertor than the inner divertor. For the inverse sheath, the bifurcation seen in the total heat load to the targets appears.

Electron temperatures at the strike point for each simulation set can be seen in Figure 4.6(c) for the standard case and Figure 4.6(f) for the inverse case. Once again, the variation in electron temperature for the standard case is smooth, with consistently higher temperatures at the outer target than the inner

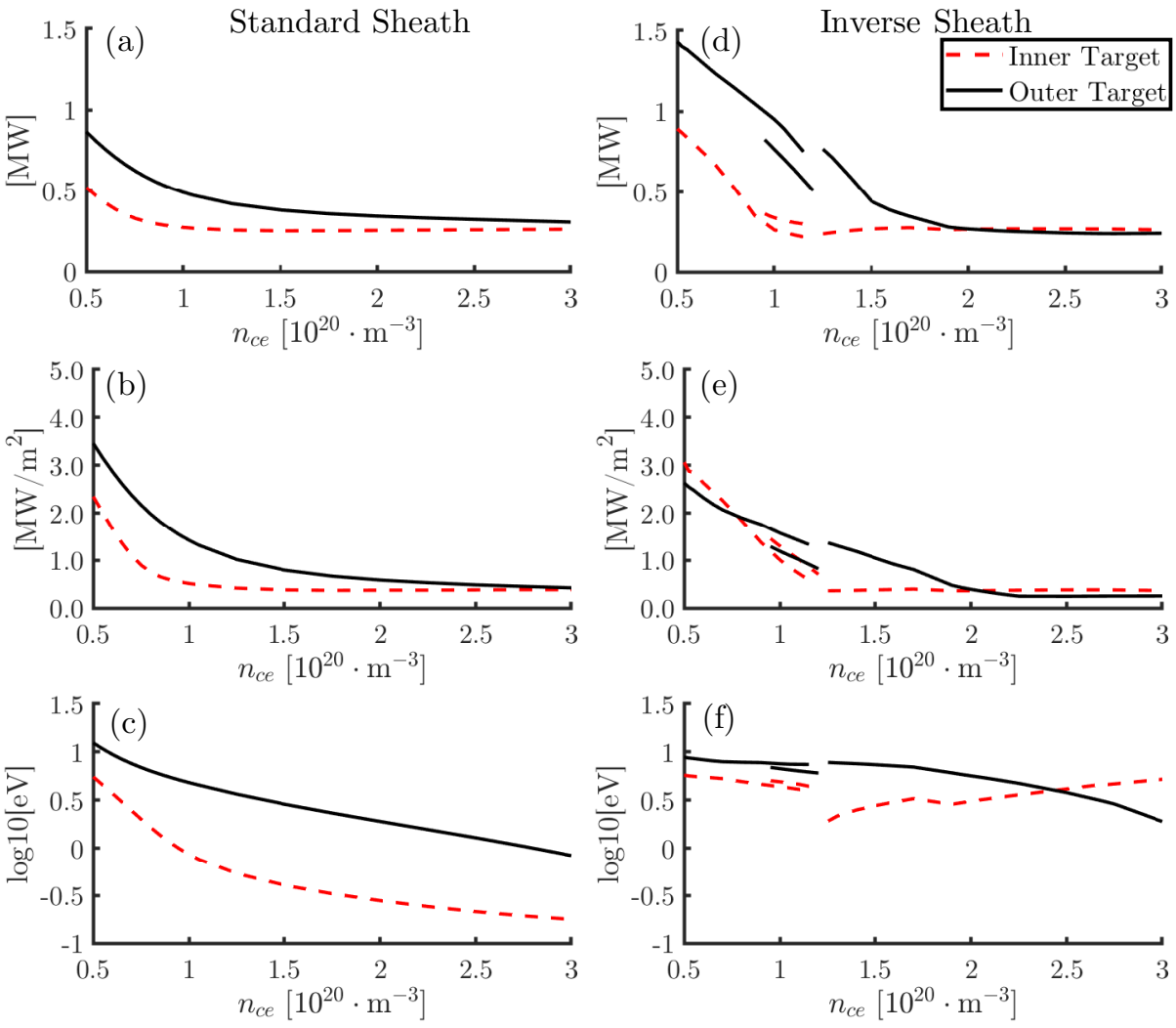

Figure 4.6. Plasma parameters as n_{ce} is varied for the standard and inverse sheath simulation sets with no impurity radiation. The left column (Figure 4.6(a), (b), and (c)) show the total heat load, maximum heat flux, and strike point electron temperature at the targets for the standard sheath, while the right column (Figure 4.6(d), (e), and (f)) show the same quantities for the cases with an inverse sheath. In both sets of data, the dashed red lines correspond to the inner target, while the solid black lines correspond to the outer target. The bifurcation in the simulation set can be seen in the inverse sheath solution set in all three quantities shown.

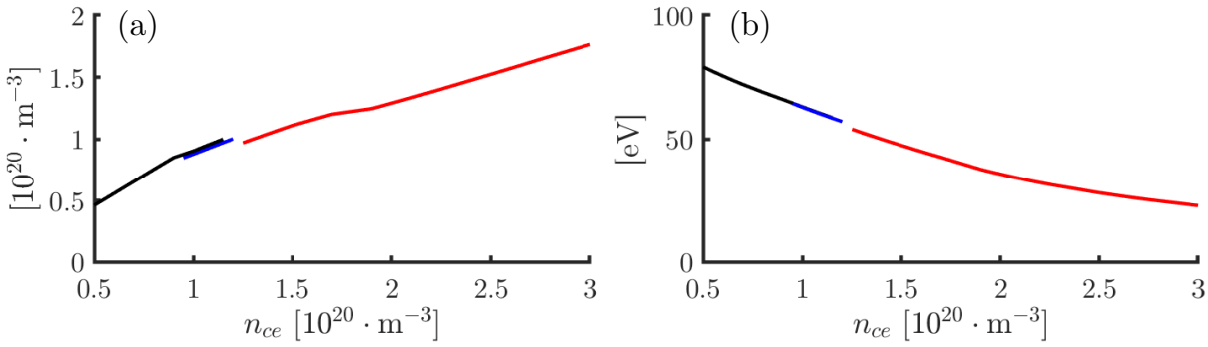

Figure 4.7. Plasma density and electron temperature at the midplane for plasmas with inverse sheaths and no impurity radiation, with values taken just outside the separatrix. The three "branches" correspond to the three bifurcated "branches" seen in the divertor, each denoted with a different color. Note that in (b) there is significant overlap on Branch 1 and Branch 2, and the lines appear to match exactly.

target. The bifurcation is present in the variation in electron temperature for the inverse case. At lower n_{ce}, temperatures at the outer target are higher than temperatures at the inner target, but as n_{ce} is increased, the temperatures at the outer target decrease and become lower than the temperatures at the inner target, which increase.

Plasma density and electron temperature at the midplane for plasmas with inverse sheaths are shown in Figure 4.7. The different "branches" in the bifurcation (as it is observed in the divertor) are shown in different colors. Unlike the variation of plasma parameters in the divertor, the bifurcation is not pronounced at the midplane - the change in parameters as n_{ce} is varied is relatively smooth.

Total recombination rate in the divertor for both the inverse and standard sheaths with no impurity radiation are shown in Figure 4.8. Both the standard and inverse sheaths show recombination rate increases as core density is increased, and the bifurcation can be seen in the inverse set. The branch with lower recombination rate corresponds to the branch in Figure 4.6 with higher heat fluxes and temperatures in the inner divertor.

Total recombination rate in the inner and outer divertors for the inverse sheath with no impurity radiation are shown in Figure 4.9. Recombination rate increases as core density is increased, and the bifurcation can be seen at lower n_{ce}. There is another abrupt change in the total recombination rate at

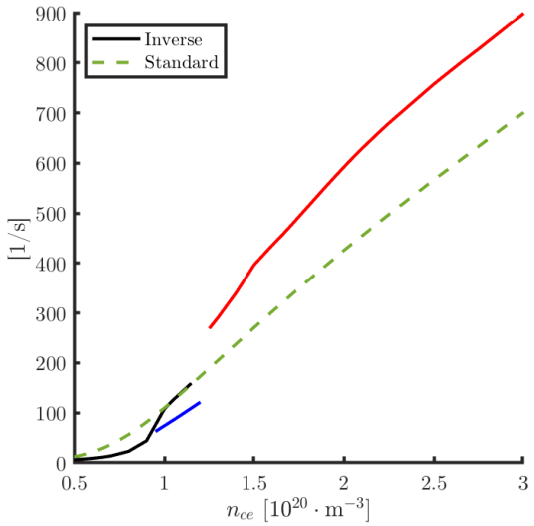

Figure 4.8. Total recombination in the divertor for plasma with standard sheath (shown in a green dashed line) and plasma with inverse sheath (shown in solid lines), both with no impurity radiation. The bifurcation in the inverse sheath solution set is present. Each "branch" of the bifurcation is shown in a different color.

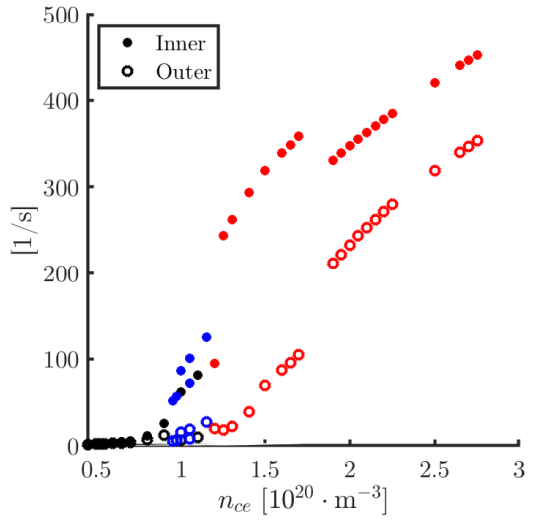

Figure 4.9. Total recombination rate in each divertor for plasma with inverse sheath and no impurity radiation. The inner divertor is shown in solid dots, while the outer divertor is shown with empty circles. Each "branch" of the bifurcation is shown in a different color.

higher values of n_{ce} where recombination rate in the inner divertor suddenly drops and recombination rate in the outer divertor suddenly increases. Particle density before and after this sudden change can be seen in Figure 4.10.

4.4.2 Discussion

Divertor plasma parameters have been assessed for plasmas with both standard and inverse sheaths. Plasmas with the standard sheath feature smooth variation in parameters, while variation in parameters bifurcates for plasmas with inverse sheaths. As mentioned previously, similar bifurcations in plasmas with standard sheaths have been observed in simulations and experiments [69–71] and have been attributed to phenomena associated with plasma recombination, impurity radiation, drifts, or some interplay of transport coefficients as they change throughout the device. The simulations shown here feature no drifts and use constant transport coefficients, which rule out the last two options as causes for this bifurcation. Since we have shown that this bifurcation persists both with and without impurity radiation, it is not due to impurity radiation alone, leaving the recombination process as the most likely suspect for the cause of this bifurcation.

In these simulations, there are "jumps" in different plasma parameters across the solution set that are seen in heat losses and heat fluxes, temperature, and recombination rate, resulting in solution "branches" that are characteristic of bifurcations. Bifurcations are a consequence of nonlinearity; this system is highly nonlinear, so it is feasible that there can be multiple branches of solutions, and multiple different solutions for one set of input parameters. Physically, this is likely related to a redistribution of particles that causes major changes to the heat fluxes and heat losses in the system, associated with the sensitivity of recombination with temperature. A temperature fluctuation could significantly change the recombination rate, leading to changes in the distribution of density and a rearrangement of particles, which would result in different heat losses and heat fluxes in each state.

The recombination process is inextricably linked with neutrals. Neutrals are important because they provide an important mechanism for dissipative heat loss in the divertor via neutral-induced radiation. In the standard regime, ion flux to the targets is neutralized, neutrals are produced via this recycling process, and an inventory of neutrals develops that will mitigate the incoming heat load. This is not the case in the

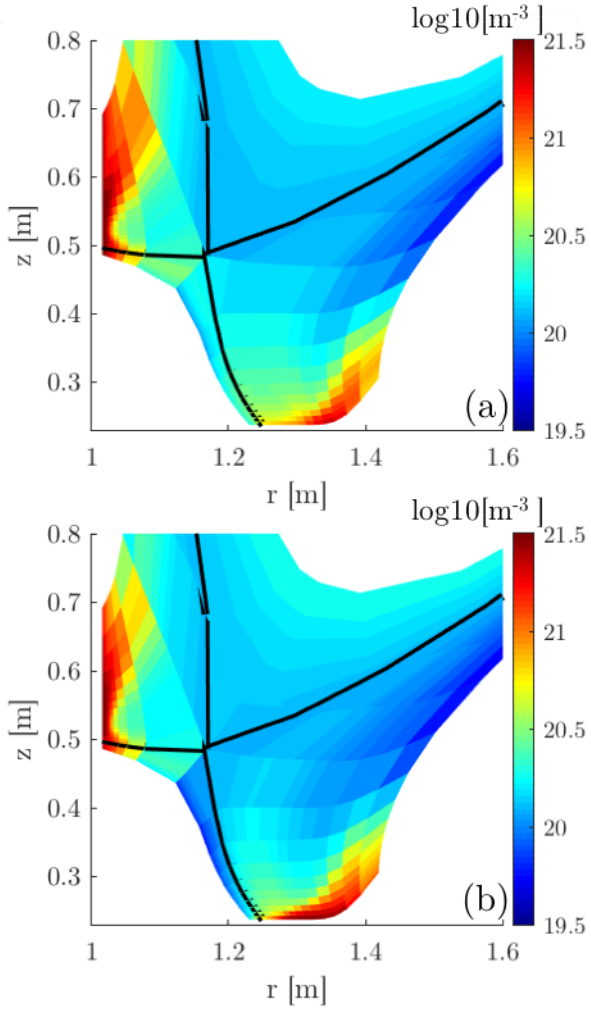

Figure 4.10. Particle density in the divertor for solutions spanning the "jump" in recombination rate across $n_{ce} = 1.7e20$ m^{-3} to $n_{ce} = 1.9e20$ m^{-3}. Figure 4.10(a) corresponds to the branch of the bifurcation at $n_{ce} = 1.7e20$ m^{-3}, prior to the redistribution in density, while Figure 4.10(b) corresponds to the branch at $n_{ce} = 1.9e20$ m^{-3}, after the redistribution in density. The thick black line traces the separatrix.

inverse sheath regime; since the inverse sheath will eliminate incoming ion flux, there will be no recycling at the targets, and no neutrals will be produced. Without this neutral source at the target, the primary source of neutrals in the system would be from the volumetric recombination process, which is highly dependent on temperature. This dependence on recombination means that small temperature fluctuations can have major effects on the overall system: if the temperature rises, even slightly, recombination will decrease, meaning neutral inventory will decrease. With fewer total neutrals, heat losses from radiation will decrease, the temperature will rise, and the effect of the initial perturbation will be amplified.

This dependence on temperature can be seen in the data for plasmas with inverse sheaths with no impurity radiation, shown in Figure 4.6(d,e,f). On the third "branch" of solutions visible in these solution sets (corresponding to the highest values of n_{ce} shown), total heat load to the targets and peak heat flux are relatively constant as n_{ce} increases, which are trends also observed with increasing n_{ce} in the standard case with no impurity radiation and in both cases with impurity radiation. Similarly, at the outer target, electron temperature at the strike point falls as n_{ce} is increased, but unlike these other cases, electron temperature at the strike point rises at the inner target as n_{ce} is increased, seen in Figure 4.6(f). This trend seems counter-intuitive: temperatures at the inner target rise, but heat load and heat flux to the inner target remain fairly constant. However, the rising temperatures can be attributed to the strong dependence of temperature on recombination, and the effects of this change are compensated through a redistribution of particles between the inner and outer divertor legs, shown in Figure 4.10.

As shown in Figure 4.9, there is an additional bifurcation in the red "branch" of solutions that occurs roughly where a temperature fluctuation is observed in Figure 4.6(f). At this value of n_{ce}, recombination rate in the inner divertor abruptly drops and recombination rate in the outer divertor abruptly increases. This behavior follows similar trends to the temperature variation in Figure 4.6(f), where temperatures at the inner target rise (where recombination rate has dropped) and temperatures at the outer target drop (where recombination rate has increased). This is consistent with the strong dependence of recombination on temperature, where an initial perturbation in temperature causes a major impact on the system. For the inner target, an initial increase in temperature decreases recombination rate, which will increase temperature further, which will decrease recombination, and so forth. The opposite effect is observed at the outer target, with a decrease in temperature leading to an increase in recombination.

However, a dramatic change in the variation of parameters as a result of this bifurcation in the recombination rate is not observed in the total heat load to the target or the peak heat flux to the target, shown in Figure 4.6(d,e). Across the bifurcation "gap", variation in parameters appears to be smooth. This can be attributed to a redistribution of density, shown in Figure 4.10, and observable in the trends in the recombination rate: after the redistribution, there are fewer particles in the inner divertor contributing to the recombination rate, so the recombination rate decreases, and more particles in the outer divertor contributing to the recombination rate, so the recombination rate increases. Because the density redistributes to compensate for the changes caused by the temperature fluctuation, variation in parameters remains smooth (and relatively constant) and the bifurcation is not observed.

In the cases with no impurity radiation, shown in Figure 4.6(d,e,f), and Figure 4.8, there is a gap between the lower and upper solution branches where no stationary solution exists. Since a time-dependent solution would exist in this region, we will investigate the transition from one regime to another by running UEDGE in time-dependent mode. We plan to approach this in future studies, using the same boundary conditions and same sets of input parameters used in this paper and using the time-dependent UEDGE mode. Additionally, we also notice that no stationary solution exits in a gap in the solution set across the bifurcation in the red "branch" in Figure 4.9; this transition will also be investigated using UEDGE in time-dependent mode.

Profiles at the midplane indicate this bifurcation has minimal impact on plasma parameters in the scrape-off layer. The effects of the bifurcation are localized to the divertor, since plasma parameters at the target and recombination are both affected by this bifurcation, but upstream profiles at the midplane are not.

4.5 Inverse sheath instability

4.5.1 1D Physical Model

To shed light on the physics of the recombination-induced bifurcation observed in our 2D numerical modeling, we consider a 1D model of the heat flux q_{SOL} propagating through plasma with an inverse sheath at the target (see Figure 4.11). We will adopt the "closed box" approximation, where we assume the given averaged density of hydrogen ions and neutrals (atoms) and 100% neutral particle reflection

Figure 4.11. Schematic view of the 1D model setup.

from the target. In Figure 4.11, we show the situation where the electron temperature at the target, T_d, is low enough $\sim$ 1 eV and below) so that three-body plasma recombination becomes important. In this case, neutrals, originated in the course of plasma recombination, penetrate into the relatively hot upstream plasma (with the temperature T_{ion} $\sim$3-4 eV), where they are ionized and simultaneously dissipate the heat flux to the target due to line radiation.

The neutral flux, j_N, is determined by the neutral source due to three-body plasma recombination:

$$j_N = \int_0^\infty \kappa_{rec}(T) n^3 \, \mathrm{dz}, \tag{4.6}$$

where $\kappa_{rec}(T) = \hat{k}_{rec}/T^{9/2}$ is the recombination rate constant, $\hat{k}_{rec}$ is the normalization constant, and n is the plasma density.

4.5.2 Small neutral pressure

We will assume that the temperatures of electrons, ions, and neutrals are equal, but neutral density and therefore, neutral pressure is much smaller than the plasma density and pressure (this will be shown for the parameter range of interest later). Since total plasma and neutral pressure is constant along the magnetic field lines, in this case we can assume that the plasma pressure is constant along the magnetic field, $P = 2nT = \text{const}$. Therefore, Eq. (4.6) can be written as:

$$j_N = \left(\frac{P}{2}\right)^3 \hat{k}_{rec} \int_0^\infty T(z)^{-15/2} \, \mathrm{dz}. \tag{4.7}$$

For the temperature range in the divertor plasma, the temperature profile is determined by the heat

flux into this region, $q_{SOL} - q_{ion}$, and the electron heat conduction,

$$q_{SOL} - q_{ion} = \kappa_e(T)\sin^2(\alpha)\frac{\mathrm{dT}}{\mathrm{dz}}, \tag{4.8}$$

where $\kappa_e(T) = \hat{k}_e T^{5/2}$ is the electron heat conduction coefficient, $\hat{k}_e$ is the normalization constant, and $\alpha \sim 0.1$ is the inclination angle of the magnetic field line to the divertor target. The dissipation of the heat due to neutral ionization/radiation, q_{ion}, can be related to the neutral flux into the ionization region, j_N, via the "neutral ionization cost", $E_{ion} \sim 30$ eV [21]:

$$q_{ion} = E_{ion} j_N. \tag{4.9}$$

Taking into account that the neutral density is small, for inverse sheath conditions the only channel for dumping the heat coming to the target is the electron exchange flux, since ion-surface interaction is eliminated. So, at the target, we have

$$q_{SOL} - q_{ion} = \left(\frac{P}{2}\right)\gamma_e\left(\frac{T_d}{m}\right)^{1/2}\sin(\alpha), \tag{4.10}$$

where γ_e is the electron heat transmission coefficient and m is the electron mass.

To determine q_{ion}, we can combine Eq. (4.8) and Eq. (4.10) such that:

$$\begin{aligned} 1 &= \left(\frac{\kappa_e(T)\sin^2(\alpha)\frac{\mathrm{dT}}{\mathrm{dz}}}{\left(\frac{P}{2}\right)\gamma_e\left(\frac{T_d}{m}\right)^{1/2}\sin(\alpha)}\right) \\ \Rightarrow \mathrm{dz} &= \left(\frac{\hat{k}_e T^{5/2}\sin(\alpha)}{\left(\frac{P}{2}\right)\gamma_e\left(\frac{T_d}{m}\right)^{1/2}}\right)\mathrm{dT} \end{aligned}$$

Incorporating this into the expression for neutral flux Eq. (4.7), we see that

$$\begin{aligned} j_N &= \left(\frac{P}{2}\right)^3 \hat{k}_{rec} \int_{T_d}^{T} T^{-15/2} \left(\frac{\hat{k}_e T^{5/2} \sin(\alpha)}{\left(\frac{P}{2}\right) \gamma_e \left(\frac{T_d}{m}\right)^{1/2}} \right) \mathrm{dT} \\ &= \left(\frac{P}{2}\right)^2 \left(\frac{\hat{k}_e \sin(\alpha)}{\left(\frac{P}{2}\right) \gamma_e \left(\frac{T_d}{m}\right)^{1/2}} \right) \int_{T_d}^{T} T^{-5} \mathrm{dT}, \end{aligned}$$

which gives

$$j_N = \left(\frac{P}{2}\right)^2 \left(\frac{\hat{k}_e \sin(\alpha)}{\left(\frac{P}{2}\right) \gamma_e \left(\frac{T_d}{m}\right)^{1/2}} \right) \frac{-1}{5} (T^{-4} - T_d^{-4}) = \left(\frac{P}{2}\right)^2 \left(\frac{\hat{k}_{rec} \hat{k}_e \sin(\alpha)}{\gamma_e T_d^4 (\frac{T_d}{m})^{1/2}} \right) \frac{1}{5},$$

where we can see that the main contribution of neutrals comes from $T \sim T_d$, since for the majority of the divertor plasma, $T \gg T_d$. This means that heat dissipation term q_{ion} can be written as

$$q_{ion} = \left(\frac{P}{2}\right)^2 \left(\frac{E_{ion} \hat{k}_{rec} \hat{k}_e \sin(\alpha)}{\gamma_e T_d^4 (\frac{T_d}{m})^{1/2}} \right) \frac{1}{5}.$$

With this, we will consider the electron exchange flux, Eq. (4.10), at the target, where:

$$q_{SOL} = \left(\frac{P}{2}\right) \gamma_e \left(\frac{T_d}{m}\right)^{1/2} \sin(\alpha) + \left(\frac{P}{2}\right)^2 \left(\frac{E_{ion} \hat{k}_{rec} \hat{k}_e \sin(\alpha)}{\gamma_e T_d^4 (\frac{T_d}{m})^{1/2}} \right) \frac{1}{5}. \tag{4.11}$$

It is useful to introduce a parameter θ_d, related to the temperature T_d, where

$$\theta_d = \left(\frac{P}{2 q_{SOL}} \right) \gamma_e \left(\frac{T_d}{m}\right)^{1/2} \sin(\alpha),$$

such that Eq. (4.11) now reads

$$1 = \theta_d + \left(\frac{P}{2}\right)^3 \left(\frac{E_{ion}\hat{k}_{rec}\hat{k}_e \sin^2(\alpha)}{T_d^4}\right)\frac{2}{9\theta_d} \Rightarrow 0 = \theta_d^2 - \theta_d + \left(\frac{P}{2}\right)^3 \left(\frac{E_{ion}\hat{k}_{rec}\hat{k}_e \sin^2(\alpha)}{T_d^4 q_{SOL}^2}\right)\frac{1}{5},$$

or

$$\theta_d = \frac{1}{2}\left(1 \pm \sqrt{1 - \frac{4}{5}\left(\frac{P}{2}\right)^3 \left(\frac{E_{ion}\hat{k}_{rec}\hat{k}_e \sin^2(\alpha)}{T_d^4 q_{SOL}^2}\right)}\right). \tag{4.12}$$

For simplicity, we introduce a new parameter θ_*, such that

$$\theta_*^8 = \left(\frac{P}{2}\right)^{11} \left(\frac{4E_{ion}\hat{k}_{rec}\hat{k}_e \sin^{10}(\alpha)}{5q_{SOL}^{10} m^4}\right)$$

and Eq. (4.12) can be written as

$$\theta_d = \frac{1}{2}\left(1 + \sqrt{1 - \left(\frac{\theta_*}{\theta_d}\right)^8}\right) \equiv 1 - \frac{q_{ion}}{q_{SOL}} = \mathrm{F}(\theta_d, \theta_*), \tag{4.13}$$

where we have only considered the physically meaningful sign in front of the square root. The LHS and RHS of the expressions in Eq. (4.13) describe the heat flux to and from the plasma region, respectively. Real solutions for the RHS of Eq. (4.13) require a positive radicand, such that $1 - \left(\frac{\theta_*}{\theta_d}\right)^8 \geq 0$, where the lower limit on θ_d occurs where $\theta_*/\theta_d = 1$. From Eq. (4.13), this corresponds to a value of $\theta_d = 1/2$.

With this expression, we can see that depending on the magnitude of θ_*, Eq. (4.13) has one solution for $\theta_* < 1/2$, two solutions for $\theta_{crit} > \theta_* > 1/2$, and no solutions for $\theta_* > \theta_{crit}$.

To find the value of θ_{crit}, the derivative of Eq. (4.13) with respect to θ_d is

$$1 = \frac{2\left(\frac{\theta_*}{\theta_d}\right)^8}{\theta_d\sqrt{1-\left(\frac{\theta_*}{\theta_d}\right)^8}} \tag{4.14}$$

and Eq. (4.13) can be written as

$$\theta_*^8 = \theta_d^8\left[1-(2\theta_d-1)^2\right]. \tag{4.15}$$

Combining these two expressions, we find an equation for the intersection of the two parameters in Eq. (4.13):

$$1 = \left(\frac{5}{2}\theta_d - 1\right)(2\theta_d - 1), \tag{4.16}$$

where the only relevant solution is $\theta_d = 9/10$. From Eq. (4.15), we obtain a corresponding value of $\theta_* = \theta_{crit} = \frac{9}{10}(\frac{3}{5})^{1/4}$.

From Eq. (4.13) (and observable in Section 4.5.2), stable solutions of Eq. (4.13) are only possible for a very limited range of q_{ion}/q_{SOL}:

$$q_{ion}/q_{SOL} < 1/10. \tag{4.17}$$

4.5.3 Estimate of neutral pressure

In the previous section, we assume that the contribution of neutral pressure, P_n, to the total pressure P is small: $p = P_N/P \ll 1$. Here, we provide the estimate supporting this assumption.

First, we note that the neutral flux j_n can be found from the neutral momentum balance equation

$$0 = \frac{\mathrm{dP_N}}{\mathrm{dz}} + MK_{CX}(T)nj_N, \tag{4.18}$$

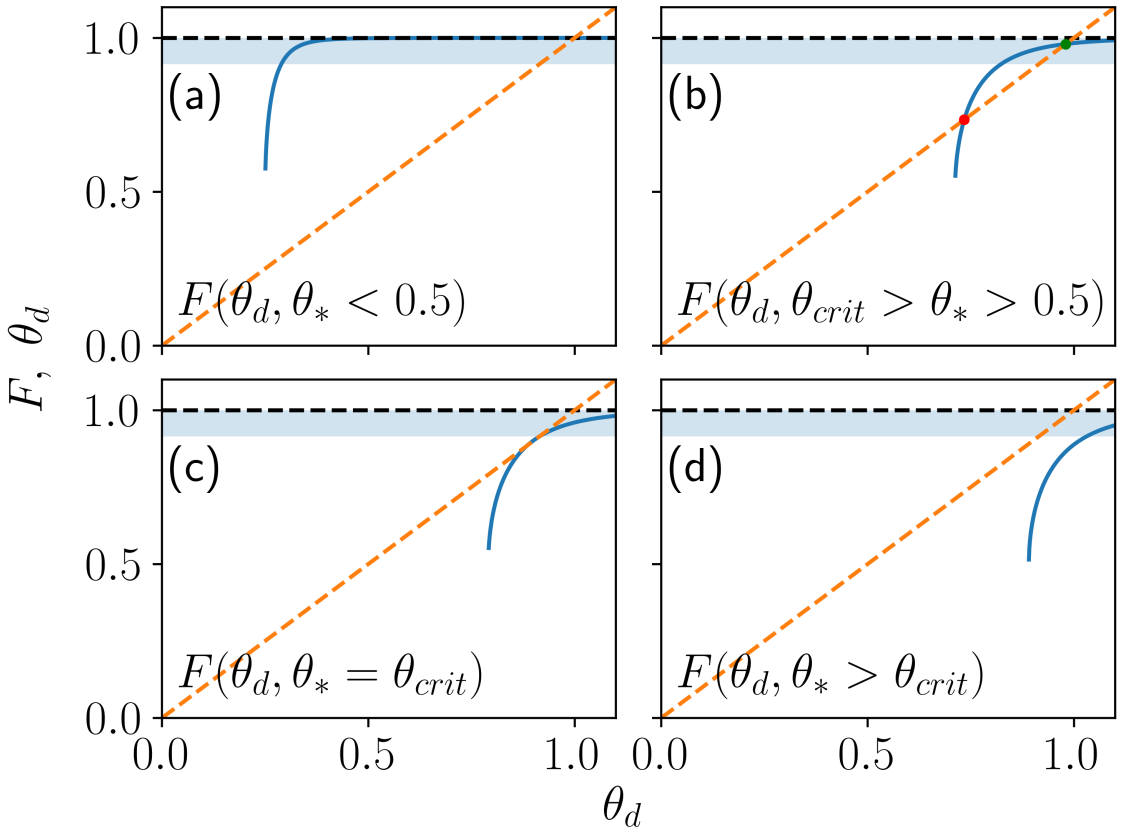

Figure 4.12. The graphical "solutions" of Eq. (4.13) for different values of θ_*. The line for θ_d is in orange dash, and the curve for F is in solid blue. The "red" and "green" dots in (b) correspond to the unstable and stable solutions. The fact that the "red" solution is unstable could be illustrated by small "virtual" positive (negative) departure of θ_d from "red" solution which results in the heat flux into near-target plasma becoming larger (smaller) that the heat from plasma to the target, promoting further increase (decrease) of θ_d. The narrow range of stable solutions identified in Eq. (4.17) is highlighted.

where $K_{CX}(T)$ is the charge-exchange collision rate and M is the ion/atom mass. Expressing j_N in terms of q_{ion}, recall Eq. (4.9), such that Eq. (4.18) can be rewritten as

$$\frac{\mathrm{dp}}{\mathrm{dz}} = -K_{CX}(T)\left(\frac{M}{T}\right)\left(\frac{q_{ion}}{E_{ion}}\right). \tag{4.19}$$

Then, from Eq. (4.8) and Eq. (4.19) and taking into account that the neutral density in the ionization region is negligibly small, we find

$$p(z=0) = \frac{1}{3}\frac{T_{ion}}{E_{ion}}\frac{q_{ion}}{q_{SOL}}\frac{M}{T_{ion}}K_{CX}(T_{ion})\kappa_e(T_{ion})\sin^2(\alpha). \tag{4.20}$$

Taking into account the inequality in Eq. (4.17) for $T_{ion} \approx 4$ eV, we find from Eq. (4.20) that $p(z=0) \sim 10^{-2} \ll 1$, which justifies the assumption of a small contribution of the neutral pressure made in the previous section.

4.5.4 Solutions for $\theta_* > \theta_{crit}$

In Section 4.5.2, we find that the solution of our 1D model and small contribution of neutral pressure is only possible for $\theta_* < \theta_{crit}$. Since $\theta_* \propto P^{11/8}/q_{SOL}^{5/4}$, we conclude that for a given q_{SOL}, such solutions only exist for the pressure range $P < P_{crit}$. A similar situation was found in a 1D model for the case of plasma 3-body recombination for "standard" sheath conditions [9]. If we keep the pressure $P > P_{crit}$ fixed by adding particles in the domain, plasma recombination will ramp-up, temperature at the target will continue to drop due to high neutral heat conduction, and the solution will "collapse" to virtually zero temperature at the target. However, in the "closed box" approximation, where plasma pressure is not fixed, but determined by the averaged ion/neutral density in the domain, an onset of strong plasma recombination causes the "condensation" of plasma/neutral particles in the cold region at the vicinity of the target, which reduces pressure and "stabilizes" the solution. In a more real 2D model, neutrals will leak from the vicinity of the target due to perpendicular fluxes, which stabilize the plasma pressure near the separatrix at $P \approx P_{crit}$ (e.g. see [9],[16]). The bifurcation caused by the onset of 3-body plasma recombination results in an increase in neutral density at the target with a corresponding decrease in

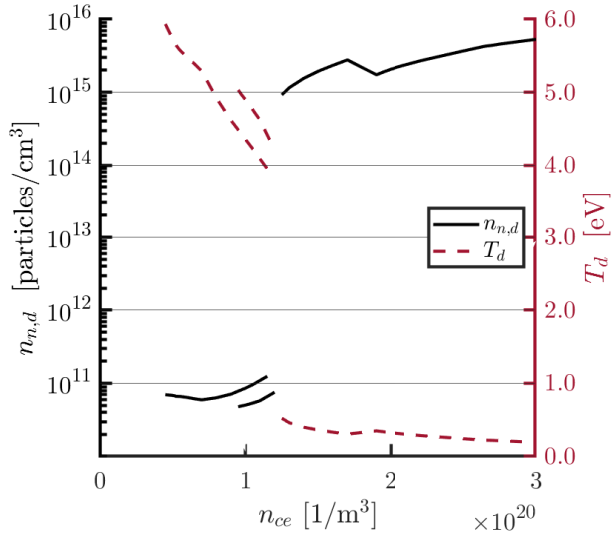

Figure 4.13. Neutral density at the target (black solid line) with electron temperature at the target, just outside the separatrix (red dashed line) across the core-edge density scan for simulations with an inverse sheath, without impurity radiation.

electron temperature at the target (just outside the separatrix) that is observed in the simulation set, shown in Figure 4.13.

4.6 Conclusions

In conclusion, we have investigated the impact of the inverse sheath on divertor plasmas and discovered multiple bifurcations in the solution set. These bifurcations are not observed in the solution set for plasmas with standard sheaths, indicating that the presence of an inverse sheath can cause bifurcations in divertor plasmas. We have explored the mechanism which causes this bifurcation and shown that it is related to temperature sensitivities associated with plasma recombination that leads to a redistribution of particles in the divertor. The effects of this bifurcation are localized to the divertor and do not appear throughout the device. The bifurcation observed in our 2D simulations is consistent with a 1D estimate that indicates the existence of two distinct branches of stable solutions corresponding to low and high neutral pressures that is dependent on target temperature.

Acknowledgments

We would like to thank Dr. Michael Campanell and Dr. Ilon Joseph (LLNL) for useful discussions. This work was supported by the U.S. Department of Energy under DE-FG02-04ER54739.

Chapter 4, in part, is a reprint of the material as it appears in "Influence of the inverse sheath on divertor plasma performance in tokamak edge plasma simulations" in *Contributions to Plasma Physics*, 60(5-6), p.e201900097, by R. Masline, R.D. Smirnov, and S.I. Krasheninnikov (2020), and in "Simulations of divertor plasmas with inverse sheaths" in *Physics of Plasmas*, 27(9), p.092505 by R. Masline, R.D. Smirnov, and S.I. Krasheninnikov (2020). The dissertation author was the primary investigator and author of this material.

Chapter 5

Energy and particle balance during plasma detachment in a long-leg divertor configuration

5.1 Introduction

Managing heat and particle exhaust in tokamak devices remains an open challenge in the development of next-generation fusion machines. Present understanding indicates that the operational regime best suited for handling the extreme conditions of the plasma exhaust by allowing for both heat removal and suppression of incoming particle and heat fluxes is the so-called "detached" divertor regime. Virtually all present-day tokamaks and future reactors will operate in this detached divertor regime, where a collection of atomic and radiative processes nearly extinguishes plasma heat and particle flux before it reaches the divertor target.

While many aspects of the complex and multifaceted edge plasma remain poorly understood, the general physics of the mechanisms of the "detachment" of plasma from the material surfaces in the "standard" divertor regime have been explained [74, 75]. However, a new class of magnetic divertor configurations have been proposed, the design of which has been guided by the underlying physics principles of plasma detachment in standard divertors. Alternative divertor configurations, the so-called "advanced" divertors, are designed to minimize heat flux to the targets and improve detachment stability by introducing geometric variations in the magnetic field topology with characteristics that are thought to be favorable to stable detachment conditions. To do this, one common feature to many of these alternative divertor configurations is to manipulate the magnetic geometry of the plasma to poloidally extend the

outer leg of the separatrix, such that the plasma-material interface at the outer target is far removed from the main plasma [76]. This long leg allows for a longer connection length, increased divertor volume, and, in some cases, larger wetted target area relative to standard divertor configurations.

Long legs are features of several proposed alternative divertor designs, shown in simulations of Super-X, XPTD, and others, and demonstrated in experiments, including the TCV tokamak, the KSTAR tokamak, and recent experiments in MAST-U [7, 23, 77, 78]. These results have shown promise in the long leg as a novel divertor improvement, and simulations suggest the existence of stable, fully detached solutions for a multitude long-leg configurations in reactor-relevant conditions, making the long divertor leg configuration an appealing candidate for exhaust systems in future fusion pilot plants [8, 79, 80]. However, although these results are encouraging, no validation of the existing analytical models describing the transition to detachment has been performed for these long leg regimes. It is not yet fully known if and how the physics of detachment in standard divertors translates to these long legs, nor is there a definitive understanding of the impact of the long leg on plasma and impurity transport, meaning that stability and long-term operational outcomes of these long leg regimes remains unclear.

In this work, the SOLPS4.3 code is used to assess the transition to the detached divertor regime in a long leg divertor configuration. We hold the total number of particles in the simulation space constant in the so-called "closed gas box" approximation of the tokamak divertor to assess the physics of the transition to detachment over a scan of increasing particle count. These simulations feature a deuterium plasma with a trace neon impurity, impinging on a tungsten target. Over the course of this scan, we find that the criteria for detachment in a local flux tube is similar to theory-based predictions and existing numerical simulations of "standard" divertor targets. We observe asymmetry between the up-down and in-out divertors, with favorable characteristics in the long outer legs that are largely driven by cross-field transport. These simulations show that the transition to detachment is largely similar to plasma detachment in standard divertors.

5.2 Background

5.2.1 Fundamental physics of divertor detachment

Fundamental physics of divertor detachment have been extensively analyzed and detailed in other works [74, 75]. However, it is useful to briefly elucidate a few aspects of the existing understanding of the fundamental physics of detachment to emphasize how this understanding translates to the new magnetic geometries shown in this work.

The divertor is the exhaust and fueling system for the tokamak; field lines divert the exhausted heat and particles away from the fragile core plasma and into targets designed to handle the extreme conditions induced by the plasma exhaust. Initially, the plasma ions will hit the target plates and neutralize back into neutrals, which will form a protective cushion of neutral gas that will mitigate some of the incoming heat flux to the divertor target by expending energy on ionizing these newly-formed neutrals. This process will continue, eventually becoming so effective that the plasma-neutral-plasma ionization "loop" will become the primary mechanism of dissipating heat in the divertor volume, and the divertor enters what can be characterized as the "high-recycling regime". An important characteristic of the high-recycling regime is that the plasma flux generated from the ionization of the newly-formed neutrals in the divertor volume greatly exceeds the plasma flux from the scrape-off layer (SOL) or the influx of particles from neutral puffing by several orders of magnitude. Under these conditions, the scrape-off layer plasma influx can be ignored, and the SOL and divertor region can be considered as a "self-organized dissipative closed plasma box" [74]. This means that effectively, the SOL/divertor region contains a fixed number of deuterium or hydrogen particles and impurity that is sustained by a fixed heat flux (Q_{SOL}) coming across the separatrix and into the divertor region. The plasma-neutral-plasma ionization cycle in the divertor volume sustains the upstream plasma since there is virtually no upstream plasma source under these conditions.

The detached divertor regime is a natural extension of the high-recycling regime, where the dissipative processes in the divertor volume become so effective that the plasma exhaust can be virtually extinguished before it hits the target. Three synergistic atomic processes work together to reduce and eliminate plasma flux to the target: impurity radiation (which works as an energy sink, but can contaminate or reduce performance of the core plasma), ionization of neutrals (which works as an energy sink, but a source of

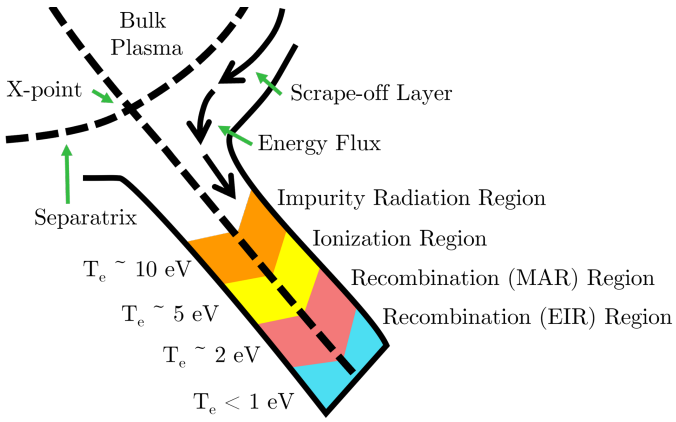

Figure 5.1. A cartoon imagining a simplified divertor. Each "region" is designated by a different color and characterized by a different temperature-dependent dissipative process: impurity radiation, neutral ionization, and plasma recombination (both molecule activated recombination, MAR, and electron-ion recombination, EIR).

plasma), and volumetric plasma recombination (which works as an extremely effective particle sink, but only "activates" at at single eV electron temperatures for molecular-activated recombination processes sub-eV electron temperatures for electron-ion three body recombination). Because these processes are largely dependent on temperature and each process is optimized at different temperatures, the divertor region can be imagined as a series of spatially stratified regions where heat flux is dissipated by different processes and temperature progressively reduced along the divertor leg before reaching the target, as in Figure 5.1. While ion-neutral friction is important for the momentum balance and cooling the divertor to sub-eV temperatures, it cannot alter the flux to the target. Instead, flux to the wall is characterized by the relation [20, 81]

$$\Gamma_t = \frac{Q_{SOL} - Q_{imp}}{E_{ion}} - \Gamma_{rec} \tag{5.1}$$

where Γ_t is the flux to the target and Γ_{rec} is the plasma sink from recombination. The plasma source from ionization is characterized by the first term, where Q_{SOL} is the incoming heat flux from the scrape-off layer, Q_{imp} is the heat loss related to impurity radiation, E_{ion} is the ionization energy needed per ionization event, which characterizes the plasma source as the total energy available for ionization with its corresponding energy "cost" [21].

This relation explains the behavior of the familiar "rollover curve", observed extensively in experiments and simulations, where detachment can be characterized as a "rollover" of the ion flux, or saturation current, to the material surfaces as a parameter related to the dissipation (e.g. density or particle count) is varied. Ion flux increases (as expected in the high recycling regime) then decreases, as the dissipative processes become effective enough to cool the divertor low enough to trigger volumetric plasma recombination processes, and the protective cloud of neutrals that forms at the divertor target will "detach" the plasma from its contact with the surface.

Fundamentally, Equation 5.1 describes the flux to the divertor targets as a function of the plasma source due to ionization and plasma sink due to recombination. However, this formulation neglects the effects of perpendicular transport, which might be important for long leg divertor configurations, as the increase in connection length and divertor volume in the long leg could significantly impact turbulence in the divertor leg. Simulations of the ADX conceptual tokamak (with a long-leg divertor design) using the UEDGE plasma edge modeling code showed that perpendicular transport to the side walls was significant for a steady-state detached plasma [79, 80], but the full scope of the impact of this substantial influence of perpendicular transport and side wall interaction on the edge plasma in the transition to detachment is unclear, and warrants further investigation. As such, Equation 5.1 should be modified for long leg divertor configurations to consider the effects of perpendicular transport, or

$$\Gamma_t = \frac{Q_{SOL} - Q_{imp} - Q_{\perp}}{E_{ion}} - \Gamma_{rec}, \tag{5.2}$$

where $Q_{\perp}$ refers to the heat lost due to perpendicular transport onto the main chamber and divertor walls in the main chamber and divertor. We distinguish this perpendicular heat flux leaving the plasma along the separatrix with $Q_{\perp}$, while the heat load to the target will be denoted later with Q_{target}.

5.2.2 Detachment onset criterion

Rollover of the ion saturation current can be indicative of detachment, but does not necessarily tell the full story; it is possible that other mechanisms, such as particle losses to side walls [82–84] or variations in Langmuir probe measurements, might create an artificial impression of the detachment of a plasma

when the actual physical mechanisms of true plasma detachment are not actually engaged. Similarly, the "Degree of Detachment" parameter [85], which relies on measurements of the saturation current, could face similar issues with interpretation of the characterization of plasma detachment.

As such, it is useful to articulate a physics-based scaling relation for the local onset of detachment to appropriately characterize the detachment state of a particular plasma and to make meaningful comparisons between different machines and operating conditions. Such a parameter was identified [9] and confirmed in a DIII-D-like plasma with simulations [86] as the ratio of the upstream pressure P_{up} to the specific heat flux entering the recycling region $q_{recycle}$ in a single flux tube, or $P_{up}/q_{recycle}$, which indicates detachment when it meets and exceeds some critical value (approximately 20 N/MW for deuterium plasmas). This is because maintaining that upstream plasma pressure requires some energy flux above the critical level to sustain the recycling, and therefore provide the sufficient inventory of neutrals to maintain the stability of radiation, ionization, and recombination processes in the divertor plasma.

5.3 Methods

5.3.1 SOLPS4.3

To assess the physics of detachment in a long leg divertor configuration, a scan of simulations was performed with the SOLPS4.3 code [35, 45]. The SOLPS4.3 code is a suite of plasma transport codes, composed of the 2D multifluid B2 code to solve the plasma state along and across magnetic flux surfaces coupled with the 3D multi-species Monte Carlo EIRENE code to solve the state of the neutral particles. Here, the behavior of electrons and ions (deuterium and all charge states of neon) are calculated with the B2 fluid code and used as the background plasma for EIRENE calculations of the trajectory of the neutrals (deuterium and neon). The B2 code solves transport equations for electrons and ions, including continuity, momentum, and energy balance equations in the magnetic configuration of a tokamak. Equations solved in B2 are derived from a modified set of the Braginskii equations, where transport along field lines is assumed to be classical, but includes some ad hoc processes (such as anomalous or turbulence-driven transport coefficients) that allow for cross-field transport. The EIRENE code calculates individual trajectories of neutral particles, and includes atomic processes, such as ionization, charge exchange, elastic collisions, and recombination. Molecule-activated recombination processes (MAR) are not included since the MAR

process is not expected to contribute significantly to effective recombination of the divertor plasma for high power and high density cases [87], but electron-ion recombination (EIR) processes are included. Drifts were not included in these simulations, as they are not included in the SOLPS4.3 code package.

It is important to note that drifts have been shown to have a profound impact on plasma detachment in simulations in multiple plasma edge codes [88, 89], where the dynamics of the plasma (and resultant neutral dynamics in response to changes in the plasma behavior) are shown to be strongly influenced by the presence of drifts. However, it was observed that the presence of drifts had little impact on the steady-state solutions of SOLPS-ITER simulations with disconnected double-null geometries with and without drifts, while similar simulations in connected double-null and single-null geometries showed significant differences between comparative simulations with and without drifts [90]. All simulations presented in this work feature a computational grid with a disconnected double-null configuration, and up-down asymmetries in plasma parameters that are sometimes ascribed to the presence of drifts are evident in the simulation results. While the lack of a model for drifts in the SOLPS4.3 code package prohibits the study of the impact of drifts on these simulations in the first place, it is reasonable that the more physically realistic geometry of the disconnected double-null (and corresponding increased complexity of the computational domain) might mitigate the impact of drifts on the qualitative nature of the steady-state of the simulations presented in this work.

5.3.2 Setup

The computational grid features a disconnected double null configuration with a long, tightly baffled outer divertor leg with a tilted target at the outer divertors (both upper and lower) and short, tightly baffled inner divertor legs, shown in Figure 5.2. Unlike a symmetric double null configuration, where the two X-points lie on the same flux surface and are connected by one separatrix, the disconnected double null reflects a more realistic consideration where there is no exact magnetic connection between the upper and lower divertor X-points [91]. In this situation, there is a primary X-point on the last-closed flux surface, with a secondary X-point on another magnetic flux surface just outside the LCFS [92]. The divertor with both primary and secondary separatrices will receive incoming fluxes from both the separatrices, while the other divertor will only receive fluxes from the secondary separatrix, which results in an imbalance in the overall magnitude of the integrated fluxes directed towards each divertor. In these simulations, the

primary X-point in the disconnected double null configuration is in the lower divertor. As such, to avoid a loss of generality in this work, the lower divertor will be denoted as the "primary" divertor and the upper divertor will be denoted as the "secondary" divertor, referring to the intersection of the principal separatrix with each target plate. This nomenclature used for identification of each divertor is shown in Figure 5.2.

These simulations are performed with a total of 30 MW input power, carried evenly between ions and electrons, and fixed across all simulations. Cross-field transport coefficients are constant and set at $\chi_\perp = 1.0\ m^2 s^{-1}$ and $D_\perp = 0.3\ m^2 s^{-1}$, which were chosen to emulate a plasma regime with strong turbulence and no edge transport barrier in a compact ($R_0 = 1.85\ m$), high-field (12.2 T) tokamak with high input power [93], resulting in a heat flux width $\lambda_q = 0.2\ mm$. Unlike the SOLPS-ITER simulations presented in that reference, the SOLPS4.3 code package does not have the capability to incorporate spatially varying transport coefficients, so these transport coefficients are consistent with the ones used outside of the imposed transport barrier that is present in the simulations shown in that work (the transport coefficients listed in that article only describe the near-SOL transport barrier values). They are also equivalent to a 0-D estimate that is consistent with the projected separatrix temperature listed in that reference.

The scrape-off layer width (from the separatrix to the edge of the plasma domain) is 5 mm, and the distance between the primary and secondary separatrices is 2 mm. At the midplane, there is a 7 mm gap between the primary separatrix and the vessel wall; the SOLPS code only simulates neutrals, not plasma, all the way to the vessel wall, but the rather wide scrape-off layer width included in the plasma simulation domain covers most of this gap, and the divertor side walls in the vessel geometry are close to the plasma simulation domain in the divertor legs. As such, all fluxes out of the north and south boundaries (with boundary conditions of a 3 cm radial decay length for temperature and density) are assumed as losses to the walls.

Boundary conditions were selected to achieve a "closed box" setup to emulate the high-recycling regime, where the total number of deuterium particles is held constant in a simulation as the simulation is run to steady state. The next simulation in the scan is generated by replicating the steady-state simulation, holding all input parameters constant, incrementally modifying the total number of particles in the edge of

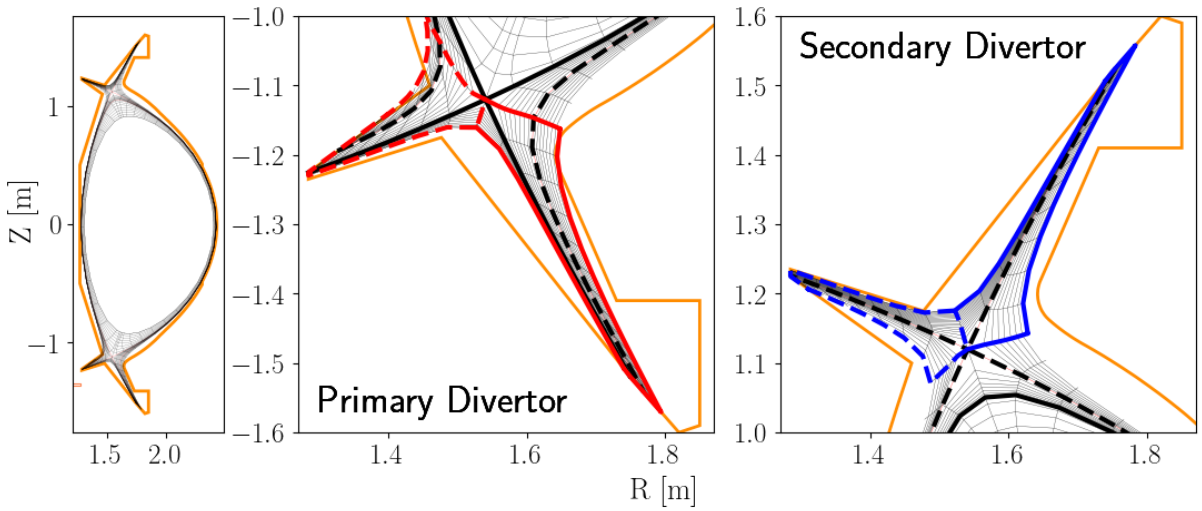

Figure 5.2. (a) The computational mesh used for the B2 component of the simulations. The EIRENE computational mesh, which extends to the outer walls (orange), is not shown. (b) The primary divertor has a short inner leg (outlined in dashed red) and long outer leg (solid red). The primary separatrix is drawn as a dark black line, and the secondary separatrix is drawn as a dashed black line. (c) The secondary divertor also has a short inner leg (dashed blue) and a long outer leg (solid blue). The vessel wall is drawn in orange on each figure; the overlap of the vessel wall and the simulation grid on the inner primary divertor is a consequence of a limitation of the parameterization used by the plotting software to create a closed shape with no overlapping lines, and does not reflect the real geometry of the vessel at that point (which actually sits just outside the plasma simulation grid).

the existing steady-state simulation (denoted in this work as N_D^{edge}), and running the new simulation to steady-state. This process is repeated to generate a bank of steady-state simulations, each with a slightly different and gradually increased inventory of deuterium particles, that can be analyzed as individual "snapshots" that collectively emulate the transition to detachment. This approach, in contrast to the more common methodology of varying upstream density at the core-edge interface to generate a parameter scan, allows for a more natural evolution of plasma parameters and their response to varying input conditions that is more likely to capture behavior (like hysteresis or bifurcations) that might be obscured or otherwise not captured by modulating the upstream settings [75]. We note that using the total number of particles as the control parameter of the simulation is not repeatable in experiments; we emphasize that these studies are intended as a framework for rigorous theoretical analysis and a thorough examination of the physics of plasma detachment and are not intended to be replicated on any real tokamak machine.

To achieve the "closed box" configuration, recycling is set to 100% at the targets and walls, where all ions impacting the material surfaces and boundaries are reflected as neutral particles. There is no active puff or pump included in these simulations, but particle count of both species is maintained using a feedback system implemented in the SOLPS4.3 code package that controls an effective particle puff that is sourced at all material surfaces on the outboard side and the core to make up for inherent and unavoidable particle losses which result from numerical coupling between the implicit fluid and explicit kinetic codes. The neon impurity is fully contained in this simulation, meaning an initial inventory of particles was included in the simulation with no sink or source of neon particles. The Bohm sheath condition is applied at the target, and a zero-flux boundary condition is applied at the core.

5.4 Results and Discussion

5.4.1 Up-Down asymmetries

In these simulations, there are pronounced differences in the primary and secondary divertor heat fluxes, which are consistent with observations of up-down asymmetries in "standard" divertor configurations. Asymmetries are characterized as imbalances of the heat and particle loads between the different divertor regions (upper and lower divertors, in the case of a double null, or inner and outer, for each divertor). These asymmetries are frequently observed in experiments and simulations, and can arise from

the ballooning nature of anomalous transport, drift effects, impurity radiation, geometric effects, or as a result of other instabilities [40, 74]. Such asymmetries are observed in these simulations: the primary and secondary divertors display vastly different characteristics, and the inner and outer divertors in each of the primary and secondary divertors also display significant asymmetries (which will be identified and discussed in later sections). Figure 5.3 shows the distribution of the heat flux entering into each of the four divertor legs, which reflect the asymmetry in fluxes directed towards each of the divertors.

The primary cause of these up-down asymmetries are the transport mechanisms associated with the disconnected double null magnetic topology, since other up-down symmetry-breaking effects, such as the influence of drifts or impurity radiation, are not applicable here, as these simulations do not include drift effects and include only trace impurity radiation. This effect, which is well-understood and observed in "standard" disconnected double null divertors, also manifests in the long leg geometry; the disconnected double null configuration of these simulation grids feature the primary X-point (and therefore the primary divertor) at the lower part of the device. In this magnetic configuration, there are two separatrices in the lower divertor, and rapid longitudinal transport along or very close to these separatrices amounts to a total flux that is much greater than the flux to the secondary divertor [91].

5.4.2 Plasma detachment

The strong disbalance in heat fluxes induced by the asymmetric magnetic topology causes plasma detachment to proceed with different dynamics in each of the upper and lower divertors. The results of a simulation set with incrementally increasing particle content N_D^{edge} shows a rollover of plasma flux to the divertor targets, shown in Figure 5.4. Across the simulation set, both the inner and outer secondary divertors detach first and second, respectively, as particle count is increased. The outer primary divertor detaches third, and the inner primary divertor never detaches.

Despite very different plasma conditions in each of the individual divertor legs (which are detailed in subsequent sections) the rollover of the plasma flux to the target starts at (or never surpasses) the same $P_{up}/q_{recycle}$ value of 20 N/MW, shown in Figure 5.5, which is consistent with existing theory and understanding of divertor physics. To calculate the $P_{up}/q_{recycle}$ ratio, the procedure detailed in [86] is followed. A simulation with a strongly attached plasma in all four divertors is identified from Figure 5.4,

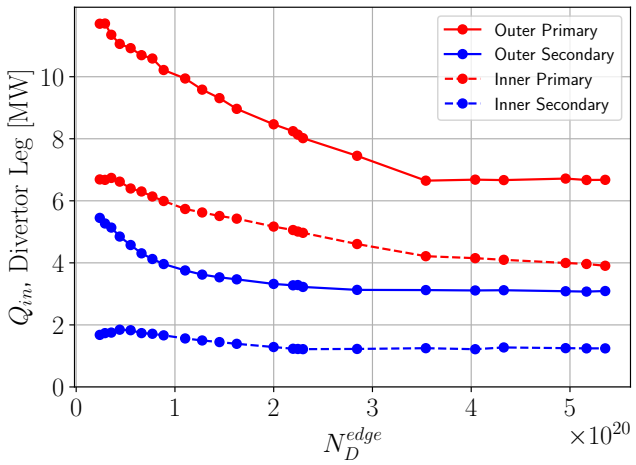

Figure 5.3. Net heat flux crossing the divertor throat to enter each of the four divertor legs. Each divertor is shown using the same color convention and line style shown in Figure 5.2; the outer divertors are shown with solid lines, and the inner divertors are shown with dashed lines, and the primary divertors are drawn in red, while the secondary divertors are drawn in blue.

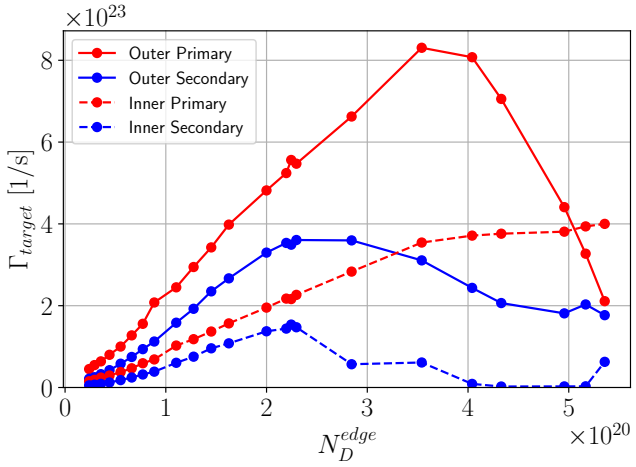

Figure 5.4. Ion flux to each of the divertor targets. The outer divertors are shown with solid lines, and the inner divertors are shown with dashed lines. The primary divertors are drawn in red, while the secondary divertors are drawn in blue.

and the most loaded flux tube on each target plate in this simulation is determined. The four different flux tubes that are identified are unique to each of the four divertors. Each of these four flux tubes is then analyzed across the entire simulation set to see how the plasma parameters evolve in the same flux tube to obtain the different profiles for each of the divertors. The upstream pressure, P_{up}, is the plasma pressure in each flux tube at the midplane. The $q_{recycle}$ value is determined by taking the specific heat flux entering the recycling region, where the recycling region is defined as the region where 85% of the total ionizations in that flux tube are taking place. This is calculated by taking the integral of the total number of ionizations in the flux tube from the target up to the heat flux stagnation point, and then identifying the cell where the integral of the ionization events becomes $\geq 85\%$ of the total ionizations. The parallel heat flux entering the cell where this region begins, which can be interpreted as the input energy to facilitate the recycling process that maintains the upstream plasma, is $q_{recycle}$.

Figure 5.5 shows the dependence of the saturation current to the target on the $P_{up}/q_{recycle}$ ratio for all simulations in the particle count scan preceding the ion flux rollover observed in Figure 5.4 in each divertor. All simulation results are included for the primary inner divertor, which never displays a rollover in target ion flux; notably, the $P_{up}/q_{recycle}$ ratio approaches, but never exceeds the "critical" value of 20 N/MW predicted for plasma detachment. The outer secondary divertor rolls over with $P_{up}/q_{recycle}$ value of roughly 28 N/MW, which is higher than the other divertors and visible as the peak on the solid blue line in Figure 5.5. This is not abnormal, since the physics basis for this ratio assumes a set of simplifying assumptions and minor variations in adherence to this parameter, similar to this one, have been observed in other simulation sets [86, 94]. In this case, the $P_{up}/q_{recycle}$ value is likely higher than the prediction since most of the fluxes are directed towards the primary divertor, and these strong up-down asymmetries mean the effects of the primary divertor dominate, so heat flux to the outer secondary divertor is lower and the stagnation of the upstream pressure on the outboard side does not occur until the primary outer target detaches (shown in Figure 5.6).

We also notice a modest decrease in the average deuterium ionization cost, consistent with observations in other works [95, 96]. This effect is shown in Figure 5.7, where the averaged electron energy dissipation per ionization of each deuterium atom (accounting for both the potential energy required to ionize the neutral atom and the radiative energy losses from excitation collisions before the ionization,

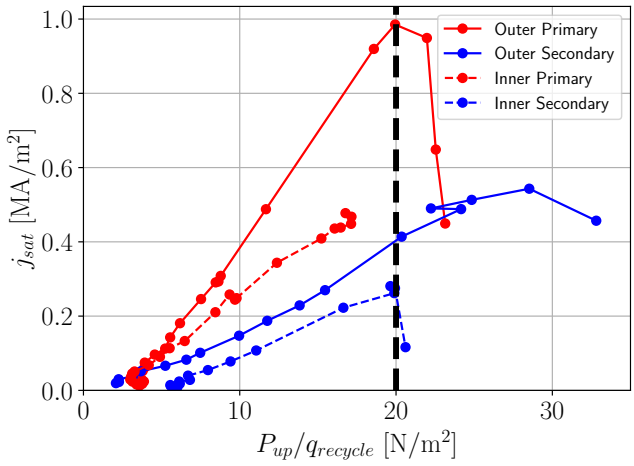

Figure 5.5. Dependence of the saturation current j_{sat} on the $P_{up}/q_{recycle}$ ratio across all simulations for the flux tube corresponding to the most loaded flux tube in a highly attached simulation in each divertor. Each divertor is shown using the same color convention and line style shown in Figure 5.2.

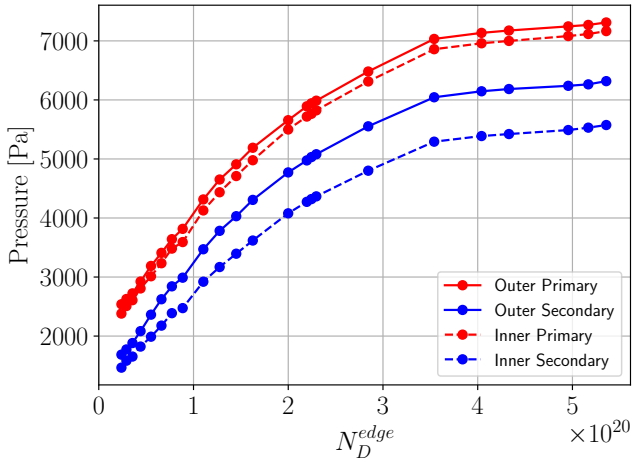

Figure 5.6. Dependence of plasma pressure at the midplane on N_D^{edge} for each of the flux tubes.

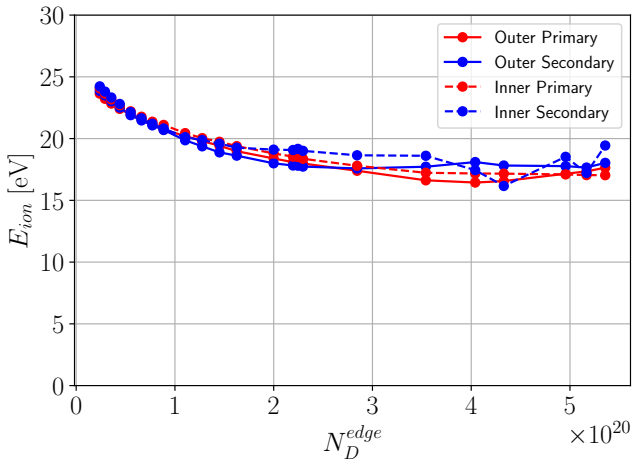

Figure 5.7. Average energy cost per ionization in each of the divertor regions across the simulation set.

divided by the total number of ionizations) is shown. The average energy per ionization is dependent on density and temperature, and significant changes in this value might have an impact on the overall energy balance as the plasma transitions to the detached regime. The small variation in the ionization energy cost does not play a significant role in the energy balance in the transition to plasma detachment shown in these simulation results.

5.4.3 In-out asymmetry

In each of the primary and secondary divertors, there is significant poloidal asymmetry between the inner and outer legs. The secondary divertor, which is positioned at the top of the device and receives lower heat and particle fluxes relative to the primary divertor at the bottom, shows lower heat and particle fluxes to the secondary inner divertor and lower temperatures than the secondary outer divertor across the whole simulation set. The plasma at the secondary inner divertor shows the "roll over" of the saturation current to the target and detaches first, at lower number of particles N_D^{edge}, than the secondary outer divertor. The blue lines in Figure 5.8(a), Figure 5.8(b), and Figure 5.8(c) show the peak heat flux, the target electron temperature just outside the separatrix, and the total heat load, respectively, for the secondary inner (dashed blue) and secondary outer (solid blue) divertors. The peak heat flux and total heat load to the secondary outer target are consistently higher than the secondary inner target, while the electron temperature at the secondary inner target decreases to volumetric recombination temperatures before the

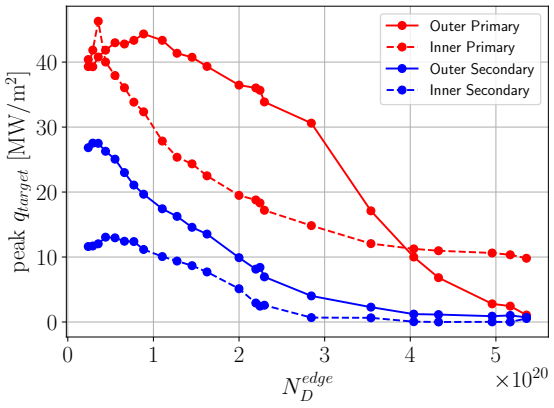

(a) Peak heat flux to the target.

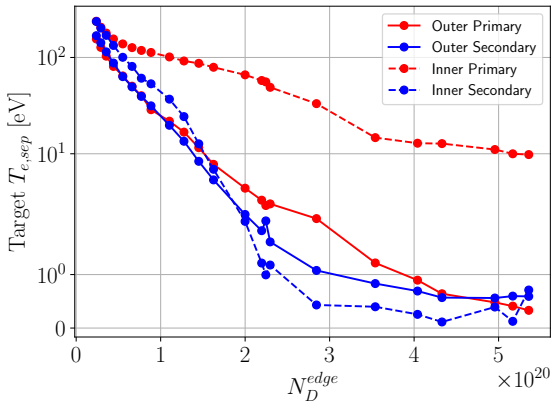

(b) Electron temperature at the target, just outside the separatrix.

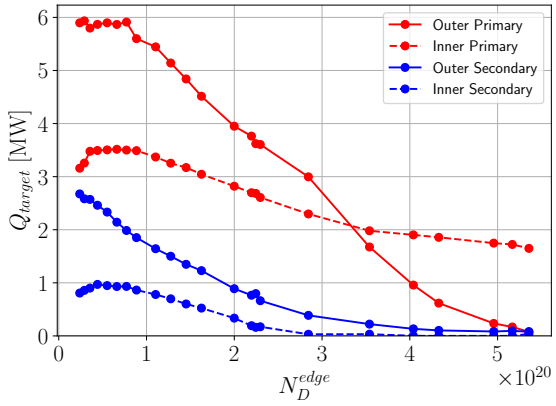

(c) Total heat load to the target.

Figure 5.8. Distribution of target parameters for each divertor.

secondary outer target does. Volumetric recombination increases first at the secondary inner target, shown in Figure 5.9, which is consistent with the rollover of ion flux observed in Figure 5.4. This distribution of in-out symmetry, where the inner divertor detaches before the outer one, is common and expected in "standard" divertor configurations, as higher fluxes are expected at the outboard side due to ballooning effects [74].

However, the opposite asymmetric effect occurs for the primary divertor; while there is still significant asymmetry in the heat and particle fluxes between both the primary divertor legs, the long legged primary outer divertor "rolls over" and detaches first, while the ion flux to the short primary inner divertor reaches a level of saturation and the plasma stays attached. The red lines across the quantities shown in Figure 5.8

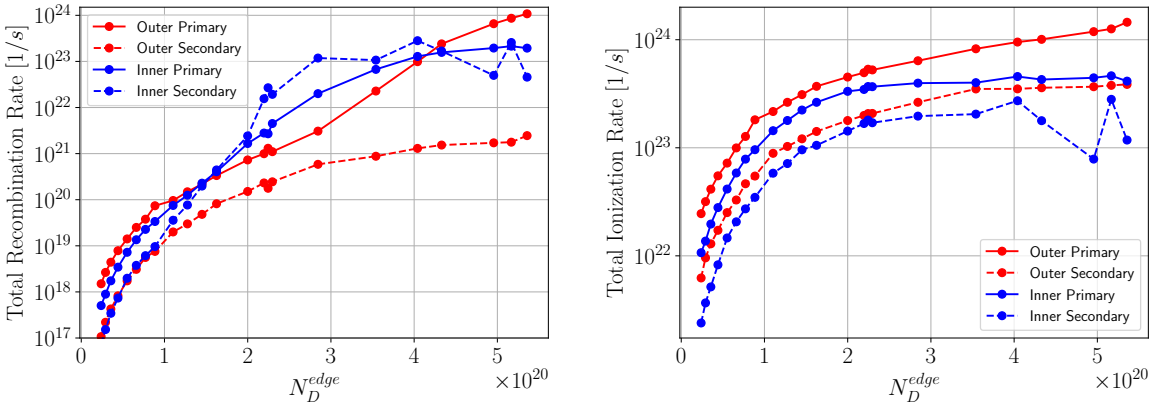

(a) Total recombination events in each divertor.

(b) Total ionization events in each divertor.

Figure 5.9. Atomic processes in each divertor.

show a cooler outer divertor and lower heat fluxes (red solid line) at high densities relative to the inner divertor (red dashed line).

This "opposite" asymmetric effect appears to be a unique feature of the long leg in the primary divertor, which has a larger power load than the secondary divertor. Experiments and modeling of lower single null L-mode deuterium plasmas with a short inner leg and long outer leg on the KSTAR tokamak also achieve plasma detachment in the long outer leg before the short inner leg [97]. Analogous results from similar experimental setups were also observed on the TCV tokamak, but these discharges used reverse B_T and featured a much longer connection length in the outer leg relative to the KSTAR results or the simulations presented here [98, 99]. In the KSTAR experiments and simulations, the magnetic geometry of the KSTAR tokamak features a lower single null divertor with an open, vertical inner target with a short poloidal connection length and a much longer outer leg onto an open, inclined target plate. The TCV geometry is similar to the KSTAR geometry, but with a highly-flared leg on a flat outer target. The simulations presented in this work feature a similar short inner leg and longer outer leg in the lower divertor, but include tight baffling along each of the divertor leg channels, unlike the open target plates used in the KSTAR or TCV tokamaks. The KSTAR study attributes this asymmetry to target geometry, while the TCV study concludes that the asymmetry is a consequence of flux flaring effects at the target.

While the specifics of target geometry might play a role in enhancing the detachment of the long

leg, it is not clear that this is the dominant mechanism driving this significant asymmetry, since the same effect is observed in only one of the divertors in this simulation set for a geometric configuration with matching angled, closed divertors with long outer legs in the upper and lower divertor regions. In these simulations, the secondary divertor targets are also angled with closed geometries and a long outer leg, but detachment proceeds with the inner before the outer divertor in the particle count scan, consistent with detachment in standard divertor configurations, but opposite to that of other long leg discharges. This is likely due to both the tight baffling of the narrow divertor leg channel, in contrast to the open divertors at the inner target in the KSTAR and TCV tokamaks, and the lower power entering the secondary inner leg. The tight channel in the inner divertor facilitates neutral trapping and promotes detachment at the inner target. A similar effect (although less pronounced than shown in these simulations, and only after the detachment of the outer target) was observed on TCV, where modular baffles were installed at the inner target to create a more closed inner divertor region and enabled detachment at the inner target [100].

However, while the primary divertor also features tight baffling at the short inner leg that would enhance neutral confinement, the plasma in the primary inner divertor never detaches from the target in this simulation set. This seems to be related to the magnitude of the heat fluxes directed towards each divertor; due to up-down asymmetry effects, more heat flux is directed to the primary divertor target, and any improvement in neutral confinement due to this tight slot geometry is mitigated by the shorter connection length and smaller overall divertor volume that do not appear to have the capacity to dissipate the incoming power. The decomposition of the heat flux into major sources/sinks and identification of spatial characteristics of each divertor leg in the simulation with the maximum particle flux to the outer divertor leg is summarized in Table 5.1. The relevant quantities relating to the energy available for ionization in Equation 5.2 are shown, where Q_{in} is the component of Q_{SOL} that is directed towards each divertor leg (from Figure 5.3), $Q_{\perp}$ is the perpendicular losses to the side walls (from Figure 5.11), and Q_{ion} is the total energy available for ionization (from Figure 5.7 and Figure 5.9(b)), such that the energy hitting the target Q_{target} (from Figure 5.8(c)) is:

$$Q_{target} = Q_{in} - Q_{\perp} - Q_{ion}. \tag{5.3}$$

Table 5.1. Decomposition of incoming heat flux into heat sinks in each divertor leg just before plasma flux rollover in the outer primary divertor (N_D^{edge} = 3.54e20), with the total volume and surface area of the walls in each leg. Q_{in} is the heat flux crossing the divertor throat and entering into each leg. $Q_{\perp}$ is the heat flux crossing the north and south boundaries of the computational domain for each divertor region. Q_{ion} is the energy loss from plasma ionization. Q_{target} is the total heat load to the target. The divertor volume and surface area in each leg are included.

Leg	Q_{in}	$Q_{\perp}$	Q_{ion}	Q_{target}	Volume	Wall Area
Outer Primary	6.6 MW	2.3 MW	2.6 MW	1.7 MW	0.19 m^3	8.92 m^2
Inner Primary	4.2 MW	0.8 MW	1.0 MW	2.0 MW	0.13 m^3	3.81 m^2
Outer Secondary	3.1 MW	1.6 MW	1.4 MW	0.2 MW	0.16 m^3	8.88 m^2
Inner Secondary	1.2 MW	0.6 MW	0.6 MW	0.0 MW	0.09 m^3	4.25 m^2

The volume and surface area for each divertor leg are also included.

As in the KSTAR and TCV tokamaks, the outer target in the primary divertor *does* detach, while the inner one remains attached. The magnitude of the heat flux received by the outer divertors is consistently larger relative to the inner ones, as shown in Figure 5.3, but the outer divertor volume itself is also much larger than the inner one, shown in Table 5.1. This equates to a larger space for a higher particle inventory for more dissipative processes to occur, but it also increases the surface area of the divertor walls. The cumulative perpendicular heat loss to the divertor side wall, $Q_{\perp}$, is a significant energy sink in the power balance in the outer leg. While the baffled, angled target of the various long leg divertor configurations likely enhances the detachment of the plasma, as mentioned previously, it cannot explain the mismatch in the observations of the detachment in the primary and secondary divertors observed in these simulations. Instead, the energy balance indicates that it is likely that the dominant mechanism behind the strong in-out asymmetry in detachment is the influence of perpendicular transport.

5.4.4 Perpendicular transport

5.4.4.1 Divertor heat flux

The effects of perpendicular transport appear to be extremely important in the transition to detachment in the long leg in several ways. To help clarify the following discussion, a schematic of the outer divertor leg and associated heat fluxes and sinks is shown in Figure 5.10. As described in the previous section, a significant portion of the divertor heat flux is directed out of the plasma and onto the material surfaces

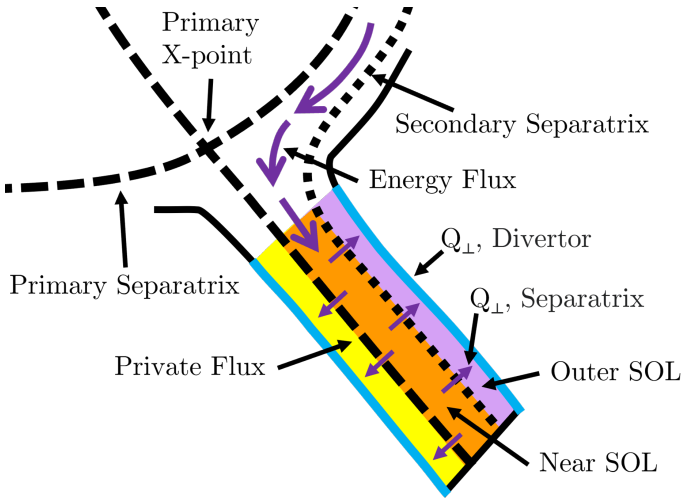

Figure 5.10. A cartoon illustrating various regions, defined by their proximity to the two magnetic separatrices, in the outer divertor and associated heat fluxes. The private flux region is shown in yellow, the near SOL is shown in orange, and the outer SOL is shown in light purple. Heat flux is shown in dark purple; the majority of heat flux enters the divertor throat in the near SOL (where the shading for the zones begins). The perpendicular heat flux, $Q_\perp$, Separatrix, is shown in the small purple arrows, orthogonal to the separatrices and directed away from the near SOL. The divertor side wall, which receives a significant heat flux, is identified with the light blue lines as $Q_\perp$, Divertor.

on the tightly baffled divertor leg, acting as an additional energy sink identified in Equation 5.2 and represented as the blue surfaces in Figure 5.10. These losses are displayed in Figure 5.11 and identified in Table 5.1.

The perpendicular transport enhances heat flux spreading and delocalization in the outer divertor leg. The total cross-field heat transport directed across the separatrix, illustrated as the small purple arrows in Figure 5.10, is shown in Figure 5.12. The heat flux entering the private flux region from the SOL is shown in Figure 5.12(a), while the heat flux passing through the near SOL and entering the outer SOL is shown in Figure 5.12(b). The majority of the heat flux directed into each primary divertor region is carried by the primary separatrix, and passes through the near SOL region (the orange-shaded channel in Figure 5.10), flanked by the primary and secondary separatrix legs. The heat flux passing into the near SOL in each primary divertor leg is shown in Figure 5.13, while the total heat flux entering the divertor legs is shown in Figure 5.3; roughly three quarters of the total power to each leg travels into this region, so this region

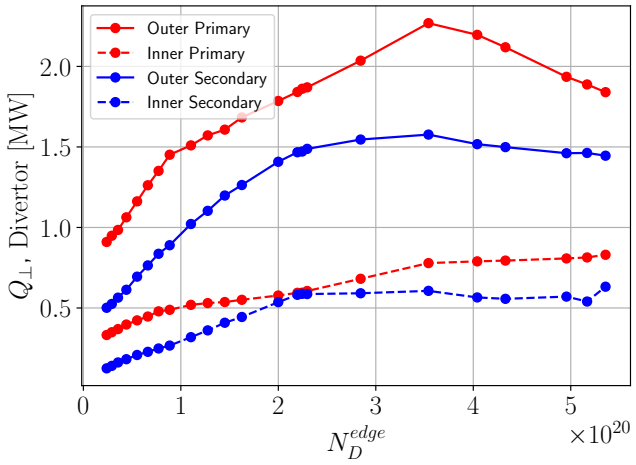

Figure 5.11. Total $Q_\perp$ to the divertor walls in each leg.

will be the focus of this analysis. Across the particle count scan, roughly 1 MW of the incoming heat flux to this near SOL region is consistently transported across the separatrix into the private flux region (the yellow-shaded channel in Figure 5.10), providing a strong reduction in the heat flux directed towards the near SOL divertor target. In comparison, the cross-field transport across the separatrix to the private flux region of the inner leg is much weaker relative to the outer leg; the near SOL in the inner divertor consistently receives a portion of incoming heat flux equivalent to approximately 75% of the power to the near SOL in the outer leg, but only loses an equivalent of approximately 50% of the power lost to the PFR from cross-field transport in the outer leg.

At the secondary separatrix in the primary divertor, there is significant asymmetry in the cross-field transport crossing from the near SOL to the outer SOL. At very low densities, there is essentially no transport across the separatrix (there is even a small flux in the reverse direction, back towards the near SOL, at the lowest densities in the outer divertor). However, as the particle count increases and the secondary divertors detach, the cross-field transport towards the outer SOL in the outer divertor increases significantly, and continues to rise as the outer primary divertor detaches. The inner primary divertor cross-field transport to the outer SOL remains very low and never increases.

The spread of the overall heat load in the near SOL helps to reduce power density to a tolerable level where either the cross-field transport can continue to carry the heat flux to the side walls of the leg, or the

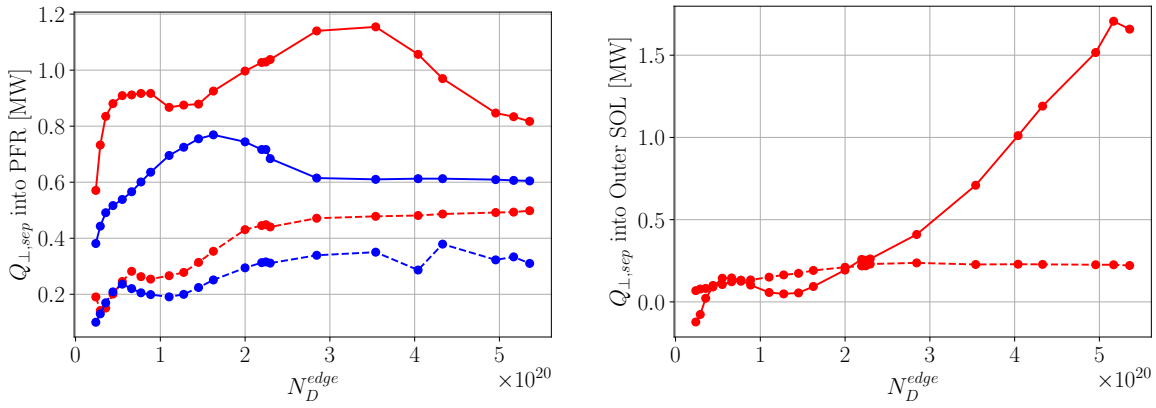

(a) Total heat flux crossing the main separatrix leg in each divertor, towards the private flux region.

(b) Total heat flux crossing the separatrix leg across the secondary divertor leg in the primary divertor, leaving the near scrape off layer and directed towards the outer scrape-off layer.

Figure 5.12. Heat flux crossing the separatrix into the PFR (for all divertors) and into the outer SOL (for the primary divertors).

dissipative processes can deplete the remainder of the heat flux before the plasma starts to recombine. In contrast, the heat flux to the inner target remains fairly localized at the primary separatrix, which seems to prevent detachment altogether.

To assess whether perpendicular transport plays a significant role in the energy balance in the divertor heat flux spreading in the detached plasma, additional simulations were generated with transport coefficients reduced by one third to $\chi_\perp = 0.33\ m^2 s^{-1}$ and $D_\perp = 0.1\ m^2 s^{-1}$. A comparison between the electron temperatures in the primary divertor for the simulation at the highest N_D^{edge} value with the "original" (a) and "reduced" (b) transport coefficients is shown in Figure 5.14, dramatic increase in temperature all along the separatrix and to the target that is incompatible with the detachment processes described earlier in the paper. In this simulation, which displays the "most" detached outer leg with the original transport coefficients, the perpendicular heat flux interacting with the main chamber side walls reduces from around 16 MW to 7.6 MW, greatly increasing the heat flux received by each of the divertor legs, and the plasma fully reattaches at the primary outer leg with modified transport coefficients. As shown in the Figure 5.14(b), the simulation with the modified perpendicular transport coefficients has considerably higher electron temperatures all the way down the leg to the target in both the near SOL and outer SOL than shown in the original simulation. In the primary outer leg, the heat flux entering

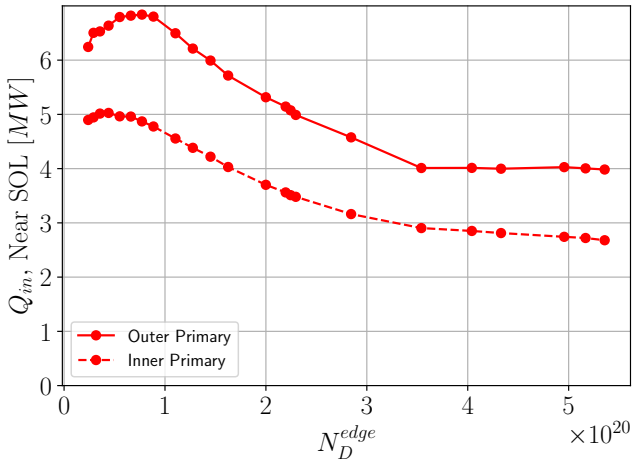

Figure 5.13. Total heat flux entering the near-SOL region, outside the primary separatrix and within the secondary separatrix, in the primary divertor.

into the divertor leg increases from 6.7 MW to 10.4 MW, the perpendicular heat flux to the divertor side wall $Q_\perp$ is reduced from 1.9 MW to just under 1 MW, and heat flux to the primary outer target increases from virtually nothing to 2 MW. Similarly, the secondary outer divertor (not shown in the figure) also reattaches, despite receiving considerably less heat flux than the primary divertor; the heat flux entering the secondary outer divertor leg increases from 3.1 MW to 3.7 MW and the $Q_\perp$ to the secondary divertor side walls reduces from 1.5 MW to 0.8 MW, while the heat flux to the secondary outer target increases from virtually nothing to 0.8 MW.

5.4.4.2 Main chamber heat flux

While detachment processes proceed "as expected" with similar behavior and scaling criteria to standard divertors, perpendicular transport also plays a significant role in the reduction of heat fluxes entering each divertor leg, which ultimately lowers the incoming power in the legs to a tolerable level for the "standard" dissipative processes to become effective and the "expected" detachment behaviors to proceed. There are significant perpendicular losses to the side walls as particle count increases, shown in Figure 5.15, which eventually saturate and stop increasing with higher densities.

At low plasma densities, power exhaust from the core enters the scrape-off layer and travels straight to the divertor legs. As the particle count is increased, the heat flux leaving the plasma and impacting

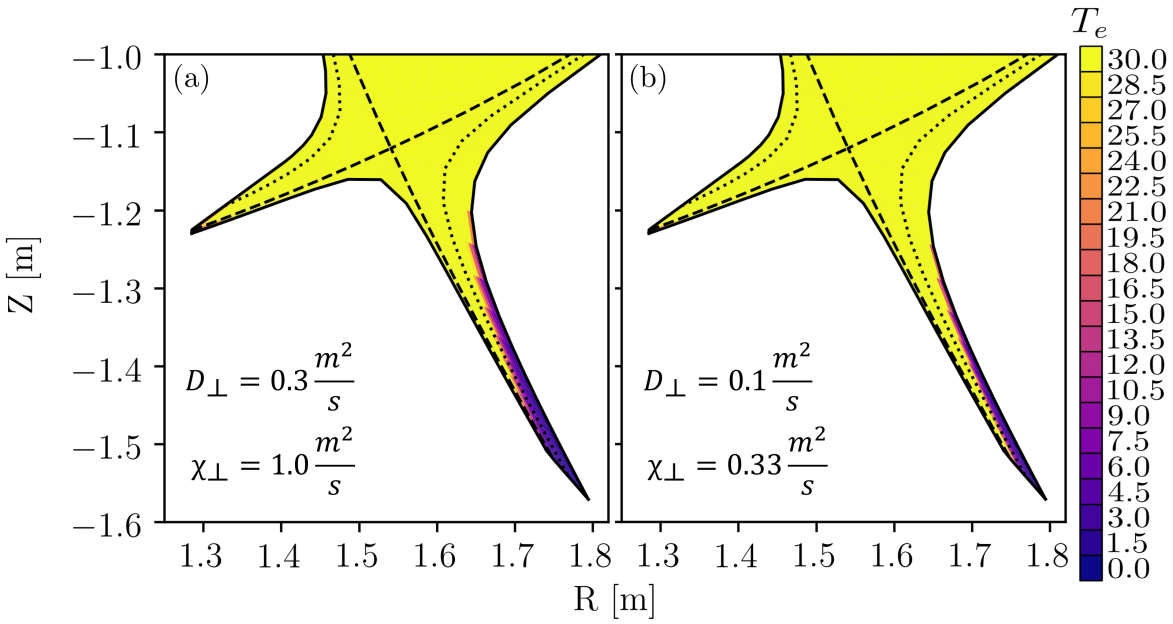

Figure 5.14. Distribution of electron temperature in the primary divertor for the simulation corresponding to the the highest particle inventory of N_D^{edge}=5.36e20. The simulation with "unmodified" transport coefficients, with a detached plasma, is shown in (a), while the simulation with reduced transport coefficients, with an attached plasma, is shown in (b).

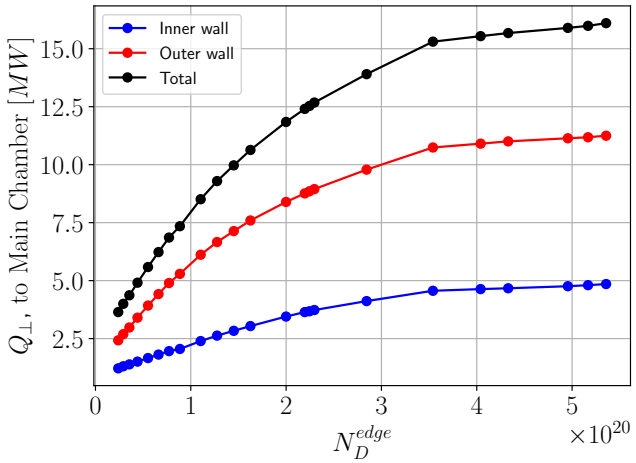

Figure 5.15. Losses resulting from perpendicular transport to the inboard (blue) and outboard (red) side walls in the main chamber. Total losses are shown in black.

the main chamber walls increases, observed in Equation 5.2, and the remaining heat flux that enters the divertor legs decreases, observed in Equation 5.1. This effect occurs until the outer divertor reaches its peak in the ion flux rollover curve, at which point the synergistic effect of losses to the side walls and ionizations in the divertor volume reduce the temperature in the divertor. At this low temperature, volumetric recombination processes begin in the outer leg, and upstream pressure saturates. A significant increase in volumetric recombination processes in the primary outer divertor, shown in Figure 5.9(a), with a saturation of the total ionization events in the primary outer divertor, shown in Figure 5.9(b), correspond to the upstream pressure saturation (Figure 5.6) and rollover at the outer target (Figure 5.4).

At this point, radial transport towards the main chamber walls and divertor legs stays fairly high, but stops increasing, while the heat flux to the outer primary divertor leg walls starts to decrease, shown in Figure 5.11.

This effect is the result of the upstream pressure saturation; density increases, temperature lowers, and as the pressure saturates, the radial gradient in the temperature relaxes, which nearly eliminates the conductive component of the cross-field heat fluxes, shown in Figure 5.16. There is strong variation in the radial temperature profile at lower number of particles N_D^{edge}, which flattens out after recombination processes begin in the outer leg. All versions of the SOLPS code use a diffusive ansatz for radial transport, which is an approximation of turbulence that emulates a spatiotemporal average of cross-field transport through spatial gradient with diffusion coefficients. This follows an equation of the form

$$Q_\perp = -\frac{5}{2} D \frac{\partial n}{\partial r} T_i - \chi \frac{\partial T_i}{\partial r} n, \tag{5.4}$$

where D and χ are the user-specified diffusion and thermal diffusivity coefficients that articulate the convective and conductive cross-field heat fluxes, respectively. The saturation of the upstream pressure and the relaxation of the temperature gradient mean that essentially the only contribution to the cross-field transport is the convective heat flux. This convective contribution is significant, which is typical and expected for edge plasmas, but does not increase with increasing particle count because of the saturation in pressure.

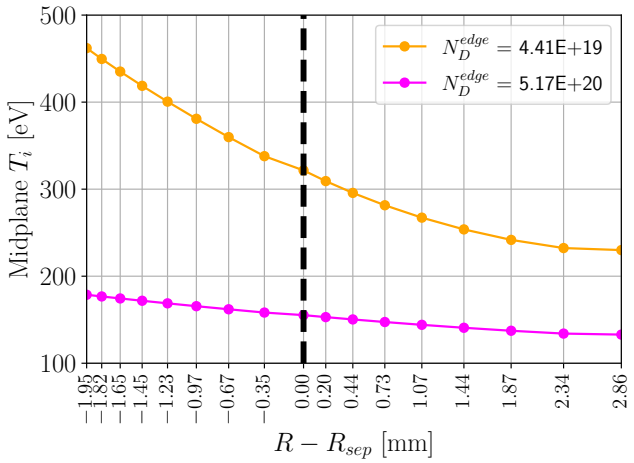

Figure 5.16. Midplane ion temperature for a lower particle count simulation and a higher particle count simulation.

The consequence of this is a synergistic beneficial effect of the flux rollover and transition to the detached state: as recombination begins, the conductive component of the cross-field transport is eliminated, limiting the cross-field transport to a fixed level and stabilizing conditions upstream.

5.4.5 Trace impurity radiation

A trace neon impurity consisting of a fixed inventory of 1e17 particles is present across the entire simulation set. All charge states of neon are fully resolved, meaning neutral neon atoms (and the associated atomic reactions) are treated by the EIRENE code and continuity, momentum, and energy balance equations are solved for all ten charge states in the B2 fluid code. The neon is primarily localized next to the core in the intermediate region between the primary and secondary separatrices, rather than radiating in the divertor legs and away from the core plasma. Since the overall contribution of neon to the overall energy balance in the transition to plasma detachment is small, we do not anticipate that the impact of this trace impurity was significant on the analysis presented here. However, it is noted that the localization of the neon close to the core, even in this trace amount, is not ideal for future reactor-relevant situations. While neon is often considered to be a favorable radiator because it is inert and will not introduce complexities with molecule formation, strong localization to the core plasma can decrease core performance, which should be avoided, and further study is required to understand the distribution and spread of impurity radiation in these long-leg configurations.

5.5 Conclusions

A scan of plasma particle count is performed with the SOLPS 4.3 code package to assess the physics of detachment in a long-leg divertor configuration, which is a promising mitigative feature of the magnetic topology used in many alternative divertor configurations. Up-down and in-out divertor asymmetries are observed, with plasma behavior in the primary divertor that is consistent with experiments and modeling of other long leg divertor geometries. Across this scan, which displays the typical “rollover” of ion flux to the material surface as the plasma detaches, it is observed that the physics-based scaling relationship between upstream plasma pressure and incoming divertor heat flux during plasma detachment corresponds well to the existing physical understanding of divertor detachment in “standard” divertor configurations. However, in the absence of impurities, significant spreading of the heat flux and losses to the side walls from perpendicular transport are required for the "normal" atomic and molecular detachment processes to begin, and a new energy balance is suggested for long leg configurations to address the perpendicular energy losses, as Equation 5.2. The influence of losses to the side walls, characterized here as $Q_{\perp}$, was not initially identified as an important component of the scrape-off layer energy balance, but appears to be significant in long leg geometries [20, 81]. Once detachment proceeds, a synergistic effect between the limitation of cross-field transport and divertor plasma recombination and detachment is observed. Overall, the existing theory and many features of divertor plasma detachment in standard divertors appear to translate to long leg divertor geometries. With this foundation, several other key aspects of the physics of long leg divertors can be studied in future simulations, including the spread of impurity radiation, since this study indicates that localization of impurity radiation to the core plasma might be a major concern.

5.6 Acknowledgments

Initial grids and equilibria for these simulations were generated by J. Canik and J. Lore of ORNL and heavily modified for this project. A.S. Kukushkin provided significant technical expertise and support to this project. This work was supported by the U.S. Department of Energy, Office of Science, Office of Fusion Energy Sciences under Award No. DE-FG02-04ER54739 at UCSD.

Chapter 5, in full, is a reprint of the material as it appears in "Energy and particle balance during plasma detachment in a long-leg configuration", in *Nuclear Fusion* by R. Masline and S.I. Krasheninnikov

(2023). The dissertation author was the primary investigator and author of this material.

Chapter 6

Mechanisms behind impurity spreading in a channeled, long-leg divertor configuration

Abstract

One suggested benefit of long-leg, tightly baffled divertor configurations, a common feature included in the designs of many next-generation fusion devices, is access to a delocalized "spread" of impurity radiation along the leg, allowing for a substantial radiation region while maintaining both sufficient distance from the core to prevent pollution of the plasma fuel and avoiding local overheating of the plasma-facing materials. However, it is unclear whether this increased connection length and divertor volume afforded by the long-leg configuration is compatible with impurity transport, and whether it will enable this desired impurity radiation spread at all. Here, the SOLPS 4.3 code is used to assess the distribution of nitrogen and neon impurity radiation in a long-leg, tightly baffled divertor geometry. There is a strong correspondence between the distribution of impurity radiation in the long leg and impurity recycling on the divertor side walls with both the nitrogen simulation set and the neon simulation set, suggesting that impurity spreading along these long legs is due to the interplay between the cross-field transport and associated neutralization of the impurity on the material surfaces.

6.1 Introduction

Impurity radiation in the plasma edge is vitally important for power dissipation and divertor detachment [16]. In reactor-relevant regimes, this impurity radiation must provide enough dissipation to reduce incoming power and protect the material surfaces without reducing core plasma confinement, and the

impurity must remain localized to the divertor region to prevent diluting or poisoning the plasma with intrinsic or injected impurity. However, to avoid local overheating of the first wall, the impurity radiation must also be spread throughout the volume of the divertor leg, necessitating compatibility of the location and distribution of the radiation with these requirements of the core and material surfaces. Additionally, although stable impurity radiation localized at the X-point (as an X-point radiator, or XPR) has recently been demonstrated as a suitable option for reducing energy fluxes into the divertor in tungsten-walled machines [10, 11, 101–104], strong radiation at the X-point can cause excessive plasma cooling and trigger unstable MARFEs [15] that can lead to radiative collapse in machines with other wall materials that are susceptible to higher chemical erosion [33, 105–107], meaning that a stable XPR and mitigation of MARFEs is dependent on the specific tokamak design and operating conditions and that radiation localization might not be compatible with all future reactor designs [24]. One promising solution that enables a fair spread of impurity radiation along the divertor leg (away from both the core plasma and the material surfaces) are long-leg divertors, which are common features used in many proposed alternative divertor configurations and included as integral components in the design of conceptual tokamaks [23, 32, 93, 108] and future fusion pilot plants [109]. These long legs, usually situated in the outer divertor, allow for a larger plasma volume in the divertor and a longer connection length, both of which are favorable for containing and enhancing radiative losses.

Enabling a strong, stable spread of the radiation front across the divertor leg is one of the hallmark design features of the long outer leg, and this effect has been studied in many simulations [7, 8, 79, 80]. Studies [8, 79, 80] of the ADX conceptual tokamak across several alternative divertor configurations with long outer legs (including an X-point target divertor, Super-X divertor, and long vertical leg divertor) using the UEDGE plasma edge code [51] show desirable spreading of impurity radiation along the entire outer leg in high-power discharges. However, the calculations used in the UEDGE code to determine radiation losses use the "fixed fraction" model for radiative dissipation, which does not include any characterization of impurity transport and tends to overestimate radiation losses [110]. While the results shown in this work are promising for the viability of radiation spreading in the long leg since they indicate that favorable temperatures for impurity radiation can be achieved along the divertor leg, the limitations imposed by the fixed fraction for radiative losses justify further investigation with a higher fidelity model. Simulations

[7] of the MAST-U divertor (using several different iterations of the Super-X divertor) using the SOLPS code, which features a multispecies model for radiation that calculates contributions to radiative losses for each charge state of impurities individually, show strong radiation spreading along the entire length of the long outer leg. Spectroscopic investigations of plasma detachment of MAST-U seem to corroborate the distributions of neutral and impurity radiation shown in this work, albeit with much lower input power and an intrinsic carbon impurity instead of seeded nitrogen [111]. However, the mechanisms that cause the impurity spreading observed in these simulations and experiments are unclear. In the simulations, the regions of substantial radiative losses associated with the impurity species coincide with regions of hydrogenic neutral radiation that is also spread all along the outer leg. Though it was not discussed in these works, the only source of hydrogenic neutrals available at the temperatures consistent with impurity radiation is from plasma recycling on the divertor side walls. It is feasible that the impurities, which would also be subject to the side wall recycling, are spread along the leg as a result of perpendicular transport and recycling on the side walls. Additionally, recent simulations [112] have indicated a strong influence of perpendicular transport on the overall plasma state for a channeled, long-leg divertor configuration, which shares several features with the alternative divertor configurations described here. These simulations also included a trace neon impurity, which was localized near the core plasma rather than radiating in the legs and warrants further investigation.

In this work, we assess the mechanisms behind impurity radiation spreading in a long-leg divertor configuration with tightly-baffled channels along all the divertor legs by studying the effects of cross-field transport on the distribution of impurities in the edge and divertor plasma. We use the SOLPS4.3 code, following a similar approach and using the same computational grids detailed in other studies [93, 112], to scan impurity concentration across simulations with fixed deuterium content and fixed input power, and vary the transport coefficients used in the simulation to asses the impact of small and large transport coefficients on the impurity distribution. One simulation set features a nitrogen impurity and the other features a neon impurity to rule out species-dependent effects on impurity distribution in the edge plasma. These simulations show that for both species, impurity radiation spread is largely dependent on cross-field transport to the divertor side walls and associated impurity recycling processes. Section 6.2 provides details on the simulation setup and parameters for these scans. Results are shown in Section 6.3, while

analysis and discussion are presented in 6.4. The conclusions are presented in Section 6.5.

6.2 Simulation setup

Simulations for this work were performed using the SOLPS 4.3 code package [35, 45], which is comprised of the implicit B2 multifluid plasma edge code for all ion species and electrons to solve the plasma state and the explicit 3D Monte Carlo code EIRENE to evaluate neutral trajectories and atomic processes. Together, self-consistent equations for continuity, momentum, and energy are solved in a realistic magnetic configuration of a tokamak, with classical transport along the field lines and some "anomalous" cross-field contributions approximated as a radial diffusion. These calculations are used as a background plasma for an EIRENE calculation of the state of the neutral particles, where a corresponding grid is overlaid over the plasma domain where the plasma densities and temperatures are used to calculate neutral trajectories and detailed atomic processes, such as ionization, charge exchange, elastic collisions, and radiation. No neutral-neutral collisions are included, but are not expected to have a significant impact [113]. Collisions between the neutral neon species and the main deuterium ion species are included, while collisions between the neutral nitrogen species and the main deuterium ion species are not included because they are not available in the AMJUEL reaction database used by the EIRENE code [42]. Molecule-activated recombination processes (MAR) were not included since the MAR process is not expected to contribute significantly to the effective recombination in the divertor plasma at high densities and temperatures [87]. Drifts were not used in these simulations, as the drift model is not included in the SOLPS4.3 code package.

The computational grid is the same as the one featured in other studies [112], with a heat flux width λ_q of 0.2 mm and a disconnected double null configuration [91] with tightly baffled outer divertor legs in both the upper and lower divertors. The toroidal field is 12.2 T. Both inner divertors are short, relative to the long outer leg, but also have tight baffling. We will refer to the surfaces along the sides of the divertor legs as the "side walls". The computational grid for the plasma state is shown in Figure 6.1. As shown in the figure, the unbalanced double null is biased towards the lower divertor, which will receive the majority of the fluxes in the computational domain, and is denoted as the "primary" divertor, while the upper divertor is denoted as the "secondary" divertor, to avoid a loss of generality in this work. The

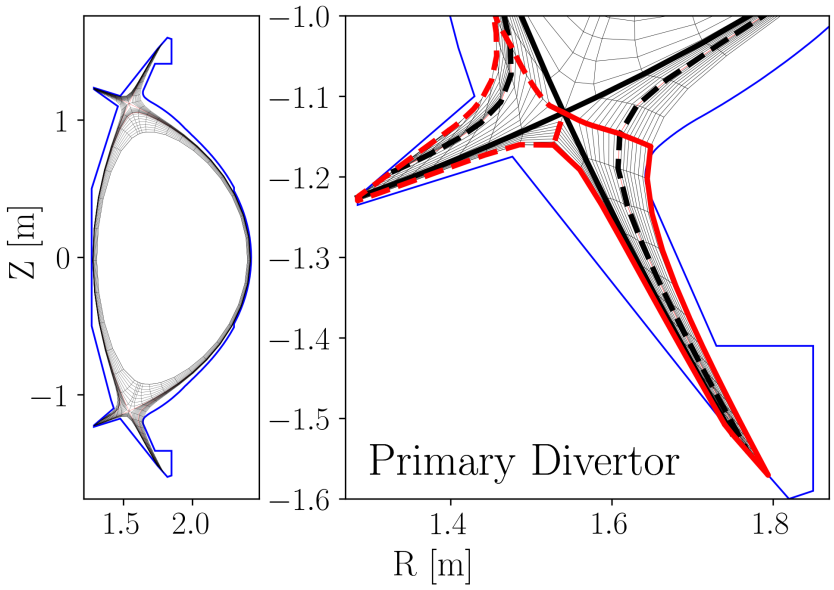

Figure 6.1. The simulation grid. The grid for the B2 plasma code is shown in the thin black lines, the primary separatrix is denoted with the thick solid black lines, the secondary separatrix is denoted with the thick dashed black lines, and the vacuum vessel geometry (and the extent of the domain of the EIRENE neutrals) is approximated in blue. The primary divertor is identified in red, with solid red lines corresponding to the outer divertor and dashed red lines referring to the inner divertor.

distance between the two separatrices is 2 mm at the midplane, while the full scrape-off layer width is 5 mm at the midplane, with an additional 2 mm gap between the very edge of the scrape-off layer and the vessel wall. All losses to the radial boundaries of the computational domain are assumed to be losses to the material surfaces.

In these simulations, boundary conditions were selected to achieve a "closed box" setup for particles to emulate the physics of the high-recycling regime [114]. A fixed particle content provides a more natural evolution of plasma parameters for physics studies, and is more likely to capture behaviors such as hysteresis or bifurcations that could be obscured or otherwise not captured by manipulating the upstream density or other boundary settings as the control parameter for the scan. In these simulations, fixed particle content enables the precise examination of the physics that are specific to the impurity species, as opposed to capturing other effects (like density changes inducing ionization/recombination effects that will have significant impacts on the overall material and energy balances) that are more general to the divertor

plasma.

To enable the closed box configuration, recycling is set to 100% at the targets and all boundaries, where all ions hitting the boundaries and material surfaces are neutralized and reflected back as neutral particles. To maintain a fixed number of particles, there is zero flux from the core and no specific puff or pump included at any location. Because there is no particle source, it is not possible to use source scaling terms, the usual particle conservation technique used in the SOLPS code [115] to compensate for inherent particle losses that are an unavoidable consequence of the implicit-explicit coupling between the implicit fluid and explicit Monte Carlo codes [35]. Without these corrections, these slight mismatches in the particle balance between the coupling steps can become significant over the course of the thousands of iterations required to achieve steady state. Instead, particle count is maintained at a user-specified level for each species using a unique feedback system in the SOLPS 4.3 code framework, which has been shown to have no impact on steady state plasma parameters when enabled [116]. The feedback system has two components, both of which are controlled independently, and can be applied to one or multiple species in the simulation space: one element at the core-edge interface that dynamically adjusts a flux of the main ion species based on neutral/plasma fluxes at the core-edge boundary to assure zero flux at the core, and the other element along entire outboard wall, providing a source of neutral gas that is spatially uniform and continuous from upper outer target plate to lower outer target plate. During every iteration, the feedback system on the outer wall takes the input/output total number of particles of the given species and adjusts a very small gas puff that is emitted uniformly across the entire outer wall that will introduce an equivalent number of new particles to compensate for any loss from the coupling step. For each individual call to the feedback system, the relative magnitude of the effective puff is only a few fraction of a percent of the overall particle flux calculations in the code (which includes the fluxes from atomic processes and surface interactions), making it largely inconsequential to the physics resolved by the code in each individual step, but crucial for maintaining the overall particle balance over thousands of iterations of the code. Once the system reaches steady state, the fluxes determined by the feedback system no longer change; the final values of the flux determined by the dynamic response are maintained at this level, which prevents changes in the steady state that might result from Monte Carlo noise.

Using this feedback system, the total number of deuterium and impurity particles is held fixed in each

simulation, and the simulation is run to steady state. The steady state simulation is then replicated, the impurity content is incrementally adjusted while all other parameters are held fixed, and the simulation is run to steady state with this new impurity content. This process is repeated several times across a wide range of impurity content, denoted here as $\xi_{N,Ne}$, such that

$$\xi_{N,Ne} = \frac{N_{N,Ne}^{edge}}{N_{D}^{edge}},$$

where $N_{N,Ne}^{edge}$ corresponds to the total number of particles of nitrogen and neon in the plasma edge, respectively, and N_{D}^{edge} is the total number of deuterium particles in the plasma edge. We refer to the "plasma edge" as the region of the B2 simulation domain that includes the divertors, private flux region, and scrape-off layer, but does not include the region of the core plasma included in the B2 grid. A simulation was selected with $N_{D}^{edge} = 2.3e20$ particles to use as a starting point for both the nitrogen simulation set and neon simulation set. We note that a "fixed particle content" is not repeatable in an experimental context, where impurity content in the edge is usually maintained by a controlled puff of impurity gas into the divertor region, and emphasize that these studies are intended to guide our theoretical analysis and provide a thorough examination of the possible physics mechanisms at work that may inform experimental operation, rather than to serve as a guide for any real experiment.

This feedback system is implemented in the SOLPS4.3 code package and has been extensively verified [116], which enabled the use of the "closed box" setup used in these simulations. We are not aware of the status of any similar feedback system in the SOLPS-ITER code package, which is largely why SOLPS4.3 was used for this work instead of the SOLPS-ITER code package. We are aware that the SOLPS 4.3 code package does not contain several modules that are available in the SOLPS-ITER code package, which features a different formulation of the underlying equations that enables the study of drifts, and a recent upgrade that includes a more complete description of parallel impurity transport [117–119] that incorporates fully multi-ion collisional Grad-Zhadanov closure for the thermal force model into the code. Despite these new functionalities, we are aiming to study the physics of the cross-field transport of the impurity in this work, which necessitates the use of the "closed box" model, and we do not think the inclusion of drifts or an improved parallel transport model will significantly impact our

conclusions. We expect that the influence of drifts would be minimal, since drift effects are minimal in the presence of a strong magnetic field (a toroidal field of 12.2 T is used in this work), and that the effects of drifts on SOLPS-ITER simulations using similar disconnected double null configurations (like the one used in this work) were shown to be negligible [90]. The aim of this work is to study the impact of perpendicular transport, and despite the updates to the parallel transport model, the cross-field terms are retained across all impurity models, and provide a reasonable estimation of the qualitative behavior of the perpendicular transport of the impurity in the simulation, which is the primary focus of this analysis. As it stands, SOLPS4.3 and SOLPS-ITER have evolved enough that they can and should be considered different tools, and SOLPS4.3 is the appropriate tool for the physics study in this work.

These simulations are performed with 30 MW of input power exiting the core, split evenly between ions and electrons. Cross-field transport coefficients are constant and set at $D_\perp = 0.3\ m^2 s^{-1}$ and $\chi_\perp = 1\ m^2 s^{-1}$ for particles/momentum and heat flux, respectively, in scans of impurity content for both species (denoted as "large" transport coefficients) and reduced to $D_\perp = 0.1\ m^2 s^{-1}$ and $\chi_\perp = 0.33\ m^2 s^{-1}$ for a comparison case (denoted as "small" transport coefficients) for both species. The B2 surfaces along the scrape-off layer and private flux region have boundary conditions of a 3 cm decay length for temperature and density, and energy fluxes out of these surfaces are assumed as losses to the walls. The Bohm sheath boundary condition is applied at the targets.

6.3 Simulation results

Scans for both nitrogen and neon impurity species were performed using the "large" transport coefficients. The distribution of the impurity particles is shown in Figures 6.2(a) and 6.2(b). In this configuration, the impurity particles are primarily localized in the primary divertor and scrape-off layer for both species. Because of this, the impurity radiation in the divertor region is also primarily localized to the primary divertor, so the secondary divertor will be ignored for this analysis.

6.3.1 Scans on impurity content

The scans on nitrogen and neon shown here use a feedback condition on the total number of impurity particles in the edge plasma relative to the total number of deuterium particles (both ions and neutrals) in the edge plasma, which only includes the divertor, private flux, and scrape-off layer regions of the B2

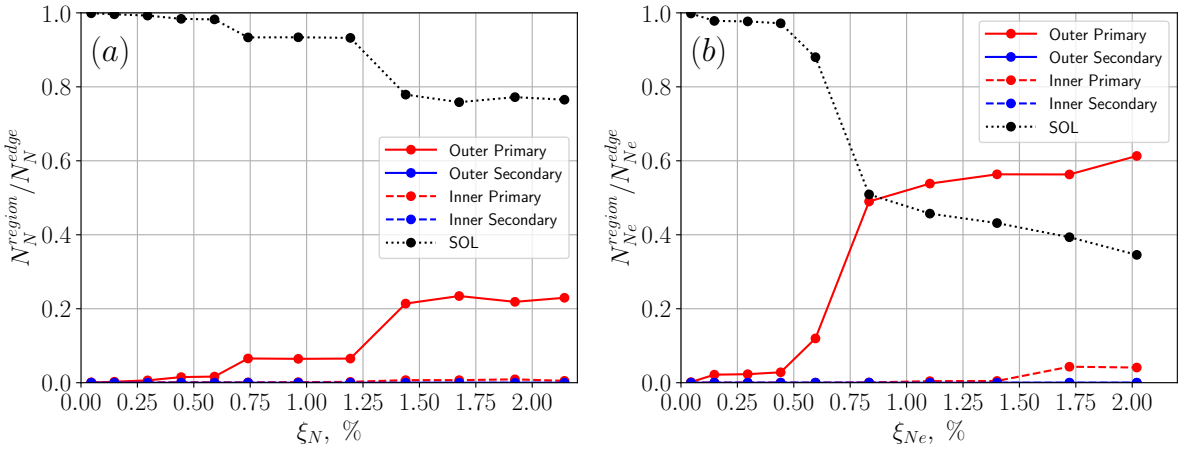

(a) Fraction of nitrogen particles in each region.

(b) Fraction of neon particles in each region.

Figure 6.2. Impurity particle content in each divertor leg relative to the total impurity content in the edge, versus the impurity particle content in the edge relative to the total number of deuterium particles in the edge.

domain. This specifically excludes the component of the computational domain in the region of the core plasma: particles from the edge are free to travel to and from this region, but a particle from the edge that enters the core region will no longer be counted for the feedback condition, while a particle from the core region transferring into the edge region will be counted for the feedback condition. These settings were chosen to enable a more careful study on the specific behavior of the impurity in the divertor legs, and give insight on the compatibility of the power handling requirements imposed on the specific impurity with possible core accumulation. This means, however, that there is some variation in the power crossing the separatrix into the scrape-off layer, since the impurity content in the core does not necessarily reflect the same $\xi_{N,Ne}$ ratio used as the tuning parameter for the particle scan. The fraction of the total input power radiated in the core region can be seen as the dashed black line in Figure 6.3, where the fraction of radiated power in the core never exceeds roughly 10% (Figure 6.3(a)) for nitrogen and roughly 15% for neon (Figure 6.3(b)).

6.3.1.1 Nitrogen

Across this scan, the majority of the nitrogen particle content in the plasma edge is localized to the scrape-off layer region, with a larger fraction in the outer primary divertor only at the highest densities, which is shown in Figure 6.2(a). Compared to the neon density distribution (which will be discussed in

detail in the next section), more nitrogen stays in the scrape-off layer for equivalent concentrations of each impurity than for the neon simulations. Leakage of impurities into the main chamber scrape-off layer region has been noted to occur because of frictional coupling with the main ion species, with more or less efficiency depending on the location of the region of the greatest ionization potential of the respective impurity species and the location of the poloidal flow velocity stagnation points [120, 121]. Although neon ionizes closer to the X-point than nitrogen, we do not observe increased impurity leakage into the upstream scrape-off layer region compared to nitrogen. Instead, it is likely that the strong gradients in the temperature that result from the more efficient radiation from neon impact the flow velocity profile of the main ion species and result in higher flows of the impurity species towards the divertor legs; further analysis on this subject is beyond the scope of this work. This hypothesis is consistent with low nitrogen radiation in the divertor legs, which only increases with increased nitrogen particle content in the outer divertor leg. The fraction of the total power radiated from impurities across the scan is shown in Figure 6.3(a), and decomposed into the total radiated power from nitrogen in each region; nitrogen radiates very little in the scrape-off layer region and only radiates a small amount in the inner primary divertor leg at high impurity concentrations. Overall, about half of the total power radiated from the impurity species is radiated in the divertor leg, as shown in Figure 6.4(a). The plasma parameters, including electron temperature and peak heat flux at the outer target, as well as Z_{eff} and ion density at the separatrix midplane, for nitrogen are shown as the red solid line in Figure 6.5.

6.3.1.2 Neon

In the scan of increasing neon particles, the majority of impurity particles are initially concentrated in the scrape-off later, but the proportion of particles in the outer divertor leg increases with increasing neon content, shown in Figure 6.2(b). There is considerable radiation in the core across all simulations (Figure 6.3(b)) which is higher than the simulations with equivalent concentrations of nitrogen. Radiation in the scrape-off layer region remains fairly low, while radiation in the divertor leg eventually increases, and remains fairly consistent for the remainder of the simulation set. The total radiated power from the neon impurity "saturates" to this level at lower concentration than the nitrogen impurity scan. Like nitrogen, about half of the overall impurity radiation is in the outer divertor leg, although there is some contribution to the total balance of radiated power from the inner divertor leg at the highest concentrations (Figure

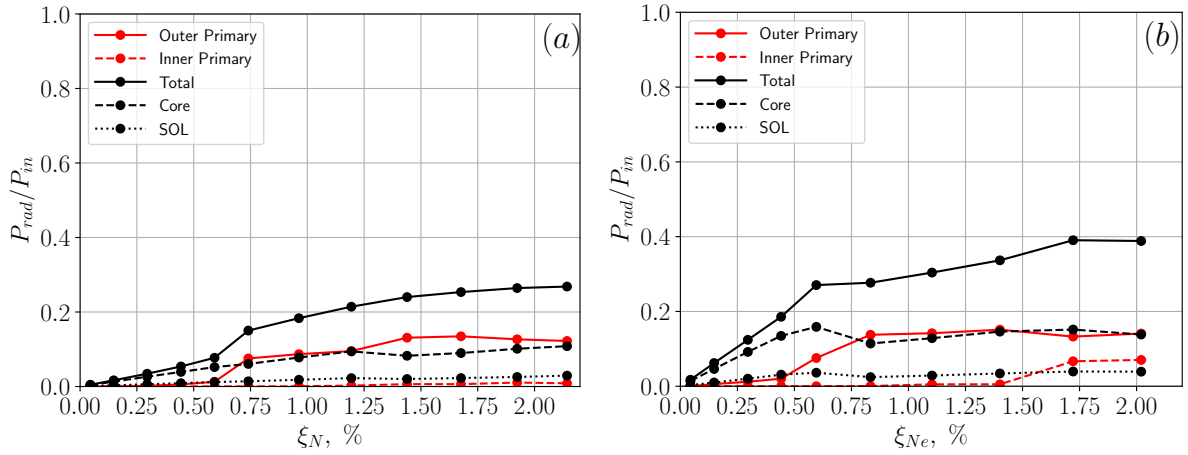

(a) Fraction of nitrogen radiation relative to the total input power.

(b) Fraction of neon radiation relative to the total input power.

Figure 6.3. Total radiation from impurities in the simulation domain, broken down into each "region" of the edge plasma and core, relative to the total input power $P_{in} = 30$ MW.

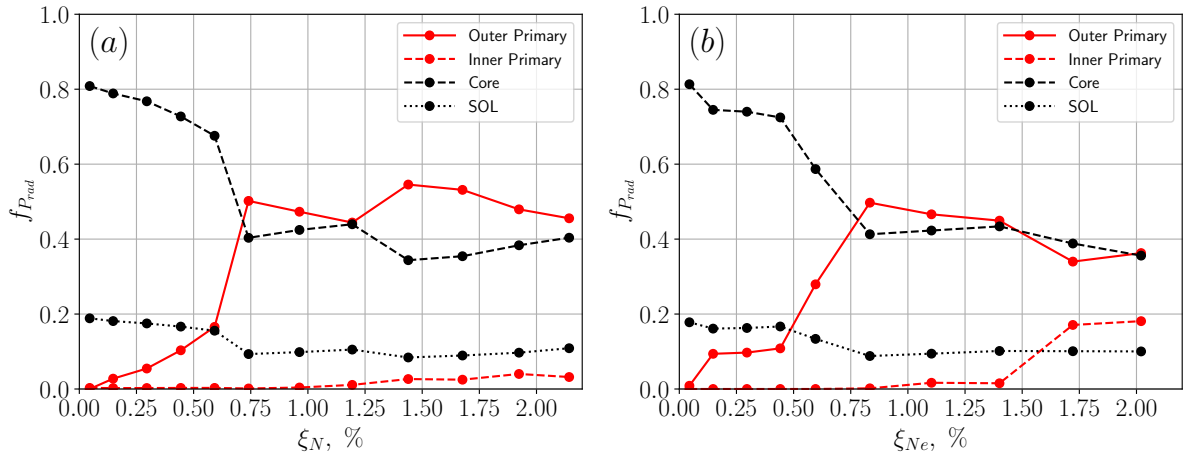

(a) Fraction of total nitrogen impurity radiation in each region.

(b) Fraction of total neon impurity radiation in each region.

Figure 6.4. Fraction of total radiation from impurities in each "region" of the simulation domain (edge and core) relative to the total impurity radiation in the entire simulation domain.

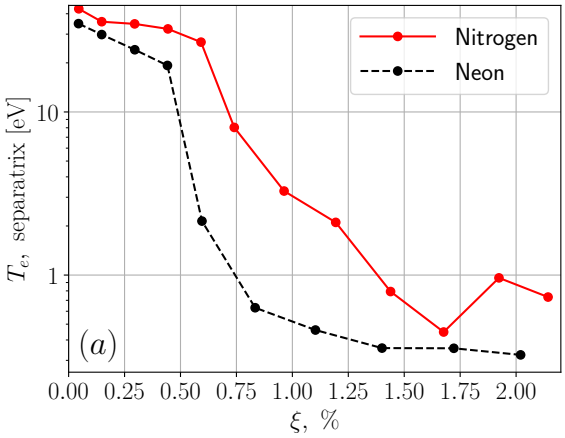

(a) Outer target electron temperature, just outside the separatrix.

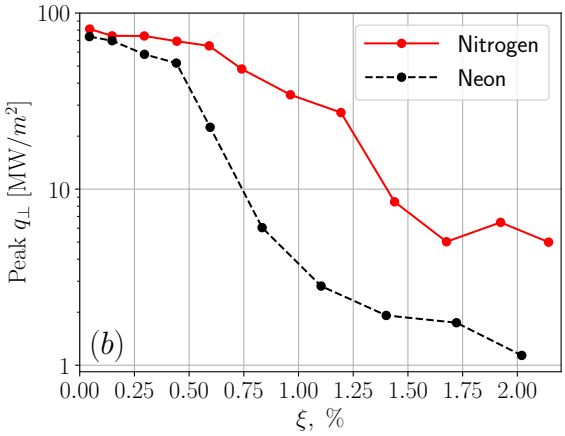

(b) Peak perpendicular heat flux at the outer target.

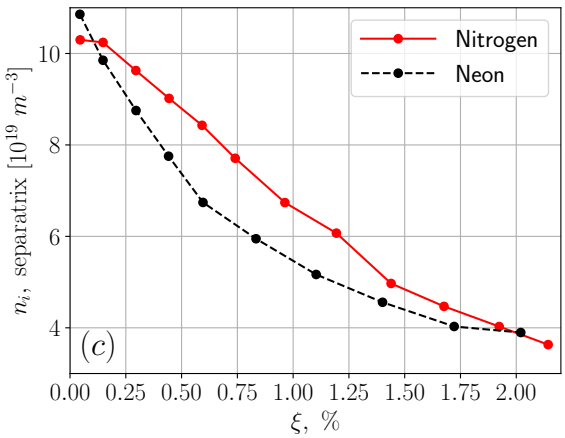

(c) Main ion density at the outer midplane.

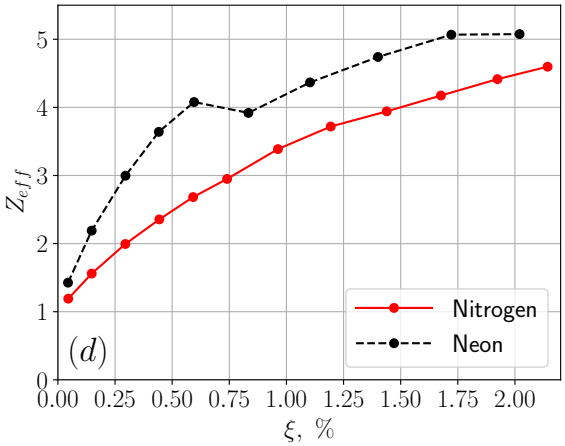

(d) Effective charge at the separatrix at the outer midplane.

Figure 6.5. Plasma parameters. Nitrogen is shown in the solid red line and neon is shown in the dashed black line. Figures (a) and (b) are taken at the outer target, and Figures (c) and (d) are taken at the outer midplane.

6.4(b)). The plasma parameters for neon taken at the outer target and the separatrix midplane are shown as the black dashed line in Figure 6.5.

6.3.2 Impurity radiation distribution

To assess the distribution and spreading of impurity radiation in the outer leg, a simulation with considerable impurity radiation in the outer leg was selected from the each of the scans for further analysis. The distribution of impurity radiation is shown in Figure 6.6(a) for nitrogen and 6.7(a) for neon. Both of these cases show considerable spread of impurity radiation along the outer leg, with the radiation front (the region with the majority of the overall radiation) positioned away from the target and the core.

The corresponding first ionization of the impurity species (going from the neutral particle to the first ionization state) for nitrogen and neon are shown in Figures 6.6(b) and 6.7(b), respectively. In both species, there is strong ionization near the edge of the B2 plasma domain (which is flush with the tight baffling of the divertor side walls) in both the inner divertor and outer divertor. In particular, the strong ionization region (shown in yellow) is thick towards the target and extends in a small sliver next to the wall all the way up the outer wall in the outer divertor, which corresponds with the regions of high impurity radiation in Figures 6.6(a) and 6.7(a). This near-wall ionization region going up the leg towards the X-point is more substantial for neon, but is still present for the nitrogen simulations.

To analyze this correspondence further, the total radiation in the outer divertor leg and the flux of all charge states of the impurity to the wall is shown in Figures 6.8(a) and 6.8(b) for nitrogen and neon, respectively, across the entire scan. Under the full wall recycling conditions used in these simulations, all impurity flux to the wall is neutralized and reflected back as neutral impurity particles. From this, there appears to be strong correspondence between an increase in recycling flux to the side walls and the total radiation in the divertor leg.

6.3.2.1 Reduced particle transport

Two simulations shown in Section 6.3.2 are repeated with reduced transport coefficients to assess the influence of cross-field transport and recycling on the impurity species. Deuterium particle inventory is maintained at $N_D^{edge} = 2.30e20$ for both species, while impurity particle inventory is held at $N_N^{edge} = 3.31e18$ particles for nitrogen and $N_{Ne}^{edge} = 3.96e18$ particles for neon, giving $\xi_N = 1.44\%$ and $\xi_{Ne} =$

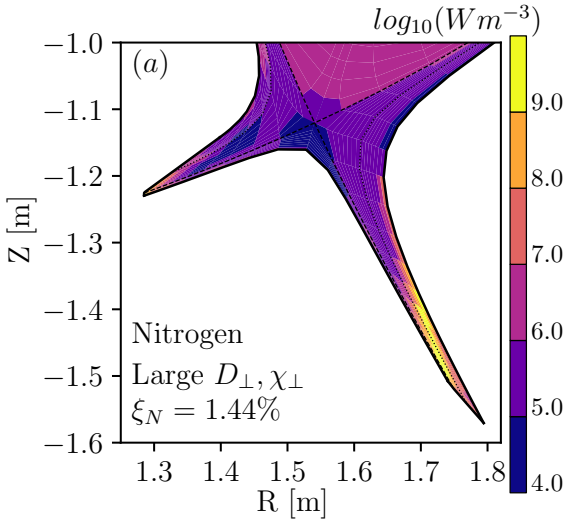

(a) Nitrogen radiation, large transport coefficients.

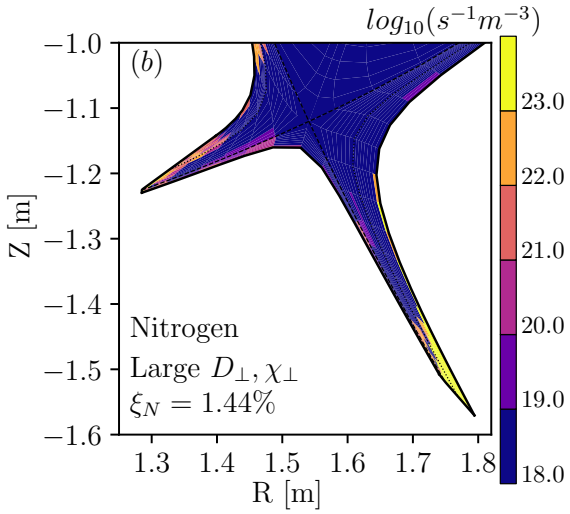

(b) First ionization of neutral nitrogen, large transport coefficients.

Figure 6.6. 2D Distributions for a simulation with 1.44% nitrogen impurity and large transport coefficients.

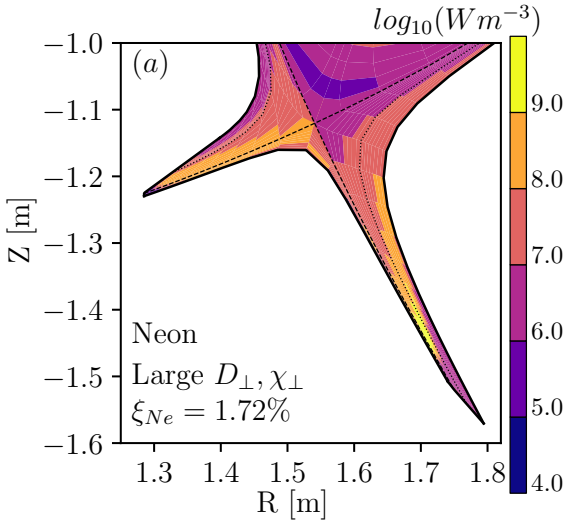

(a) Neon radiation, large transport coefficients.

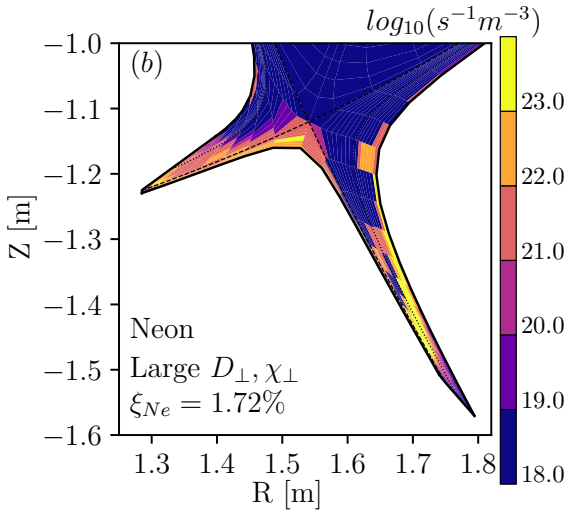

(b) First ionization of neutral neon, large transport coefficients.

Figure 6.7. 2D Distributions for a simulation with 1.72% neon impurity and large transport coefficients.

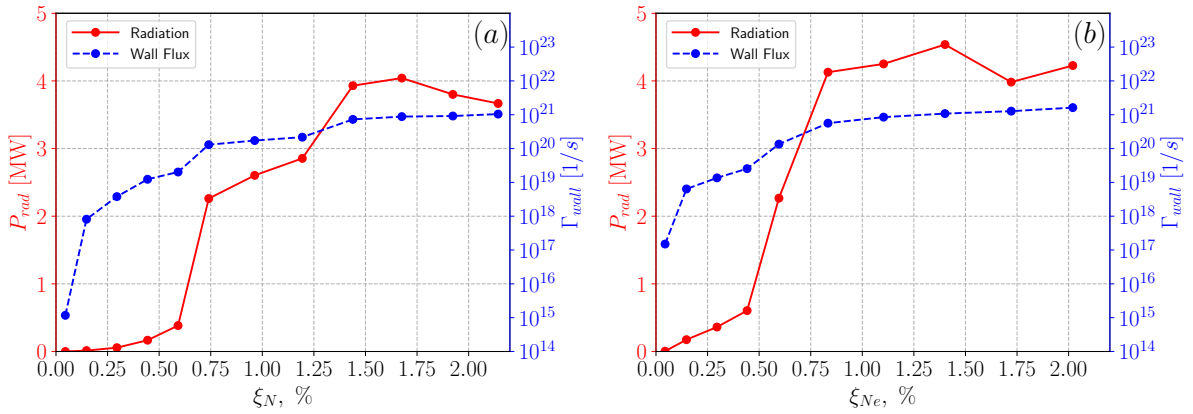

(a) Nitrogen radiation and impurity ion fluxes to the outer divertor wall.

(b) Neon radiation and impurity ion fluxes to the outer divertor wall.

Figure 6.8. Radiation from impurity species (red solid line) recycling/neutralization of impurity along side walls (blue dashed line) versus increasing impurity concentration for simulations with large transport coefficients.

1.72%. The transport coefficients for both the plasma and impurity species are reduced to a factor of $1/3$ of the "large" values for each simulation, giving values of particle and heat flux of $D_\perp = 0.1\ m^2 s^{-1}$ and $\chi_\perp = 0.33\ m^2 s^{-1}$, respectively. The distributions of impurity radiation and impurity ion source are shown in Figure 6.9 for nitrogen and Figure 6.10 for neon. Values of radiation and flux of impurity ions to the side walls, for the associated species and transport coefficients, are shown in Table 6.1.

6.4 Analysis and Discussion

6.4.1 Plasma parameters

Parameter scans were performed with large transport coefficients for both species. Across the simulation sets, neon radiates more in the core than the nitrogen, seen in Figure 6.3 and Figure 6.4. Higher neon radiation in the core relative to nitrogen has been observed in other simulations [120, 122–125] and seen in experiments [126–130]. The fraction of total radiated power in each region of the edge is fairly consistent between both simulations, except neon has considerably more radiated power in the inner divertor (which is a "standard" leg length) than nitrogen at higher impurity concentration. Both the increased core radiation and radiation in the inner leg observed in the neon simulations are namely due to the differences in radiation potential between neon and nitrogen, which is shifted to higher temperatures

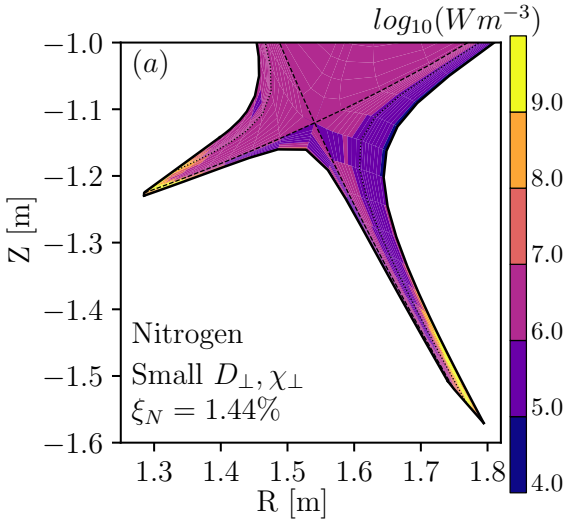

(a) Nitrogen radiation, small transport coefficients.

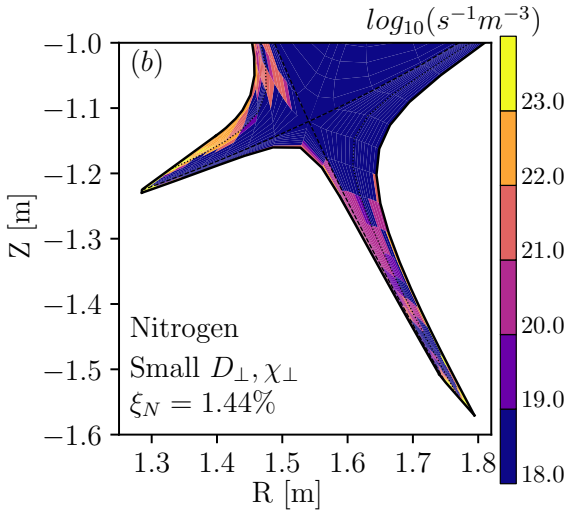

(b) First ionization of neutral nitrogen, small transport coefficients.

Figure 6.9. 2D Distributions for a simulation with 1.44% nitrogen impurity and transport coefficients small to 1/3 of the large values.

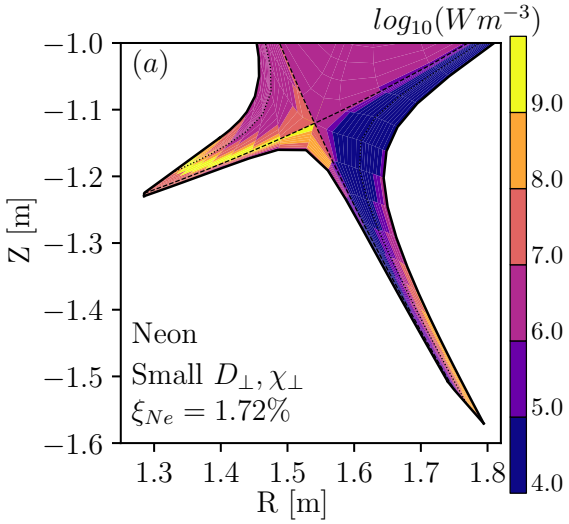

(a) Neon radiation, small transport coefficients.

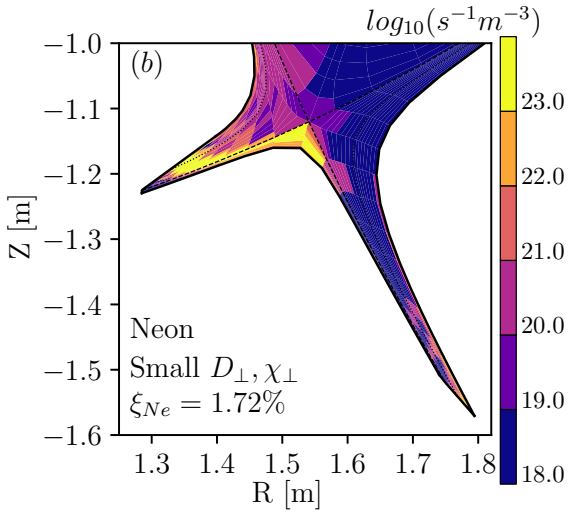

(b) First ionization of neutral neon, small transport coefficients.

Figure 6.10. 2D Distributions for a simulation with 1.72% neon impurity and transport coefficients small to 1/3 of the large values.

Table 6.1. Transport coefficients, total radiated power from impurity, radial particle flux to the divertor side walls for nitrogen and neon, and impurity particle distribution percentage for two different sets of transport coefficients, in the inner and outer legs of the primary divertor. Each simulation has a fixed inventory of impurity, relative to a inventory content of $N_D^{edge} = 2.3e20$ particles, noted as ξ. Peak $q_{\perp,out}$ has units of MWm^{-2}.

	Nitrogen		**Neon**	
$D_\perp$	0.3 m^2/s	0.1 m^2/s	0.3 m^2/s	0.1 m^2/s
$\chi_\perp$	1.0 m^2/s	0.33 m^2/s	1.0 m^2/s	0.33 m^2/s
ξ	1.44 %	1.44 %	1.72 %	1.72 %
P_{rad} (edge)	4.73 MW	6.87 MW	7.17 MW	6.92 MW
P_{rad} (core)	2.48 MW	0.84 MW	4.54 MW	4.04 MW
P_{rad} (outer)	3.93 MW	1.85 MW	3.98 MW	0.72 MW
P_{rad} (inner)	1.91 MW	4.65 MW	2.01 MW	6.09 MW
Peak $q_{\perp,out}$	8.5	143.7	0.2	15.4
Γ_{wall}, outer leg	7.3e20 s^{-1}	4.8e19 s^{-1}	1.3e21 s^{-1}	2.0e19 s^{-1}
Γ_{wall}, inner leg	1.0e19 s^{-1}	1.4e20 s^{-1}	6.7e19 s^{-1}	4.5e20 s^{-1}
N_{out}^{div}/N^{edge}	21%	3%	56%	2%
N_{in}^{div}/N^{edge}	1%	24%	4%	88%

(and therefore further upstream) for neon. Accordingly, the separatrix temperature and peak perpendicular heat flux (Figures 6.5(a) and 6.5(b)) at the target are lower for neon than in simulations with equivalent concentrations of nitrogen, since neon also radiates more effectively in the edge and the power crossing the separatrix is lower, because more power is radiated in the core. The reduction in main ion density at the midplane observed in 6.5(c) is a consequence of the increasing impurity density in the simulations and the closed box approximation, which forces the plasma species towards the divertor legs [18]; as the population of impurity species increases, more energy is radiated, the divertor plasma near the target becomes colder, and the plasma from the hot upstream region flows into the cold divertor recycling region [9].

6.4.2 Effective charge

The effective charge Z_{eff} shown in Figure 6.5(d) for both species is higher for neon than nitrogen, consistent with observations in other impurity studies [18]. Under these conditions, a high value of Z_{eff} is observed at the midplane for both species, which is achievable in the code, but would not be realistic for actual experiments. Despite this very high Z_{eff}, the fraction of the total power radiated from

the impurities is well under 40% across all simulations shown here, which is far below the necessary volumetric radiation losses to reach practical operating points. These values are consistent with estimates of impurity concentrations in similar tokamak geometries [93, 131]. It is concerning to see such a high Z_{eff} in order to achieve such a low radiation fraction, and raises questions about whether the core performance will be compatible for reactor-relevant conditions.

Between the results from this work and other simulations [18] and experimental data [29] of impurity radiation in long legs, from the perspective of Z_{eff}, there does not appear to be a benefit for core-edge integration from moving the radiation front away from the core plasma. From these simulations, the overall losses associated with impurity radiation are low, despite an increased divertor volume intended to provide a larger region for impurities to radiate, and the separatrix Z_{eff} is high, despite increased distance between the divertor radiation front and the plasma core. Similar effects were observed on TCV, where studies [29] on nitrogen seeding and divertor closure in alternative divertor configurations revealed no meaningful improvement in core confinement or core Z_{eff} by extending the radiation away from the core plasma.

6.4.3 Influence of cross-field transport

6.4.3.1 Divertor leg

Recycling along baffle surfaces was an important consideration reported in the design of the TCV baffles [100, 132, 133], and it appears to play a very important role here. In the long outer divertor leg, there is a considerable impact on the distribution of impurities from perpendicular transport on the side walls of the divertor, evident in the differences seen between the simulations with large transport coefficients (Figures 6.6 and 6.7) and the simulations with small transport coefficients (Figures 6.9 and 6.10). In the simulations with large cross-field transport coefficients, there is a significant correspondence between increases in the impurity radiation in the leg and fluxes to the side walls that does not appear to be directly correlated with a simple increase in particle count, seen in Figure 6.8(a) and 6.8(b) for each species. In the initial simulations, the impurity radiation is spread along the leg, away from the target plates and away from the core, which is the desired impact of this geometric choice. This is visible in Figures 6.6(a) and 6.7(a), where the yellow region (corresponding to strong impurity radiation) is spread along the leg and away from the target.

The strong recycling of the impurity species results in a strong incoming flux of neutral impurity, which are quickly ionized; the first ionization of the neutral species is shown in Figures 6.6(b) and 6.7(b) for each species. In both cases (with the neon case exhibiting a much stronger effect than the nitrogen), the source of ionized nitrogen extends all the way up the divertor leg, with very strong ionization in the region in the vicinity of the outer wall. For nitrogen, this ionization source is close to the target, but very strong along the outer wall and extending upwards, whereas for neon, the recycling/ionization region is strong at both the inner wall and all along the outer wall. These regions correspond to the regions of strong radiation in the corresponding Figures 6.6(a) and 6.7(a), where the majority of the impurity radiation happens slightly upstream (relative to the target) of the strong ionization regions. The long leg seems to facilitate the spread of impurities by allowing for an ionization and neutralization process along the leg's side walls. As impurity inventory increases, this ionization/neutralization process enables the impurity particles to "climb" towards the X-point, but not further: the recycling along the surface of the tight channeling in this configuration enhances dissipation related to the impurities, which in turn allows the plasma to cool below this region and near the target. This pushes the radiation front away from the target and towards the X-point, but eventually establishes a stabilized radiation region within the leg volume, where the interplay between dissipation and side wall recycling prevents the radiation region from climbing further towards the X-point or escaping the outer leg entirely.

In contrast, after reducing the transport coefficients, there is significantly less radiation in the outer leg and significantly less recycling flux to the side walls, described in Table 6.1. The radiation that does appear in the outer leg, shown in Figures 6.9(a) and 6.10(a), is primarily localized at and near the target, which is also where the majority of the first ionizations of the neutral impurity are taking place, shown in Figures 6.9(b) and 6.10(b). The region of the radiation localization is consistent with the charged impurity species being carried down the entire leg and neutralizing on the target, where it is re-ionized outside the separatrix, but still in the vicinity of the target plate, and not spread along the divertor leg. For both species, both the total power radiated in the leg and the total recycling flux is considerably lower with reduced transport coefficients, while the peak heat flux also significantly increases, listed in Table 6.1.

The reduction in transport coefficients results in a redistribution of the impurity particles between the divertor legs and scrape-off layer, with a compression of the impurity species at the inner divertor.

The shorter connection length and more dominant parallel transport effects relative to the perpendicular transport effects in these simulations cause the accumulation of the impurity species at the inner target, increasing both the impurity radiation in the inner divertor and the impurity wall recycling (recorded in Table 6.1). With the set of high transport coefficients, the impurity species is continuously moved across the magnetic field to be recycled and re-ionized along the outer divertor side walls, allowing the impurity species to remain in the outer divertor, and to spread along the leg. This effect is consistent with observations in other works which study the influence of impurities on alternative divertor configurations. In other simulations investigating the impact of perpendicular transport on impurities in a long-leg divertor configuration [134], no significant direct relationship between the total number of impurity particles and cross-field transport was observed. However, the simulations analyzed in that work used grids with an open private flux region and open SOL along the long divertor legs, whereas the grid used in the simulations shown here is closed on both legs, where the impurities can recycle along the surfaces of the tightly baffled walls and enhance radiative losses. Simulations of the large spherical tokamak STEP [135] with a standard-length, channeled inner divertor leg and long, channeled outer divertor leg show strong argon spreading along both legs, with similar characteristics of the spread and distribution of the first impurity ionization along the leg and near the walls observed in the 2D distributions shown in our simulations (though only the inner divertor was analyzed in detail).

6.4.3.2 Main chamber

The majority of the nitrogen particles are localized in the scrape-off layer region (Figure 6.2), whereas the majority of neon particles are localized to the outer divertor leg at higher impurity concentration. The localization of nitrogen in the scrape-off layer seems to be a consequence of the recycling of the perpendicular flux of nitrogen to the main chamber walls, which is much lower for neon (Figures 6.11(a) and 6.11(b)). Recycling contributes to the accumulation of impurity in the scrape-off layer region because in the edge plasma, an impurity particle will either be transported across the field line into the main chamber wall, where it will be neutralized and ionized, or it will be transported down the field line to the target, where it will be neutralized there instead. Once the particle is neutralized, it will be re-ionized, where it will radiate until it is neutralized on the wall, or neutralized on the target. Because of the narrow scrape-off layer width and proximity to the hot core plasma and the strong cross-field transport of the

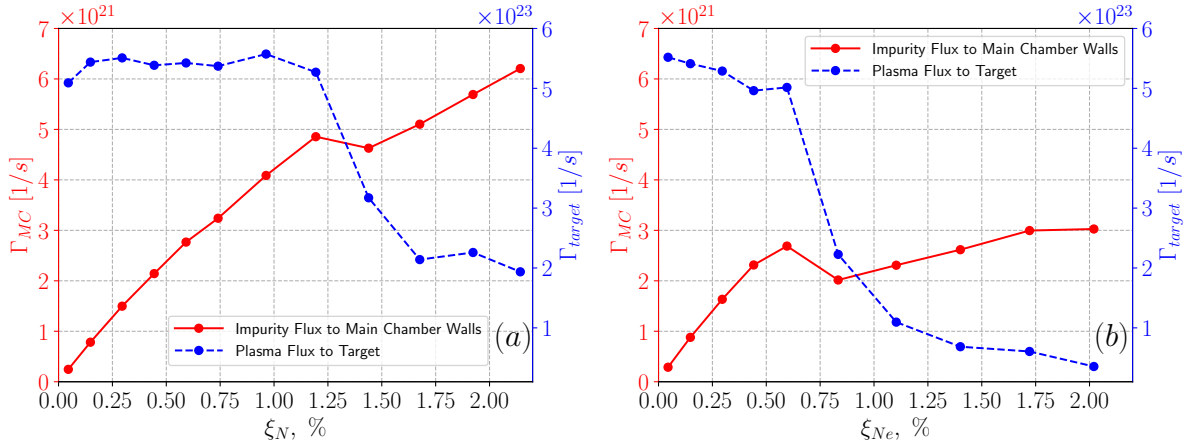

(a) Nitrogen ion fluxes to the main chamber wall and plasma flux to the target.

(b) Neon ion fluxes to the main chamber wall and plasma flux to the target.

Figure 6.11. Impurity flux to the main chamber walls and plasma ion flux to the target for each species.

nitrogen to the main chamber walls, the nitrogen is continuously neutralized and re-ionized on the main chamber surfaces, preventing the majority of nitrogen particles from leaving the scrape-off later and going into the divertor legs.

This effect is not observed in the neon simulations for two reasons: first, because the upstream cross-field transport is limited due to the onset of recombination in the outer leg, and because the neutral neon has a longer mean free path than the neutral nitrogen [122], and would be able to travel further away from the wall before being ionized. Previously, it was observed that the onset of plasma recombination in the divertor plasma limited further increases in cross-field transport due to the saturation of the upstream pressure [112], which appears to be the case here: the saturation of the main chamber recycling flux for neon saturates with the drop in ion flux to the target (also shown on both plots in Figure 6.11), which is a signifier of the onset of plasma recombination and divertor detachment. The nitrogen simulations only see a modest reduction in the ion flux to the target compared to neon at the highest impurity concentrations, and cross-field impurity flux to the main chamber walls never saturates. The strong recombination onset in the outer leg likely happens for neon and not nitrogen because the power radiated from the core is higher in the neon simulations, so there is lower power entering the divertor legs. It is also important to note that this accumulation effect is due to the close proximity of the main chamber wall to the bulk plasma (see the black grid relative to the blue wall in Figure 6.1), since the neutralized particles are not able to

"escape" re-ionization, making this effect dependent on the geometry of the device. However, the main chamber walls in the designs of many compact tokamaks with high fields are tightly enclosed around the core [23, 32, 93, 108, 109], and it is likely that this effect could also be observed on these machines that share this feature.

6.5 Conclusions

In this work, we have assessed the distribution of impurity radiation and identified a possible physical mechanism for the spread of impurity radiation in a long-leg, channeled divertor configuration with high input power. Across many simulations with increasing concentrations of nitrogen and neon impurities, nitrogen and neon show similar behavior, although nitrogen radiation is primarily localized to the outer divertor, while neon radiation increases in the inner leg and at the X-point at higher impurity concentrations. Overall, these simulations show low impurity radiation with very high Z_{eff}, which might be incompatible with core performance required for reactor conditions. The spread of impurity radiation along the long outer leg shows strong correspondence with the neutralization of the ionized impurity particles along the side walls for both species. This effect disappears when transport coefficients and resultant wall recycling are reduced, and the impurity species is localized at the divertor target under these conditions, suggesting that this mechanism is the cause of the stable, delocalized radiation front often observed in simulations of long-leg divertors.

Acknowledgements

Initial grids and equilibria for these simulations were generated by J. Canik and J. Lore of ORNL and heavily modified for this project. A.S. Kukushkin provided significant technical expertise and support which enabled this project. This work was supported by the U.S. Department of Energy, Office of Science, Office of Fusion Energy Sciences under Award No. DE-FG02-04ER54739 at UCSD.

Chapter 6, in full, has been submitted for publication of the material as it may appear in "Mechanisms behind impurity spreading in a channeled, long-leg divertor configuration", submitted to *Physics of Plasmas* by R. Masline and S.I. Krasheninnikov [136]. The dissertation author was the primary investigator and author of this material.

Chapter 7

Conclusions

Magnetic confinement of a plasma fuel using a tokamak device is one of the most well-developed paths to achieving the nuclear fusion process on earth, but there are still many gaps in understanding the physics at work in this approach. A critical component of a tokamak is the exhaust system (the "divertor") which directs heat and particle exhaust away from the confined core plasma. To avoid deleterious effects of this plasma exhaust interacting with the material surfaces of the divertor, the plasma must be extinguished from $\sim 10^4$ eV to ~ 1 eV, while maintaining high temperatures in the core plasma to sustain the fusion reaction. Several new divertor features have been suggested that could introduce or enhance various processes that might protect material surfaces, but a thorough physics analysis of these proposed configurations has not been conducted, and it is unclear whether these desired improvements can actually be achieved using these novel techniques. Here, we have used numerical simulations to assess the physics associated with two features that have been suggested to improve conditions of the plasma exhaust in the divertor: the "inverse" plasma sheath and long-leg divertor configurations.

In Chapter 4, we investigated the impact of the recently-proposed "inverse" plasma sheath at the plasma-material interface using the 2D edge plasma modeling code UEDGE. The inverse sheath, which is thought to repel (rather than accelerate) ion flux towards the target, was suggested [5] as a novel mechanism to promote divertor detachment by ion repulsion and subsequent charge-exchange-induced cooling and as a preventative measure to avoid material erosion. To investigate this claim, our study involved the first reported implementation of a non-Bohm sheath boundary condition at the divertor targets, where the ion particle and energy flux boundary conditions were set to zero to emulate the physics of the

inverse sheath regime. In our simulations, we observe no tangible impact on plasma cooling resulting from the inverse sheath, and a significant increase in specific heat flux to the target from electrons, which are now free-streaming to the target. We do observe bifurcations in our solution set across increasing plasma density, which are not observed in the comparative solution set with the standard Bohm plasma sheath. These bifurcations are present in simulations with and without impurity radiation, in simulations with no drifts and constant transport coefficients, leaving the only likely cause of the bifurcation to be an effect related to temperature sensitivities associated with plasma recombination that leads to a redistribution of particles in the divertor. To elucidate upon this recombination-induced bifurcation, we describe an analytical model for the bifurcation that is consistent with the plasma parameters observed in our simulations, which suggests the presence of two separate sets of stable solutions that correspond to low and high neutral pressures.

Starting with Chapter 5, our study changed focus to assess the physics of detachment in a long-leg divertor configuration with tight baffling along the divertor legs, which are common features of the magnetic topology and vessel design used in many alternative divertor configurations and next-generation fusion machines. To establish a baseline for the physics of the transition to detachment in these configurations, we used the SOLPS4.3 plasma edge code to simulate a disconnected double-null plasma equilibrium in this configuration, and incrementally increased the total number of particles in the simulation domain to observe plasma behavior as the system transitions to detachment. We observe detachment of the long outer leg, and scaling parameters consistent with the existing theoretical understanding of plasma detachment. In these simulations, we observed up-down and in-out divertor asymmetries, attributed to the imbalance of power fluxes resulting from the disconnected double null configuration and cross-field transport associated with the compact configuration in the main chamber and tight baffling along the divertor legs. The influence of losses to the side walls, characterized here as $Q_{\perp}$, was not initially identified as an important component of the general energy balance in the scrape-off layer energy balance, but appears to be significant in compact devices and long leg geometries [20, 81]. As the detachment process begins with the onset of recombination, our simulations show a saturation of the upstream cross-field transport that coincides with a flattening of the upstream temperature profile that would eliminate the conductive component of the diffusive approximation of the turbulence. Our

work shows that the existing theory and many features of divertor plasma detachment in standard divertors appear to translate to long leg divertor geometries, and that the cross-field transport to the main chamber and divertor leg walls is likely to be a significant concern for compact devices.

Chapter 6 continues the study of perpendicular transport in the same tokamak configuration with the long outer divertor legs. In particular, the focus of this study was to assess whether the impurity radiation would spread out along the long leg instead of localizing to the target or at the X-point, which has been suggested as a way to protect material surfaces and improve core-edge compatibility. We have shown that impurities are distributed along the long leg, and that the perpendicular transport is responsible for the spread of impurity radiation: strong recycling of impurity species against the side wall of the divertor leg introduces a back-and-forth neutralization-ionization "loop" that enables the impurity species to climb up the side walls and radiate in the divertor volume, rather than localizing at the target or core. This behavior is observed for simulations with a nitrogen impurity and in simulations with a neon impurity, indicating that this effect is not species-specific. Nitrogen and neon behave similarly, with neon radiating more in the core, but neither species radiating more than 40% of the total input power, which is unacceptably low for realistic operating conditions. Despite proximity away from the core plasma and low radiation overall, the effective charge at the outer midplane exceeds $Z_{eff} = 4$ for both nitrogen and neon simulations. This is concerning for one of the supposed benefits of the long-leg divertor in this geometric configuration and core compatibility for reactor-relevant conditions, since a similarly high Z_{eff} in the core would not be viable for a reactor.

In general, these results establish an informative basis for design and operational choices for future divertors. While the inverse sheath regime was shown to increase specific electron heat flux to the target with no tangible benefit to the promotion of detachment in the divertor plasma, and introduces the possibility of a bifurcation correlated to the temperature and neutral pressure, it is possible that the inverse sheath may prevent material erosion of the target by limiting bombardment from incoming ion flux, and could be applied in that context. Our studies reveal a strong influence of perpendicular transport on plasma detachment in long-leg regimes with tightly baffled divertor legs. The importance of the impact of the perpendicular transport also significantly affects the impurity species, the distribution of which was shown to be strongly dependent on cross-field impurity recycling effects.

Appendix A

Equations evaluated in the UEDGE code

The full version of the equations (that is, those including contributions from drifts and electric fields) are presented here for consistency with the user manual [68], but the calculations for drifts and electric fields were not included in any of the simulations shown in this work. Typos present in the user manual have been (hopefully) fully corrected here. Attempts have been made to paraphrase and reexplain the existing text corresponding to the equations listed in the user manual, but a distinct lack of lingual dexterity has made the riveting task of describing equations in any kind of novel capacity rather difficult. I apologize in advance for any overt and excessive repetition already present in the existing text upon which this appendix is based, and my greatest regard is owed to the original authors of the UEDGE manual, who achieved the pinnacle of a succinct and robust verbal framework to present their equations that simply could not be elaborated upon. It is truly a triumph.

In the UEDGE code, the coordinate system is such that x corresponds to the poloidal direction and y corresponds to the radial direction. The total velocity is denoted by $\mathbf{u}$, classical components use the symbol v, where these two terms differ by an anomalous diffusive term.

The poloidal ion velocity is:

$$u_{ei_x} = \frac{B_x}{B} v_{ei_\parallel} + v_{x,E} + v_{ei_x,\nabla B} \tag{A.1}$$

where the second term is the $\mathbf{E} \times \mathbf{B}/B^2$ drift and the third term is the sum of the curvature and ∇B

drifts (scaling in tokamaks as qT_i/RB, and $-qT_e/RB$ where q is the ion charge and R is the major radius of the tokamak). The drift terms are written to give a finite divergence of the plasma fluxes, since they also appear inside the divergence terms in the transport equations. The last term is only included in the ion velocity equation, which describes the non-ambipolar anomalous viscous drift that connects the electrostatic potential on neighboring flux surfaces. This term is neglected for electrons because of the small electron gyroradius. This, paired with the difference in scaling of the ∇B, lead to a finite current.

The radial velocity for the electrons and ions is:

$$u_{ei_y} = -\frac{D_a}{n_{ei}}\frac{\partial n_{ei}}{\partial y} + V_a + v_{y,E} + v_{ei_y,\nabla B} + v_{i_y,vis}, \tag{A.2}$$

where D_a and V_a are anomalous transport coefficients characterizing the turbulence-driven transport (assumed ambipolar). The third and fourth terms in Eq. (A.2) describe the radial components of the cross-field drifts.

The fluid variables are described with dynamical equations. The ion continuity equation is

$$\frac{\partial}{\partial t}n_i + \frac{1}{V}\frac{\partial}{\partial x}\left(\frac{V}{h_x}n_i u_{ix}\right) + \frac{1}{V}\frac{\partial}{\partial y}\left(\frac{V}{h_y}n_i u_{iy}\right) = \langle\sigma_i v_e\rangle n_e n_g - \langle\sigma_e v_e\rangle n_e n_i \tag{A.3}$$

The terms $\langle\sigma_i v_e\rangle$ and $\langle\sigma_e v_e\rangle$ are rate coefficients for ionization and recombination, respectively. The terms $h_x \equiv 1/||\nabla x||$ and $h_y \equiv 1/||\nabla y||$ are metric coefficients, and $V = 2\pi R h_x h_y$ is the volume element for toroidal geometry with radius R, which describe the curvature and nonuniformity corresponding to the physical mesh of each cells in the computational domain. For brevity of presentation, these metric coefficients are suppressed in the remaining equations.

The neutral continuity equation (where the subscript "g" denotes the hydrogenic gas atoms) is

$$\frac{\partial}{\partial t}n_g + \frac{\partial}{\partial x}(n_g v_{gx}) + \frac{\partial}{\partial y}(n_g v_{gy}) = -\langle\sigma_i v_e\rangle n_e n_g + \langle\sigma_e v_e\rangle n_e n_i. \tag{A.4}$$

The source term in Eq. (A.4) is the negative of the corresponding ion source.

The ion parallel momentum equation is

$$\frac{\partial}{\partial t}\left(m_i n_i v_{i\parallel}\right)+\frac{\partial}{\partial x}\left(m_i n_i v_{i\parallel}u_{ix}-\eta_{ix}\frac{\partial v_{i\parallel}}{\partial x}\right)+\frac{\partial}{\partial y}\left(m_i n_i v_{i\parallel}u_{iy}-\eta_{iy}\frac{\partial v_{i\parallel}}{\partial y}\right) = \frac{B_x}{B}\left(-\frac{\partial P_p}{\partial x}\right)-m_i n_g \nu_{cx}\left(v_{i\parallel}-v_{g\parallel}\right) \tag{A.5}$$

where $P_p = P_e + P_i$, $\eta_{ix} = (B_x/B)^2\eta_\parallel$ is the classical viscosity, $\eta_{iy} = m_i n \Upsilon_{a,\parallel}$ is the anomalous viscosity. The electron momentum equation is assume to ahve no inertia and has been used to eliminate the parallel electric field and the ion-electron friction term, which are replaced by the P_e component of P_p. The hydrogenic species neutral density is n_g, $\eta_{cx} = n_i\langle\sigma_{cx}v_i$ is the ion-neutral charge exchange frequency for the hydrogenic species, and $u_{g,\parallel}$ is the (atomic) neutral hydrogen parallel velocity. The classical viscosities and thermal conductivities are flux-limited, as discussed in Section 3.2.1, which prevents unphysically large values in regions with long mean-free paths. The classical terms are obtained from [38].

The corresponding equation for the parallel momentum of the hydrogenic neutral gas species is

$$\frac{\partial}{\partial t}\left(m_g n_g v_{g\parallel}\right)+\frac{\partial}{\partial x}\left(m_g n_g v_{g\parallel}u_{gx}-\eta_{gx}\frac{\partial v_{g\parallel}}{\partial x}\right)+\frac{\partial}{\partial y}\left(m_g n_g v_{g\parallel}u_{gy}-\eta_{gy}\frac{\partial v_{g\parallel}}{\partial y}\right) = \frac{B_x}{B}\left(-\frac{\partial P_g}{\partial x}\right)+m_i n_g \nu_{cx}\left(v_{i\parallel}-v_{g\parallel}\right), \tag{A.6}$$

where the η_{gx} and η_{gy} terms are the viscosities determined by charge-exchange collisions. These viscosities, and the corresponding neutral thermal diffusivities described below, are given by $D_g = T_g/(m_g\nu_{cx})$, where T_g is the neutral gas temperature, and flux-limited to prevent unphysically large values.

Similar to the formulation for ions, the neutral velocity has two main components: the parallel velocity (as just described) and the other from the charge-exchange and ionization processes in the directions perpendicular to **B**, or

$$\mathbf{v}_{\perp g} = -\frac{\nabla_{\perp}(n_g T_n)}{m_i n_g (n_i \langle \sigma c x v_i \rangle + n_e \langle \sigma_i v_e \rangle)}, \tag{A.7}$$

such that the total neutral velocities are

$$u_{gx} = \frac{B_x}{B} v_{i\|} - \frac{B_z}{B} v_{gw}, \tag{A.8}$$

where B_z is the total toroidal component of the B-field, and v_{gw} is the perpendicular component of $\mathbf{v}_{\perp g}$ in the binormal direction $(\hat{\mathbf{i}}_{\|} \times \hat{\mathbf{i}}_y)$. For the radial ion velocity,

$$u_{gy} = \hat{\mathbf{i}}_y \cdot \mathbf{v}_{\perp g}. \tag{A.9}$$

The electron energy equation is

$$\begin{aligned} \frac{\partial}{\partial t}\left(\frac{3}{2} n_e T_e\right) + \frac{\partial}{\partial x}\left[C_{ex} n_e u_{ex} T_e - \kappa_{ex}\frac{\partial T_e}{\partial x} - 0.71 n_e T_e \frac{B_x}{B}\frac{J_{\|}}{e n_e}\right] + \frac{\partial}{\partial y}\left(C_{ey} n_e u_{ey} T_e - \kappa_{ey}\frac{\partial T_e}{\partial y}\right) \\ = \left[u_{ix}\frac{\partial P_e}{\partial x} - u_{iy}\frac{\partial P_i}{\partial y} - u_{iw}\frac{B_x}{B}\frac{\partial P_p}{\partial x}\right] + \mathbf{E}\cdot\mathbf{J} - K_q(T_e - T_i) + S_{Ee} \end{aligned} \tag{A.10}$$

Here, the poloidal heat conductivity is classical, with $\kappa_{ex} = (B_x/B)^2 \kappa_{\|}$, radial heat conductivity is anomalous, as $\kappa_{ey} = n\chi_e$, and K_q is the collisional energy exchange coefficient. The velocity u_{iw} is the velocity in the direction binormal to $\mathbf{B}$ and the radial direction $\left(\hat{\mathbf{i}}_{\|} \times \hat{\mathbf{i}}_y\right)$, which is only used when cross-field drifts are included. Typical values for convection coefficients $C_{ex,ey}$ are $5/2$ or $3/2$.

The ion energy equation below has an implied sum over the ion and neutral species with $T_g = T_i$.

$$\frac{\partial}{\partial t}\left(\frac{3}{2}n_iT_i\right)+\frac{\partial}{\partial x}\left[C_{ix}n_iu_{ix}T_i-\kappa_{jx}\frac{\partial T_i}{\partial x}\right]+\frac{\partial}{\partial y}\left(C_{iy}n_iu_{iy}T_i-\kappa_{jy}\frac{\partial T_i}{\partial y}\right)=[\mathbf{u}_i\cdot\nabla P_i]$$
$$+\eta_{ix}\left(\frac{\partial v_{ij\|}}{\partial x}\right)^2+\eta_{iy}\left(\frac{\partial v_{i\|}}{\partial y}\right)^2+K_{qj}\left(T_e-T_i\right)+\frac{1}{2}m_iv_{i\|}^2n_i\nu_{iz}+S_{Ej}. \tag{A.11}$$

The electron poloidal thermal conduction (and viscosity) coefficients are classical and the radial coefficients are anomalous; the same typical values for convection coefficients $C_{ix,iy}=5/2$ or $3/2$ are used.

The equation for the potential is obtained by subtracting the ion and electron continuity equations, and assuming quasineutrality, such that $n_i=n_e$:

$$\nabla\cdot\mathbf{J}(\phi)=\frac{\partial}{\partial x}\left(J_x\right)+\frac{\partial}{\partial y}\left(J_y\right)=0. \tag{A.12}$$

In this case, $\mathbf{J}$ means the currents, excluding the magnetization current, since the divergence of the magnetization current is automatically zero because it is the curl of a vector. This means that the remaining current components are

$$\mathbf{J}=\left[ne\left(\mathbf{v}_{i,\nabla B}-\mathbf{v}_{e,\nabla B}\right)\cdot\hat{\mathbf{i}}_x+J_{\|}\frac{B_x}{B}\right]\hat{\mathbf{i}}_x+ne\left(v_{i,y1}-v_{e,y1}\right)\hat{\mathbf{i}}_y. \tag{A.13}$$

Note that the terms arising from the $\mathbf{v}_{\nabla B}$-drift do not explicitly depend on ϕ, so they act as source terms in Eq. (A.12). The expression for the parallel current, $J_{\|}$, comes from the parallel momentum equation for electrons with $m_e\to 0$, yielding

$$J_{\|}=\frac{en}{0.51m_e\nu_e}\frac{B_x}{B}\left(\frac{1}{n}\frac{\partial P_e}{\partial x}-e\frac{\partial\phi}{\partial x}+0.71\frac{\partial T_e}{\partial x}\right), \tag{A.14}$$

where ν_e is the electron collision frequency, and the numerical coefficients are described in [38]. Note that the expression for the radial current is different from that in [37].

A basic model for the impurity parallel velocity is obtained from the ion parallel momentum equation, but neglecting inertia and viscosity terms,

$$\begin{aligned}\frac{\partial}{\partial t}\left(m_z n_z v_{z\|}\right)+\frac{\partial}{\partial x}\left(m_z n_z v_{i\|} u_{zx}-\eta_{zx}\frac{\partial v_{z\|}}{\partial x}\right)+\frac{\partial}{\partial y}\left(m_z n_z v_{z\|} u_{zy}-\eta_{zy}\frac{\partial v_{z\|}}{\partial y}\right)\\ =\left(\frac{B_x}{B}\right)\left(-\frac{\partial P_z}{\partial x}+\alpha_z n_z\frac{\partial T_e}{\partial x}+\beta_z n_z\frac{\partial T_i}{\partial x}-Z_e n_z\frac{\partial \Phi}{\partial x}\right)\\ -\left(u_{\|z}-u_{\|h}\right)m_h n_h \nu_{hz}.\end{aligned} \tag{A.15}$$

Note that the B_x/B converts the poloidal gradients into parallel gradients, i.e, $(B_x/B)\,\partial/\partial x=\partial/\partial s$, where s is the parallel distance along a field line. The thermal force coefficients come from [137] and [138]:

$$\alpha_z = 2.2Z^2\left(1+0.52Z_{\text{eff}}\right)\left[\left(1+2.65Z_0\right)\left(1+0.285Z_{\text{eff}}\right)Z_{\text{eff}}\right], \tag{A.16}$$

$$\begin{aligned}\beta_z =& 1.56\left(1+\sqrt{2}Z_0\right)\left(1+0.52Z_0\right)\left(1+\sqrt{2}Z_0\right)\left(1+0.52Z_0\right)Z^2\left(1+\sqrt{2}Z_0\right)\left(1+0.52Z_0\right)\\ &\left[\left(1+2.65Z_0\right)\left(1+0.285Z_0\right)\left\{Z_0+\left(\left(m_h+m_z\right)/2m_z\right)^{1/2}\right\}\right]\\ &+0.6\left(Z^2 n_{tz}/n_h Z_0-1\right),\end{aligned} \tag{A.17}$$

where $Z_0 = n_e Z_{\text{eff}}/n_h - 1, Z$ is the charge of the impurity ion, the h subscript refers to the hydrogen ion, and n_{tz} is the total impurity ion density summed over all charge states (with a common ion temperature).

A more complete option is to include the individual impurity ion inertial terms Eq. (A.15); this is achieved in UEDGE my setting an input variable to the total number of full ion momentum equations desired (generally one each for hydrogen ions and neutrals, plus the number of impurity charge states, excluding the neutral impurity).

Appendix B

Equations evaluated in the SOLPS code

The SOLPS code suite is a package consisting of the B2 fluid code for the plasma and the EIRENE 3D Monte Carlo code for neutral particles. Underlying equations of the B2 Code (taken from [139] and [61]) are described, and the reactions from the EIRENE package are listed.

B.1 B2 Equations

In Eqs. (B.1) to (B.5), the subscript x denotes the transport coefficients in the parallel direction, and the subscript y stands for the perpendicular direction. The terms denoted with **u** characterize the parallel velocity, while the terms associated with **v** characterize the radial ion velocity. Terms associated with g are geometric coefficients that characterize the shape of the mesh in the computational domain.

B.1.1 Ion equations

Eqs. (B.1) to (B.3) are taken for each ion species α.

B.1.1.1 Continuity equation

$$\frac{\partial n_\alpha}{\partial t} + \frac{1}{\sqrt{g}}\frac{\partial}{\partial x}\left(\frac{\sqrt{g}}{h_x} n_\alpha u_\alpha\right) + \frac{1}{\sqrt{g}}\frac{\partial}{\partial y}\left(\frac{\sqrt{g}}{h_y} n_\alpha v_\alpha\right) = S_n^\alpha, \tag{B.1}$$

where S_n is the sources of particles due to interaction with neutrals.

B.1.1.2 Parallel momentum balance

$$\begin{aligned}
&\frac{\partial}{\partial t}\left(m_\alpha n_\alpha u_{\parallel\alpha}\right)+\frac{1}{\sqrt{g}}\frac{\partial}{\partial x}\left(\frac{\sqrt{g}}{h_x}m_\alpha n_\alpha u_\alpha u_{\parallel\alpha}-\frac{\sqrt{g}}{h_x^2}\eta_x^\alpha\frac{\partial u_{\parallel\alpha}}{\partial x}\right)+\\
&\frac{1}{\sqrt{g}}\frac{\partial}{\partial y}\left(\frac{\sqrt{g}}{h_y}m_\alpha n_\alpha v_\alpha u_{\parallel\alpha}-\frac{\sqrt{g}}{h_y^2}\eta_y^\alpha\frac{\partial u_{\parallel\alpha}}{\partial y}\right)\\
&=\frac{B_\theta}{B}\frac{1}{h_x}\left[-\frac{\partial p_\alpha}{\partial x}-\frac{Z_\alpha n_\alpha}{n_e}\frac{\partial p_e}{\partial x}+c_e\left(\frac{Z_\alpha}{Z_{eff}}-1\right)Z_\alpha n_\alpha\frac{\partial T_e}{\partial x}+c_i\left(\frac{Z_\alpha}{Z_{eff}}-1\right)Z_\alpha n_\alpha\frac{\partial T_i}{\partial x}\right]+\\
&\sum_\beta F_{\alpha\beta}+S^\alpha_{mu_\parallel},
\end{aligned}\tag{B.2}$$

where $S_{mu_\parallel}$ is the sources of parallel momentum due to interaction with neutrals, c_i and c_e are the coefficients of the thermal force (which can be important for impurities), $F_{\alpha\beta}$ is the friction force between species α and β, and Z_{eff} is the effective charge:

$$Z_{eff}=\frac{\sum_\alpha Z_\alpha^2 n_\alpha}{\sum_\alpha Z_\alpha n_\alpha}.$$

B.1.1.3 Ion energy balance

$$\begin{aligned}
&\frac{\partial}{\partial t}\left(\frac{3}{2}n_i T_i+\sum_\alpha\frac{1}{2}m_\alpha n_\alpha u_{\parallel\alpha}^2\right)+\\
&\frac{1}{\sqrt{g}}\frac{\partial}{\partial x}\left(\frac{\sqrt{g}}{h_x}\left[\sum_\alpha\frac{5}{2}n_\alpha u_\alpha T_i+\sum_\alpha\frac{1}{2}m_\alpha n_\alpha u_\alpha u_{\parallel\alpha}^2\right]-\frac{\sqrt{g}}{h_x^2}\left[k_x^i\frac{\partial T_i}{\partial x}+\sum_\alpha\frac{1}{2}\nu_x^\alpha\frac{\partial u_{\parallel\alpha}^2}{\partial x}\right]\right)+\\
&\frac{1}{\sqrt{g}}\frac{\partial}{\partial y}\left(\frac{\sqrt{g}}{h_y}\left[\sum_\alpha\frac{5}{2}n_\alpha u_\alpha T_i+\sum_\alpha\frac{1}{2}m_\alpha n_\alpha v_\alpha u_{\parallel\alpha}^2\right]-\frac{\sqrt{g}}{h_y^2}\left[k_y^i\frac{\partial T_i}{\partial y}+\sum_\alpha\frac{1}{2}\nu_y^\alpha\frac{\partial u_{\parallel\alpha}^2}{\partial y}\right]\right)=\\
&-\frac{u_\alpha}{h_x}\frac{\partial p_e}{\partial x}-\frac{v_\alpha}{h_y}\frac{\partial p_e}{\partial y}+k_{ei}\left(T_e-T_i\right)+S_E^i,
\end{aligned}\tag{B.3}$$

where S_E^i is the source of ion energy due to interaction with neutrals, $p_e=n_eT_e$, it is assumed that all ions have the same temperature T_i, and $n_i=\sum_\alpha n_\alpha$.

B.1.1.4 Radial transport

Radial transport is determined using a diffusion equation, where D_n and D_p are the diffusion coefficients:

$$v_\alpha = -\frac{D_n^\alpha}{h_y}\frac{\partial}{\partial y}(\ln n_\alpha) - \frac{D_p^\alpha}{h_y}\frac{\partial}{\partial y}(\ln p_\alpha) \tag{B.4}$$

B.1.2 Electrons

B.1.2.1 Density and velocity

The electron density and average velocity are found from the conditions of quasi-neutrality and ambipolarity:

$$n_e = \sum_\alpha Z_\alpha n_\alpha, \quad u_e = \frac{1}{n_e}\sum_\alpha Z_\alpha n_\alpha u_\alpha, \quad v_e = \frac{1}{n_e}\sum_\alpha Z_\alpha n_\alpha v_\alpha. \tag{B.5}$$

B.1.2.2 Electron energy balance

$$\begin{gathered}\frac{\partial}{\partial t}\left(\frac{3}{2}n_e T_e\right) + \frac{1}{\sqrt{g}}\frac{\partial}{\partial x}\left(\frac{\sqrt{g}}{h_x}\frac{5}{2}n_e u_e T_e - \frac{\sqrt{g}}{h_x^2}k_x^e\frac{\partial T_e}{\partial x}\right) + \\ \frac{1}{\sqrt{g}}\frac{\partial}{\partial y}\left(\frac{\sqrt{g}}{h_y}\frac{5}{2}n_e u_e T_e - \frac{\sqrt{g}}{h_y^2}k_y^e\frac{\partial T_e}{\partial y}\right) = \frac{u_\alpha}{h_x}\frac{\partial p_e}{\partial x} + \frac{v_\alpha}{h_y}\frac{\partial p_e}{\partial y} - k_{ei}(T_e - T_i) + S_E^e,\end{gathered} \tag{B.6}$$

where S_E^e is the source of electron energy due to interaction with neutrals.

B.1.3 Transport coefficients

Transport coefficients are expressed in terms of two basic collision times. The collision time for electron-ion collisions is

$$\tau_e = \frac{3\sqrt{m_e}T_e^{3/2}}{4\sqrt{\pi}n_i Z e^4 \ln\Lambda} = 3.44\cdot 10^{11}\frac{T_e^{3/2}}{Z n_e \ln\Lambda}, \tag{B.7}$$

while the collision time for ion-ion collisions is

$$\tau_i = \frac{3\sqrt{m_p m_i} T_i^{3/2}}{4\sqrt{\pi} Z^4 n_i \ln\Lambda} = 2.09 \cdot 10^{13} \frac{T_i^{3/2}\sqrt{m_i}}{Z^4 n_i \ln\Lambda}. \tag{B.8}$$

All the formulas with reduced numerical coefficients throughout this subsection yield the result (by default) in SI units. They are given for temperatures in eV and densities in^{-3}. The ion mass m_i is expressed in proton masses m_p(amu). Initial expressions taken from [140] use CGS units. The Coulomb logarithm $\ln\Lambda$ is calculated using the approximation:

$$\ln\Lambda = 17.38 - 0.5\ln\frac{n_e}{10^{20}} + 1.5\ln\frac{T_e}{1000} \tag{B.9}$$

The typical value is $5-15$.

Spitzer-Härm [141] thermal conductivity for electrons:

$$k_\parallel^e = 3.2\frac{n_e T_e \tau_e}{m_e} = \frac{2.4}{\sqrt{\pi m_e} e^4} \frac{T_e^{5/2}}{Z\ln\Lambda} = 3.07 \cdot 10^4 \frac{T_e^{5/2}}{Z\ln\Lambda} \tag{B.10}$$

Ion thermal conductivity:

$$k_\parallel^i = 3.9\frac{n_i T_i \tau_i}{m_i} = \frac{10.7}{4\sqrt{\pi m_p} e^4} \frac{T_i^{5/2}}{\sqrt{m_i} Z^4 \ln\Lambda} = 1.25 \cdot 10^3 \frac{T_i^{5/2}}{\sqrt{m_i Z^4 \ln\Lambda}} \tag{B.11}$$

Eqs. (B.10) and (B.11), with numerical coefficients, give the result in $\mathrm{W}/(\mathrm{m}\cdot\mathrm{eV})$. For a hydrogen ion, $k_\parallel^i$ is a factor ≈ 30 smaller than $k_\parallel^e$.

The Braginskii formula for parallel viscosity is:

$$\eta_\parallel = 0.96 n_i T_i \tau_i = \frac{0.406\sqrt{m_p}}{e^4} \frac{\sqrt{m_i} T_i^{5/2}}{Z^4 \ln\Lambda} = 3.2 \cdot 10^{-6} \frac{T_i^{5/2}\sqrt{m_i}}{Z^4 \ln\Lambda} \tag{B.12}$$

This is the dynamic viscosity, expressed in $\mathrm{kg}/\mathrm{m}^3\cdot\mathrm{s}(\mathrm{P}\cdot\mathrm{s})$.

Eqs. (B.10) to (B.12) are generalized for the case of multi-species plasma according to Braams:

$$k_{\parallel}^{e} = 3.2\frac{n_e T_e \tau_e}{m_e} = \frac{2.4}{\sqrt{\pi m_e} e^4}\frac{T_e^{5/2}}{Z_{eff}^2 \ln\Lambda} \tag{B.13}$$

$$k_{\parallel}^{i} = \frac{10.7}{4\sqrt{\pi m_p} e^4}\sum_{\alpha}\frac{Z_{\alpha}^{-2} n_{\alpha}}{\sum_{\beta}\left(Z_{\beta}^2 n_{\beta}\sqrt{\frac{2m_{\alpha}m_{\beta}}{m_{\alpha}+m_{\beta}}}\right)}\frac{T_i^{5/2}}{\ln\Lambda} \tag{B.14}$$

$$\eta_{\parallel}^{\alpha} = \frac{0.406\sqrt{m_p}}{e^4}\frac{Z_{\alpha}^{-2} n_{\alpha}}{\sum_{\beta}\left(n_{\beta} Z_{\beta}^2\sqrt{\frac{2}{m_{\alpha}+m_{\beta}}}\right)}\frac{T_i^{5/2}}{\ln\Lambda} \tag{B.15}$$

Eqs. (B.13) to (B.15) represent a simplification of the complete multi-species transport theory. They are valid for the case if one species dominates.

The energy exchange coefficient k_{ei} generalized for the multi-species case:

$$k_{ei} = \frac{4\sqrt{2\pi m_e} e^4}{m_p}\left(\sum_{\alpha}\frac{Z_{\alpha}^2 n_{\alpha}}{m_{\alpha}}\right)\frac{n_e \ln\Lambda}{T_e^{3/2}} = 4.75\cdot 10^{-9}\left(\sum_{\alpha}\frac{Z_{\alpha}^2 n_{\alpha}}{m_{\alpha}}\right)\frac{n_e \ln\Lambda}{T_e^{3/2}} \tag{B.16}$$

The effective Mean Free Path (MFP) of electrons and ions derived from Eq. (B.7) and Eq. (B.8):

$$MFP_e = v_T^e \cdot \tau_e = 2.5\cdot 10^{17}\frac{T_e^{3/2}}{Z^2 n_e \ln\Lambda}, \quad MFP_i = v_T^i \cdot \tau_i = 2.05\cdot 10^{17}\frac{T_i^{3/2}}{Z^4 n_i \ln\Lambda} \tag{B.17}$$

Here $v_T^e = \sqrt{\frac{3T_e}{m_e}}$ and $v_T^i = \sqrt{\frac{T_i}{m_i}}$ are the estimates if the electron and ion thermal velocities (for approximately $n_e = 10^{19}$ m^{-3} and $T_e = 100$eV, MFP$_e \approx$ MFP$_i \approx 18$ m).

Flux limits:

$$k_{\parallel,lim}^{e} = k_{\parallel SH}^{e}\left[1 + \frac{k_{\parallel SH}^{e}\frac{\partial T_e}{\partial x}}{F_e n_e T_e\sqrt{\frac{T_e}{m_e}}}\right]^{-1}, \eta_{\parallel,lim}^{\alpha} = \eta_{\parallel}^{\alpha}\left[1 + \frac{\eta_{\parallel}^{\alpha}\frac{\partial u_{\parallel\alpha}}{\partial x}}{F_{mom} p_{\alpha}}\right]^{-1} \tag{B.18}$$

Here, $k^e_{\parallel SH}$ is the Spitzer-Härm coefficient given by Eq. (B.13) and $\eta^\alpha_\parallel$ is calculated by Eq. (B.15). Default values of the flux limiting factors F_e and F_{mom} are 0.2 and 0.5, respectively.

B.2 Eirene Reactions

The references are given to the records in the EIRENE databases HYDHEL [43] and AMJUEL [42] which can be found on www.eirene.de. Neutral-neutral interactions are not considered here.

Reaction	**Type**	**Database**	**Set**	**Number**
$p + H(1s) \longrightarrow H(1s) + p$	Charge-exchange	HYDHEL	H.1	3.1.8
$p + H(1s) \longrightarrow H(1s) + p$	Charge-exchange	HYDHEL	H.3	3.1.8
$e + H \longrightarrow 2e + H^+$	Ionization	AMJUEL	H.4	2.1.5
$e + H \longrightarrow H^+ + 2e$	Ionization	AMJUEL	H.10	2.1.5
$p + Ne \longrightarrow p + Ne$	Elastic scattering (Ne)	AMJUEL	H.1	0.5T
$p + Ne \longrightarrow p + Ne$	Elastic scattering (Ne)	AMJUEL	H.3	0.5T
$e + Ne \longrightarrow e + Ne^+ + e$	Ionization (Ne)	AMJUEL	H.2	2.10B0
$e + N \longrightarrow e + N^+ + e$	Ionization (N)	AMJUEL	H.2	2.7B0
$e + H_2(X\,{}^1\Sigma_g{}^+) \longrightarrow$ $e + H_2(b\,{}^3\Sigma_u{}^+, a\,{}^3\Sigma_g{}^+, c\,{}^3\Pi_u) \longrightarrow$ $e + H(1s) + H(1s)$	Dissociation	HYDHEL	H.2	2.2.5
$e + H_2(X\,{}^1\Sigma_g{}^+) \longrightarrow$ $e + H_2{}^+(v) + e$	Ionization	HYDHEL	H.2	2.2.9
$e + H_2(X\,{}^1\Sigma_g{}^+) \longrightarrow$ $e + [H_2(\Sigma_g, \Sigma_u)^+ e] \longrightarrow$ $e + H^+ H(1s)^+ e$	Dissociation	HYDHEL	H.2	2.2.10
$H^+ + e \longrightarrow H(1s)$	Rad. recombination	AMJUEL	H.4	2.1.8
$H^+ + e \longrightarrow H$	Rad. recombination	AMJUEL	H.10	2.1.8
$p + H_2 \longrightarrow p + H_2$	Elastic scattering	AMJUEL	H.0	0.3T
$p + H_2 \longrightarrow p + H_2$	Elastic scattering	AMJUEL	H.1	0.3T
$p + H_2 \longrightarrow p + H_2$	Elastic scattering	AMJUEL	H.3	0.3T
$e + H_2{}^+ \longrightarrow 2e + H^+ + H^+$	Diss. ionization	AMJUEL	H.4	2.2.11
$e + H_2{}^+ \longrightarrow e + H + H^+$	Dissociation	AMJUEL	H.4	2.2.12
$e + H_2{}^+ \longrightarrow H + H$	Diss. recombination	AMJUEL	H.4	2.2.14
$e + H_2{}^+(v) \longrightarrow$ $H(1s) + H^*(n)(v = 0-9, n \geq 2)$	Diss. recombination	AMJUEL	H.8	2.2.14

Bibliography

(1) Masline, R.; Bykov, I.; Moyer, R. A.; Orlov, D. M.; Wingen, A.; Guterl, J.; Rudakov, D. L.; Wampler, W. R.; Wang, H. Q.; Watkins, J. Misalignment of magnetic field in DIII-D assessed by post-mortem analysis of divertor targets. *Nuclear Fusion* **2022**, DOI: 10.1088/1741-4326/ac9cf1.

(2) Luxon, J. A design retrospective of the DIII-D tokamak. *Nuclear Fusion* **2002**, *42*, 614–633.

(3) Campanell, M. D. Negative plasma potential relative to electron-emitting surfaces. *Phys. Rev. E.* **2013**, *88*, 033103.

(4) Campanell, M. D.; Umansky, M. V. Strongly Emitting Surfaces Unable to Float below Plasma Potential. *Physical Review Letters* **2016**, *116*, 1–5.

(5) Campanell, M. D.; Johnson, G. R. Thermionic Cooling of the Target Plasma to a Sub-eV Temperature. *Physical Review Letters* **2019**, *122*, 1–5.

(6) Coda, S.; Agostini, M.; Albanese, R.; Alberti, S.; Alessi, E.; Allan, S.; Allcock, J.; Ambrosino, R.; Anand, H.; Andrèbe, Y., et al. Physics research on the TCV tokamak facility: from conventional to alternative scenarios and beyond. *Nuclear Fusion* **2019**, *59*, 112023.

(7) Havlíčková, E.; Wischmeier, M.; Lipschultz, B.; Fishpool, G. The effect of the Super-X divertor of MAST Upgrade on impurity radiation as modelled by SOLPS. *Journal of Nuclear Materials* **2015**, *463*, 1209–1213.

(8) Umansky, M. V.; LaBombard, B.; Brunner, D.; Rensink, M. E.; Rognlien, T. D.; Terry, J. L.; Whyte, D. G. Attainment of a stable, fully detached plasma state in innovative divertor configurations. *Physics of Plasmas* **2017**, *24*, DOI: 10.1063/1.4979193.

(9) Krasheninnikov, S. I.; Rensink, M.; Rognlien, T. D.; Kukushkin, A. S.; Goetz, J. A.; LaBombard, B.; Lipschultz, B.; Terry, J. L.; Umansky, M. Stability of the detachment front in a tokamak divertor. *Journal of Nuclear Materials* **1999**, *266*, 251–257.

(10) Reimold, F.; Wischmeier, M.; Bernert, M.; Potzel, S.; Kallenbach, A.; Müller, H.; Sieglin, B.; and, U. S. Divertor studies in nitrogen induced completely detached H-modes in full tungsten ASDEX Upgrade. *Nuclear Fusion* **2015**, *55*, 033004.

(11) Bernert, M.; Wischmeier, M.; Huber, A.; Reimold, F.; Lipschultz, B.; Lowry, C.; Brezinsek, S.; Dux, R.; Eich, T.; Kallenbach, A.; Lebschy, A.; Maggi, C.; McDermott, R.; Pütterich, T.; Wiesen, S. Power exhaust by SOL and pedestal radiation at ASDEX Upgrade and JET. *Nuclear Materials and Energy* **2017**, *12*, Proceedings of the 22nd International Conference on Plasma Surface Interactions 2016, 22nd PSI, 111–118.

(12) Krasheninnikov, S. Lecture notes in MAE 217A: Introduction to Gas Discharge Plasma Physics, Fall 2018.

(13) Krasheninnikov, S. I.; Smolyakov, A.; Kukushkin, A., *On the Edge of Magnetic Fusion Devices*, 1st ed.; Springer: Cham, Switzerland, 2020.

(14) Tonks, L.; Langmuir, I. A General Theory of the Plasma of an Arc. *Phys. Rev.* **1929**, *34*, 876–972.

(15) Hobbs, G. D.; Wesson, J. A. Heat flow through a Langmuir sheath in the presence of electron emission. *Plasma Physics* **1967**, *9*, 85–87.

(16) Krasheninnikov, S.; Kukushkin, A. Physics of ultimate detachment of a tokamak divertor plasma. *J. Plasma Physics* **2017**, *83*, 1–77.

(17) ITER Physics Expert Group on Divertor; ITER Physics Expert Group on Divertor Modelling and Database; ITER Physics Basis Editors Related content Chapter 4 : Power and particle control. *Nuclear Fusion* **1999**, *39*, 2391–2469.

(18) Pigarov, A. Y. Radiative detached divertor with acceptable separatrix Z-eff. *Physics of Plasmas* **2017**, *24*, 102521.

(19) Loarte, A; Monk, R.; Martín-Solís, J.; Campbell, D.; Chankin, A.; Clement, S; Davies, S.; Ehrenberg, J; Erents, S.; Guo, H.; Harbour, P.; Horton, L.; Ingesson, L.; Jäckel, H; Lingertat, J; Lowry, C.; Maggi, C.; Matthews, G.; McCormick, K; O'Brien, D.; Reichle, R; Saibene, G; Smith, R.; Stamp, M.; Stork, D; Vlases, G. Plasma detachment in JET Mark Idivertor experiments. *Nuclear Fusion* **1998**, *38*, 331–371.

(20) Krasheninnikov, S. I.; Pigarov, A. Y.; Sigmar, D. J. Plasma Recombination and Divertor Detachment. *Contributions to Plasma Physics* **1996**, *36*, 314–318.

(21) Janev, R.; Post, D.; Langer, W.; Evans, K.; Heifetz, D.; Weisheit, J. Survey of atomic processes in edge plasmas. *Journal of Nuclear Materials* **1984**, *121*, 10–16.

(22) Reimerdes, H.; Ambrosino, R.; Innocente, P.; Castaldo, A.; Chmielewski, P.; Di Gironimo, G.; Merriman, S.; Pericoli-Ridolfini, V.; Aho-Mantilla, L.; Albanese, R.; Bufferand, H.; Calabro, G.; Ciraolo, G.; Coster, D.; Fedorczak, N.; Ha, S.; Kembleton, R.; Lackner, K.; Loschiavo, V. P.; Lunt, T.; Marzullo, D.; Maurizio, R.; Militello, F.; Ramogida, G.; Subba, F.; Varoutis, S.; Zagórski, R.; Zohm, H. Assessment of alternative divertor configurations as an exhaust solution for DEMO. *Nuclear Fusion* **2020**, *60*, 1–8.

(23) LaBombard, B.; Marmar, E.; Irby, J.; Terry, J. L.; Vieira, R.; Wallace, G.; Whyte, D. G.; Wolfe, S.; Wukitch, S.; Baek, S.; Beck, W.; Bonoli, P.; Brunner, D.; Doody, J.; Ellis, R.; Ernst, D.; Fiore, C.; Freidberg, J. P.; Golfinopoulos, T.; Granetz, R.; Greenwald, M.; Hartwig, Z. S.; Hubbard, A.; Hughes, J. W.; Hutchinson, I. H.; Kessel, C.; Kotschenreuther, M.; Leccacorvi, R.; Lin, Y.; Lipschultz, B.; Mahajan, S.; Minervini, J.; Mumgaard, R.; Nygren, R.; Parker, R.; Poli, F.; Porkolab, M.; Reinke, M. L.; Rice, J.; Rognlien, T.; Rowan, W.; Shiraiwa, S.; Terry, D.; Theiler, C.; Titus, P.; Umansky, M.; Valanju, P.; Walk, J.; White, A.; Wilson, J. R.; Wright, G.; Zweben, S. J. ADX: A high field, high power density, advanced divertor and RF tokamak. *Nuclear Fusion* **2015**, *55*, DOI: 10.1088/0029-5515/55/5/053020.

(24) Kotschenreuther, M.; Valanju, P.; Covele, B.; Mahajan, S. Magnetic geometry and physics of advanced divertors: The X-divertor and the snowflake. *Physics of Plasmas* **2013**, *20*, DOI: 10.1063/1.4824735.

(25) Soukhanovskii, V. A. A review of radiative detachment studies in tokamak advanced magnetic divertor configurations. *Plasma Physics and Controlled Fusion* **2017**, *59*, 064005.

(26) Valanju, P. M.; Kotschenreuther, M.; Mahajan, S. M.; Canik, J. Super-X divertors and high power density fusion devices. *Physics of Plasmas* **2009**, *16*, DOI: 10.1063/1.3110984.

(27) Ryutov, D. D. Geometrical properties of a "snowflake" divertor. *Physics of Plasmas* **2007**, *14*, DOI: 10.1063/1.2738399.

(28) Ryutov, D. D.; Soukhanovskii, V. A. The snowflake divertor. *Physics of Plasmas* **2015**, *22*, DOI: 10.1063/1.4935115.

(29) Gorno, S; Colandrea, C; Février, O; Reimerdes, H; Theiler, C; Duval, B. P.; Lunt, T; Raj, H; Sheikh, U. A.; Simons, L; Thornton, A; Team, T. T.; Team, T. E. M. Power exhaust and core-divertor compatibility of the baffled snowflake divertor in TCV. *Plasma Physics and Controlled Fusion* **2023**, *65*, 035004.

(30) Ryutov, D. D.; Cohen, R. H.; Rognlien, T. D.; Soukhanovskii, V. A.; Umansky, M. V. Comment on "magnetic geometry and physics of advanced divertors: The X-divertor and the snowflake" [Phys. Plasmas 20, 102507 (2013)]. *Physics of Plasmas* **2014**, *21*, DOI: 10.1063/1.4873404.

(31) Soukhanovskii, V. A.; Allen, S. L.; Fenstermacher, M. E.; Lasnier, C. J.; Makowski, M. A.; McLean, A. G.; Meier, E. T.; Meyer, W. H.; Rognlien, T. D.; Ryutov, D. D.; Scotti, F.; Kolemen, E.; Bell, R. E.; Diallo, A.; Gerhardt, S.; Kaita, R.; Kaye, S.; Leblanc, B. P.; Maingi, R.; Menard, J. E.; Podesta, M.; Roquemore, A. L.; Groebner, R. J.; Hyatt, A. W.; Leonard, A. W.; Osborne, T. H.; Petrie, T. W.; Ahn, J. W.; Raman, R.; Watkins, J. G. Developing snowflake divertor physics basis in the DIII-D, NSTX and NSTX-U tokamaks aimed at the divertor power exhaust solution. **2016**, DOI: 10.1109/SOFE.2015.7482263.

(32) Wigram, M. R. K. Modelling tokamak power exhaust and scrape-off-layer thermal transport in high-power fusion devices, Ph.D. Thesis, University of York, 2019.

(33) Lipschultz, B.; LaBombard, B.; Marmar, E.; Pickrell, M.; Terry, J.; Watterson, R.; Wolfe, S. Marfe: an edge plasma phenomenon. *Nuclear Fusion* **1984**, *24*, 977.

(34) LaBombard, B. X-point Target Divertor Concept, Contributed Oral, 55th Annual Meeting of the APS Division of Plasma Physics, Denver, Colorado, 2013.

(35) Kukushkin, A. S.; Pacher, H. D.; Kotov, V.; Pacher, G. W.; Reiter, D. Finalizing the ITER divertor design: The key role of SOLPS modeling. *Fusion Engineering and Design* **2011**, *86*, 2865–2873.

(36) Schneider, R.; Runov, A. Challenges in plasma edge fluid modelling. *Plasma Physics and Controlled Fusion* **2007**, *49*, DOI: 10.1088/0741-3335/49/7/S06.

(37) Braams, B. et al. A multi-fluid code for simulation of the edge plasma in tokamaks. *NET Report* **1987**, *68*.

(38) Braginskii, S. Transport processes in a plasma. *Reviews of Plasma Physics* **1965**, *1*, ed. by Leontovich, M., 205.

(39) Hinton, F., Collisional transport in plasma In *Handbook of Plasma Physics*, Galeev, A., Sudan, R., Eds.; North-Holland: Netherlands, 1983; Chapter 1, pp 147–197.

(40) Kukushkin, A. Spontaneous Break of up–down Symmetry in a Symmetric Double-Null Divertor Configuration. *Plasma Phys. Rep* **2019**, *45*, 637–641.

(41) Summers, H. P., *Atomic data and analysis structure: user manual*; Joint European Torus: Abingdon, 1994.

(42) Reiter, D. The data file AMJUEL: additional atomic and molecular data for EIRENE. *Forschungszentrum Juelich GmbH* **2000**, *52425*.

(43) Reiter, D. The data file HYDHEL: Atomic and Molecular Data for EIRENE. *FZJ* **2002**, *52425*.

(44) Reiter, D.; Giesen, G.; Belitz, H. J.; Eckstein, W. Database for recycling and penetration of neutral helium atoms in the boundary of a fusion plasma. *Forschungszentrum Juelich GmbH* **1992**, *Juel-2605*.

(45) Schneider, R.; Bonnin, X.; Borrass, K.; Coster, D. P.; Kastelewicz, H.; Reiter, D.; Rozhansky, V. A.; Braams, B. J. Plasma Edge Physics with B2-Eirene. *Contributions to Plasma Physics* **2006**, *46*, 3–191.

(46) Kukushkin, A. S.; Pacher, H. D. Neutral recirculation - The key to control of divertor operation. *Nuclear Fusion* **2016**, *56*, 1–14.

(47) Dekeyser, W.; Bonnin, X.; Lisgo, S. W.; Pitts, R. A.; LaBombard, B. Implementation of a 9-point stencil in SOLPS-ITER and implications for Alcator C-Mod divertor plasma simulations. *Nuclear Materials and Energy* **2019**, *18*, 125 –130.

(48) Moscheni, M.; Meineri, C.; Wigram, M.; Carati, C.; De Marchi, E.; Greenwald, M.; Innocente, P.; Labombard, B.; Subba, F.; Wu, H.; Zanino, R. Cross-code comparison of the edge codes SOLPS-ITER, SOLEDGE-2D, and UEDGE in modelling a low-power scenario in the DTT. *Nuclear Fusion* **2022**, *62*, DOI: 10.1088/1741-4326/ac42c4.

(49) Helander, P.; Krasheninnikov, S. I.; Catto, P. J. Fluid equations for a partially ionized plasma. *Physics of Plasmas* **1994**, *1*, 3174–3180.

(50) Horsten, N.; Dekeyser, W.; Samaey, G.; Baelmans, M. Assessment of fluid neutral models for a detached ITER case. *Nuclear Materials and Energy* **2017**, *12*, Proceedings of the 22nd International Conference on Plasma Surface Interactions 2016, 22nd PSI, 869–875.

(51) Rognlien, T.; Milovich, J.; Rensink, M.; Porter, G. A fully implicit, time dependent 2-D fluid code for modeling tokamak edge plasmas. *Journal of Nuclear Materials* **1992**, *196-198*, Plasma-Surface Interactions in Controlled Fusion Devices, 347 –351.

(52) Simonini, R; Corrigan, G; Radford, G; Spence, J; Taroni, A Models and Numerics in the Multi-Fluid 2-D Edge Plasma Code EDGE2D/U. *Contributions to Plasma Physics* **1994**, *34*, 368–373.

(53) Ballinger, S.; Umansky, M.; Kuang, A.; Brunner, D.; LaBombard, B.; Terry, J.; Wigram, M.; the SPARC team Modeling thermal transport in the plasma boundary of SPARC with the UEDGE code, Poster presented remotely at 62nd Annual APS-DPP Virtual Meeting, Nov. 9, 2020.

(54) Ballinger, S. B.; Kuang, A. Q.; Umansky, M. V.; Brunner, D.; Canik, J. M.; Greenwald, M. J.; Lore, J. D.; LaBombard, B.; Terry, J. L.; Wigram, M. Simulation of the SPARC plasma boundary with the UEDGE code. *Nuclear Fusion* **2021**, DOI: 10.1088/1741-4326/ac0c2f.

(55) Grad, H.; Rubin, H. Hydromagnetic Equilibria and Force-Free Fields. *Proceedings of the 2nd UN Conf. on the Peaceful Uses of Atomic Energy* **1958**, *31*.

(56) Shafranov, V. Plasma equilibrium in a magnetic field. *Reviews of Plasma Physics* **1966**, *2*, 103.

(57) Lao, L.; John, H. S.; Stambaugh, R.; Kellman, A.; Pfeiffer, W. Reconstruction of current profile parameters and plasma shapes in tokamaks. *Nuclear Fusion* **1985**, *25*, 1611–1622.

(58) Brown, P. N.; Hindmarsh, A. C. Matrix-Free Methods for Stiff Systems of ODE's. *SIAM Journal on Numerical Analysis* **1986**, *23*, 610–638.

(59) Yousef, S., *Iterative Methods for Sparse Linear Systems*; PWS Pub. Co.: Boston, MA, 1996.

(60) Knoll, D.; Keyes, D. Jacobian-free Newton–Krylov methods: a survey of approaches and applications. *Journal of Computational Physics* **2004**, *193*, 357 –397.

(61) Schneider, R.; Reiter, D.; Zehrfeld, H.; Braams, B.; Baelmans, M.; Geiger, J.; Kastelewicz, H.; Neuhauser, J.; Wunderlich, R. B2-EIRENE simulation of ASDEX and ASDEX-Upgrade scrape-off layer plasmas. *Journal of Nuclear Materials* **1992**, *196-198*, Plasma-Surface Interactions in Controlled Fusion Devices, 810–815.

(62) Reiter, D. Progress in two-dimensional plasma edge modelling. *Journal of Nuclear Materials* **1992**, *196-198*, Plasma-Surface Interactions in Controlled Fusion Devices, 80–89.

(63) Marchand, R. J.; Dumberry, M. CARRE: a quasi-orthogonal mesh generator for 2D edge plasma modelling. *Computer Physics Communications* **1996**, *96*, 232–246.

(64) Kukushkin, A.; Kukushkin, K.; Chin, A.; Stotler, D., DG manual In *SOLPS-ITER User Manual*, Coster, D., Bonnin, X., Eds.; ITER Organization: France, 2023, pp 603–633.

(65) Knoll, D. A.; Catto, P. J.; Krasheninnikov, S. I. A computational investigation of divertor plasma scaling laws. *Physics of Plasmas* **1998**, *5*, 2912–2920.

(66) Masline, R.; Smirnov, R. D.; Krasheninnikov, S. I. Influence of the inverse sheath on divertor plasma performance in tokamak edge plasma simulations. *Contributions to Plasma Physics* **2019**, e201900097.

(67) Komm, M; Ratynskaia, S; Tolias, P; Cavalier, J; Dejarnac, R; Gunn, J. P.; Podolnik, A On thermionic emission from plasma-facing components in tokamak-relevant conditions. *Plasma Physics and Controlled Fusion* **2017**, *59*, 094002.

(68) Rognlien, T.; Rensink, M.; Smith, G. *Users manual for the UEDGE edge-plasma transport code*; tech. rep.; Lawrence Livermore National Lab., Livermore, CA (US), 2000.

(69) Krasheninnikov, S.; Kukushkin, A.; Pshenov, A.; Smolyakov, A.; Zhang, Y. Stability of divertor detachment. *Nuclear Materials and Energy* **2017**, *12*, 1061 –1066.

(70) Lipschultz, B. Review of MARFE phenomena in tokamaks. *Journal of Nuclear Materials* **1987**, *145-147*, 15 –25.

(71) Jaervinen, A. E.; Allen, S. L.; Eldon, D.; Fenstermacher, M. E.; Groth, M.; Hill, D. N.; Leonard, A. W.; McLean, A. G.; Porter, G. D.; Rognlien, T. D.; Samuell, C. M.; Wang, H. Q. ExB Flux Driven Detachment Bifurcation in the DIII-D Tokamak. *Phys. Rev. Lett.* **2018**, *121*, 075001.

(72) Federici, G.; Skinner, C.; Brooks, J.; Coad, J.; Grisolia, C.; Haasz, A.; Hassanein, A.; Philipps, V.; Pitcher, C.; Roth, J. Plasma-material interactions in current tokamaks and their implications for next step fusion reactors. *Nuclear Fusion* **2001**, *41*, 1967–2137.

(73) Stangeby, P., *The Plasma Boundary of Magnetic Fusion Devices*; IOP Publishing: London, 2000.

(74) Krasheninnikov, S.; Smolyakov, A.; Kukushkin, A., *On the Edge of Magnetic Fusion Devices*; Springer Nature: Switzerland, 2020.

(75) Krasheninnikov, S.; Kukushkin, A. Physics of ultimate detachment of a tokamak divertor plasma. *Journal of Plasma Physics* **2017**, *83*, 155830501.

(76) Soukhanovskii, V. A. A review of radiative detachment studies in tokamak advanced magnetic divertor configurations. *Plasma Physics and Controlled Fusion* **2017**, *59*, 064005.

(77) Février, O.; Theiler, C.; Coda, S.; Colandrea, C.; de Oliveira, H.; Duval, B.; Gorno, S.; Labit, B.; Linehan, B.; Maurizio, R.; Perek, A.; Reimerdes, H.; Wüthrich, C.; the TCV Team Detachment in conventional and advanced double-null plasmas in TCV. *Nuclear Fusion* **2021**, *61*, 116064.

(78) Verhaegh, K.; Lipschultz, B.; Harrison, J.; Osborne, N.; Williams, A.; Ryan, P.; Allcock, J.; Clark, J.; Federici, F.; Kool, B.; Wijkamp, T.; Fil, A.; Moulton, D.; Myatra, O.; Thornton, A.; Bosman, T.; Bowman, C.; Cunningham, G.; Duval, B.; Henderson, S.; Scannell, R.; the MAST Upgrade team Spectroscopic investigations of detachment on the MAST Upgrade Super-X divertor. *Nuclear Fusion* **2022**, *63*, 016014.

(79) Umansky, M. V.; Rensink, M. E.; Rognlien, T. D.; LaBombard, B.; Brunner, D.; Terry, J. L.; Whyte, D. G. Assessment of X-point target divertor configuration for power handling and detachment front control. *Nuclear Materials and Energy* **2017**, *12*, 918–923.

(80) Umansky, M.; LaBombard, B.; Brunner, D.; Golfinopoulos, T.; Kuang, A.; Rensink, M.; Terry, J.; Wigram, M.; Whyte, D. Study of passively stable, fully detached divertor plasma regimes attained in innovative long-legged divertor configurations. *Nuclear Fusion* **2019**, *60*, 016004.

(81) Krasheninnikov, S. I.; Pigarov, A. Y.; Knoll, D. A.; Labombard, B.; Lipschultz, B.; Sigmar, D. J.; Soboleva, T. K.; Terry, J. L.; Wising, F. Plasma recombination and molecular effects in tokamak divertors and divertor simulators. *Physics of Plasmas* **1997**, *4*, 1638–1646.

(82) Hsu, W.; Yamada, M.; Barret, P. Experimental simulation of the gaseous tokamak divertor. *Phys. Rev. Lett* **1982**, *49*, 1001–1004.

(83) Fiksel, G.; Kishinevsky, M.; Hershkowitz, N. Experimental simulation of a gaseous plasma collector. *Physics of Fluids B: Plasma Physics* **1990**, *2*, 837–841.

(84) Schmitz, L.; Lehmer, R.; Chevalier, G.; Tynan, G.; Chia, P.; Doerner, R.; Conn, R. Experimental simulation of the gaseous divertor concept in PISCES-A. *J. Nucl. Mater* **1990**, *176–177*, 522–527.

(85) Loarte, A.; Monk, R.; Martín-Solís, J.; Campbell, D.; Chankin, A.; Clement, S.; Davies, S.; Ehrenberg, J.; Erents, S.; Guo, H.; Harbour, P.; Horton, L.; Ingesson, L.; Jäckel, H.; Lingertat, J.; Lowry, C.; Maggi, C.; Matthews, G.; McCormick, K.; O'Brien, D.; Reichle, R.; Saibene, G.;

Smith, R.; Stamp, M.; Stork, D.; Vlases, G. Plasma detachment in JET Mark Idivertor experiments. *Nuclear Fusion* **1998**, *38*, 331.

(86) Pshenov, A.; Kukushkin, A.; Krasheninnikov, S. Energy balance in plasma detachment. *Nuclear Materials and Energy* **2017**, *12*, 948–952,

(87) Kukushkin, A.; Krasheninnikov, S.; Pshenov, A.; Reiter, D. Role of molecular effects in divertor plasma recombination. *Nuclear Materials and Energy* **2017**, *12*, Proceedings of the 22nd International Conference on Plasma Surface Interactions 2016, 22nd PSI, 984–988.

(88) Jaervinen, A.; Allen, S.; Leonard, A. Role of poloidal E x B drift in divertor heat transport in DIII-D. *Contributions to Plasma Physics* **2020**, *60:e201900111*, DOI: 10.1002/ctpp.201900111.

(89) Ma, X.; Wang, H.; Guo, H.; Stangeby, P.; Meier, E.; Shafer, M.; Thomas, D. First evidence of dominant influence of E x B drifts on plasma cooling in an advanced slot divertor for tokamak power exhaust. *Nuclear Fusion* **2021**, *61*, 054002.

(90) Du, H.; Sang, C.; Wang, L.; Bonnin, X.; Sun, J.; Wang, D. Effects of discharge operation regimes and magnetic field geometry on the in-out divertor asymmetry in EAST. *Fusion Engineering and Design* **2016**, *Volumes 109–111*, 1005–1010,

(91) Marchand, R; Dumberry, M; Demers, Y; Cote, C; Clair, G. L.; Larsen, J.-M; Bonnin, X.; Braams, B. Up-down symmetry in double null divertor experiments and magnetic field topology. *Nuclear Fusion* **1995**, *35*, 297–304.

(92) Meyer, H; Carolan, P. G.; Conway, N. J.; Counsell, G. F.; Cunningham, G; Field, A. R.; Kirk, A; McClements, K. G.; Price, M; Taylor, D; the MAST Team Improved H-mode access in connected DND in MAST. *Plasma Physics and Controlled Fusion* **2005**, *47*, 843.

(93) Kuang, A. Q.; Ballinger, S.; Brunner, D.; Canik, J.; Creely, A. J.; Gray, T.; Greenwald, M.; Hughes, J. W.; Irby, J.; LaBombard, B.; et al. Divertor heat flux challenge and mitigation in SPARC. *Journal of Plasma Physics* **2020**, *86*, 865860505.

(94) Krasheninnikov, S.; Kukushkin, A.; Pshenov, A. Divertor plasma detachment. *Physics of Plasmas* **2016**, *23*, 055602.

(95) Krasheninnikov, S. I.; Kukushkin, A. S. 1D model of tokamak scrape-off layer and divertor plasmas: Dimensionless parameters and the results of numerical simulations. *Physics of Plasmas* **2022**, *29*, 122502.

(96) Dudson, B. D.; Allen, J; Body, T; Chapman, B; Lau, C; Townley, L; Moulton, D; Harrison, J; Lipschultz, B The role of particle, energy and momentum losses in 1D simulations of divertor detachment. *Plasma Physics and Controlled Fusion* **2019**, *61*, 065008.

(97) Park, J. S.; Groth, M.; Pitts, R.; Bak, J.-G.; Thatipamula, S.; Juhn, J.-W.; Hong, S.-H.; Choe, W. Atomic processes leading to asymmetric divertor detachment in KSTAR L-mode plasmas. *Nuclear Fusion* **2018**, *58*, 126033.

(98) Wischmeier, M. Simulating Divertor Detachment in the TCV and JET Tokamaks. *PhD Dissertation, EPFL, Switzerland* **2004**.

(99) Pitts, R.; Duval, B.; Loarte, A.; Moret, J.-M.; Boedo, J.; Coster, D.; Furno, I.; Horacek, J.; Kukushkin, A.; Reiter, D.; Rommers, J. Divertor geometry effects on detachment in TCV. *Journal of Nuclear Materials* **2001**, *290-293*, 14th Int. Conf. on Plasma-Surface Interactions in Controlled Fusion Devices, 940–946.

(100) Reimerdes, H.; Duval, B.; Elaian, H.; Fasoli, A.; Février, O.; Theiler, C.; Bagnato, F.; Baquero-Ruiz, M.; Blanchard, P.; Brida, D.; Colandrea, C.; Oliveira, H. D.; Galassi, D.; Gorno, S.; Henderson, S.; Komm, M.; Linehan, B.; Martinelli, L.; Maurizio, R.; Moret, J.-M.; Perek, A.; Raj, H.; Sheikh, U.; Testa, D.; Toussaint, M.; Tsui, C.; Wensing, M.; the TCV team; the EUROfusion MST1 team Initial TCV operation with a baffled divertor. *Nuclear Fusion* **2021**, *61*, 024002.

(101) Stroth, U.; Bernert, M.; Brida, D.; Cavedon, M.; Dux, R.; Huett, E.; Lunt, T.; Pan, O.; Wischmeier, M. Model for access and stability of the X-point radiator and the threshold for marfes in tokamak plasmas. *Nuclear Fusion* **2022**, *62*, DOI: 10.1088/1741-4326/ac613a.

(102) Pan, O.; Bernert, M.; Lunt, T.; Cavedon, M.; Kurzan, B.; Wiesen, S.; Wischmeier, M.; Stroth, U. SOLPS-ITER simulations of an X-point radiator in the ASDEX Upgrade tokamak. *Nuclear Fusion* **2022**, DOI: 10.1088/1741-4326/ac9742.

(103) Cavedon, M.; Kurzan, B.; Bernert, M.; Brida, D.; Dux, R.; Griener, M.; Henderson, S.; Huett, E.; Nishizawa, T.; Lunt, T.; Pan, O.; Stroth, U.; Wischmeier, M.; Wolfrum, E. Experimental investigation of L- and H-mode detachment via the divertor Thomson scattering at ASDEX Upgrade. *Nuclear Fusion* **2022**, *62*, DOI: 10.1088/1741-4326/ac6071.

(104) Lunt, T.; Bernert, M.; Brida, D.; David, P.; Faitsch, M.; Pan, O.; Stieglitz, D.; Stroth, U.; Redl, A. Compact Radiative Divertor Experiments at ASDEX Upgrade and Their Consequences for a Reactor. *Phys. Rev. Lett.* **2023**, *130*, 145102.

(105) Asakura, N.; Hosogane, N.; Itami, K.; Sakasai, A.; Sakurai, S.; Shimizu, K.; Shimada, M.; Kubo, H.; Higashijma, S.; Takenaga, H.; Tamai, H.; Konoshima, S.; Sugie, T.; Masaki, K.; Koide, Y.; Naito, O.; Shirai, H.; Takizuka, T.; Ishijima, T.; Suzuki, S.; Kumagai, A. Role of divertor geometry on detachment and core plasma performance in JT60U. *Journal of Nuclear Materials* **1999**, *266*, 182–188.

(106) Maingi, R.; Mahdavi, M. A.; Jernigan, T. C.; La Haye, R. J.; Hyatt, A. W.; Baylor, L. R.; Whyte, D. G.; Wade, M. R.; Petrie, T. W.; Cuthbertson, J. W.; Leonard, A. W.; Murakami, M.; Snider, R. T.; Stambaugh, R. D.; Watkins, J. G.; West, W. P.; Wood, R. D. Investigation of physical processes limiting plasma density in high confinement mode discharges on DIII-D. *Physics of Plasmas* **1997**, *4*, 1752–1760.

(107) Mahdavi, M.; Osborne, T.; Leonard, A.; Chu, M.; Doyle, E.; Fenstermacher, M.; McKee, G.; Staebler, G.; Petrie, T.; Wade, M.; Allen, S.; Boedo, J.; Brooks, N.; Colchin, R.; Evans, T.; Greenfield, C.; Porter, G.; Isler, R.; Haye, R. L.; Lasnier, C.; Maingi, R.; Moyer, R.; Schaffer, M.; Stangeby, P.; Watkins, J.; West, W.; Whyte, D.; Wolf, N. High performance H mode plasmas at densities above the Greenwald limit. *Nuclear Fusion* **2002**, *42*, 52.

(108) Weisberg, D. B.; Leuer, J.; McClenaghan, J.; Yu, J. H.; Wehner, W.; McLaughlin, K.; Abrams, T.; Barr, J.; Grierson, B.; Lyons, B.; MacDonald, J. R.; Meneghini, O.; Petty, C. C.; Pinsker, R. I.; Sinclair, G.; Solomon, W. M.; Taylor, T.; Thackston, K.; Thomas, D.; van Compernolle, B.; VanZeeland, M.; Zeller, K. An Integrated Design Study for an Advanced Tokamak to Close Physics Gaps in Energy Confinement and Power Exhaust. *Fusion Science and Technology* **2023**, *0*, 1–25.

(109) Menard, J.; Brown, T.; El-Guebaly, L.; Boyer, M.; Canik, J.; Colling, B.; Raman, R.; Wang, Z.; Zhai, Y.; Buxton, P.; Covele, B.; D'Angelo, C.; Davis, A.; Gerhardt, S.; Gryaznevich, M.; Harb, M.; Hender, T.; Kaye, S.; Kingham, D.; Kotschenreuther, M.; Mahajan, S.; Maingi, R.; Marriott, E.; Meier, E.; Mynsberge, L.; Neumeyer, C.; Ono, M.; Park, J.-K.; Sabbagh, S.; Soukhanovskii, V.;

Valanju, P.; Woolley, R. Fusion nuclear science facilities and pilot plants based on the spherical tokamak. *Nuclear Fusion* **2016**, *56*, 106023.

(110) Post, D. E. A review of recent developments in atomic processes for divertors and edge plasmas. *Journal of Nuclear Materials* **1995**, *220-222*, 143–157.

(111) Wijkamp, T.; Allcock, J.; Feng, X.; Kool, B.; Lipschultz, B.; Verhaegh, K.; Duval, B.; Harrison, J.; Kogan, L.; Lonigro, N.; Perek, A.; Ryan, P.; Sharples, R.; Classen, I.; Jaspers, R.; the MAST Upgrade team Characterisation of detachment in the MAST-U Super-X divertor using multi-wavelength imaging of 2D atomic and molecular emission processes. *Nuclear Fusion* **2023**, *63*, 056003.

(112) Masline, R.; Krasheninnikov, S. Energy and particle balance during plasma detachment in a long-leg divertor configuration. *Nuclear Fusion* **2023**, *63*, 066017.

(113) Sang, C. F.; Stangeby, P. C.; Guo, H. Y.; Leonard, A. W.; Covele, B; Lao, L. L.; Moser, A. L.; Thomas, D. M. SOLPS modeling of the effect on plasma detachment of closing the lower divertor in DIII-D. *Plasma Physics and Controlled Fusion* **2016**, *59*, 025009.

(114) Krasheninnikov, S.; Kukushkin, A.; Pistunovich, V.; Pozharov, V. Self-sustained oscillations in the divertor plasma. *Nuclear Fusion* **1987**, *27*, 1805.

(115) Kukushkin, A. S.; Pacher, H. D. Divertor modelling and extrapolation to reactor conditions. *Plasma Physics and Controlled Fusion* **2002**, *44*, 931.

(116) Pshenov, A. A.; Kukushkin, A. S.; Krasheninnikov, S. I. On detachment asymmetry and stability. *Physics of Plasmas* **2017**, *24*, 072508, DOI: 10.1063/1.4991402.

(117) Sytova, E.; Coster, D.; Senichenkov, I.; Kaveeva, E.; Rozhansky, V.; Voskoboynikov, S.; Veselova, I.; Bonnin, X. P. Derivation of the friction and thermal force for SOLPS-ITER multicomponent plasma modeling. *Physics of Plasmas* **2020**, *27*, DOI: 10.1063/5.0006607.

(118) Makarov, S. O.; Coster, D. P.; Rozhansky, V. A.; Stepanenko, A. A.; Zhdanov, V. M.; Kaveeva, E. G.; Senichenkov, I. Y.; Bonnin, X. Equations and improved coefficients for parallel transport in multicomponent collisional plasmas: Method and application for tokamak modeling. *Physics of Plasmas* **2021**, *28*, 062308.

(119) Makarov, S.; Coster, D.; Kaveeva, E.; Rozhansky, V.; Senichenkov, I.; Veselova, I.; Voskoboynikov, S.; Stepanenko, A.; Bonnin, X.; Pitts, R. Implementation of SOLPS-ITER code with new Grad–Zhdanov module for D–T mixture. *Nuclear Fusion* **2023**, *63*, 026014.

(120) Pitts, R. A.; Bonnin, X.; Escourbiac, F.; Frerichs, H.; Gunn, J. P.; Hirai, T.; Kukushkin, A. S.; Kaveeva, E.; Miller, M. A.; Moulton, D.; Rozhansky, V.; Senichenkov, I.; Sytova, E.; Schmitz, O.; Stangeby, P. C.; De Temmerman, G.; Veselova, I.; Wiesen, S. Physics basis for the first ITER tungsten divertor. *Nuclear Materials and Energy* **2019**, *20*, 100696.

(121) Senichenkov, I. Y.; Kaveeva, E. G.; Sytova, E. A.; Rozhansky, V. A.; Voskoboynikov, S. P.; Veselova, I. Y.; Coster, D. P.; Bonnin, X; Reimold, F; the ASDEX-Upgrade Team On mechanisms of impurity leakage and retention in the tokamak divertor. *Plasma Physics and Controlled Fusion* **2019**, *61*, 045013.

(122) Reimold, F.; Wischmeier, M.; Kukushkin, A.; Reiter, D.; Bernert, M. In *26th IAEA Fusion Energy Conference*, 2018, pp 6–22.

(123) Kaveeva, E.; Rozhansky, V.; Veselova, I.; Senichenkov, I.; Giroud, C.; Pitts, R. A.; Wiesen, S.; Voskoboynikov, S. SOLPS-ITER drift modelling of JET Ne and N-seeded H-modes. *Nuclear Materials and Energy* **2021**, *28*, 101030.

(124) Sytova, E.; Pitts, R. A.; Kaveeva, E.; Bonnin, X.; Coster, D.; Rozhansky, V.; Senichenkov, I.; Veselova, I.; Voskoboynikov, S.; Reimold, F. Comparing N versus Ne as divertor radiators in ASDEX-upgrade and ITER. *Nuclear Materials and Energy* **2019**, *19*, 72–78.

(125) Casali, L.; Eldon, D.; Boedo, J. A.; Leonard, T.; Covele, B. Neutral leakage, power dissipation and pedestal fueling in open vs closed divertors. *Nuclear Fusion* **2020**, *60*, DOI: 10.1088/1741-4326/ab8d06.

(126) Casali, L.; Eldon, D.; McLean, A.; Osborne, T.; Leonard, A.; Grierson, B.; Ren, J. Impurity leakage and radiative cooling in the first nitrogen and neon seeding study in the closed DIII-D SAS configuration. *Nuclear Fusion* **2022**, *62*, DOI: 10.1088/1741-4326/ac3e84.

(127) Giroud, C.; Maddison, G.; McCormick, K.; Beurskens, M.; Brezinsek, S.; Devaux, S.; Eich, T.; Frassinetti, L.; Fundamenski, W.; Groth, M.; Huber, A.; Jachmich, S.; Järvinen, A.; Kallenbach, A.; Krieger, K.; Moulton, D.; Saarelma, S.; Thomsen, H.; Wiesen, S.; Alonso, A.; Alper, B.; Arnoux, G.; Belo, P.; Boboc, A.; Brett, A.; Brix, M.; Coffey, I.; de la Luna, E.; Dodt, D.; Vries,

P. D.; Felton, R.; Giovanozzi, E.; Harling, J.; Harting, D.; Hawkes, N.; Hobirk, J.; Jenkins, I.; Joffrin, E.; Kempenaars, M.; Lehnen, M.; Loarer, T.; Lomas, P.; Mailloux, J.; McDonald, D.; Meigs, A.; Morgan, P.; Nunes, I.; van Thun, C. P.; Riccardo, V.; Rimini, F.; Sirinnelli, A.; Stamp, M.; Voitsekhovitch, I.; Contributors, J. E. Integration of a radiative divertor for heat load control into JET high triangularity ELMy H-mode plasmas. *Nuclear Fusion* **2012**, *52*, 063022.

(128) Kallenbach, A.; Bernert, M.; Dux, R.; Casali, L.; Eich, T.; Giannone, L.; Herrmann, A.; McDermott, R.; Mlynek, A.; Müller, H. W.; Reimold, F.; Schweinzer, J.; Sertoli, M.; Tardini, G.; Treutterer, W.; Viezzer, E.; Wenninger, R.; Wischmeier, M. Impurity seeding for tokamak power exhaust: From present devices via ITER to DEMO. *Plasma Physics and Controlled Fusion* **2013**, *55*, DOI: 10.1088/0741-3335/55/12/124041.

(129) Loarte, A.; Hughes, J. W.; Reinke, M. L.; Terry, J. L.; LaBombard, B.; Brunner, D.; Greenwald, M.; Lipschultz, B.; Ma, Y.; Wukitch, S.; Wolfe, S. High confinement/high radiated power H-mode experiments in Alcator C-Mod and consequences for International Thermonuclear Experimental Reactor (ITER) QDT=10 operationa). *Physics of Plasmas* **2011**, *18*, 056105, DOI: 10.1063/1.3567547.

(130) Kallenbach, A.; for the ASDEX Upgrade Team; the EUROfusion MST1 Team Overview of ASDEX Upgrade results. *Nuclear Fusion* **2017**, *57*, 102015.

(131) Reinke, M. L. Heat flux mitigation by impurity seeding in high-field tokamaks. *Nuclear Fusion* **2017**, *57*, DOI: 10.1088/1741-4326/aa5145.

(132) Wensing, M; Duval, B. P.; Février, O; Fil, A; Galassi, D; Havlickova, E; Perek, A; Reimerdes, H; Theiler, C; Verhaegh, K; Wischmeier, M; the EUROfusion MST1 team; the TCV team SOLPS-ITER simulations of the TCV divertor upgrade. *Plasma Physics and Controlled Fusion* **2019**, *61*, 085029.

(133) Fasoli, A.; Reimerdes, H.; Alberti, S.; Baquero-Ruiz, M.; Duval, B.; Havlikova, E.; Karpushov, A.; Moret, J.-M.; Toussaint, M.; Elaian, H.; Silva, M.; Theiler, C.; Vaccaro, D.; the TCV team TCV heating and divertor upgrades. *Nuclear Fusion* **2019**, *60*, 016019.

(134) Pshenov, A. A.; Kukushkin, A. S.; Krasheninnikov, S. I. Influence of Cross-Field Transport in a Divertor on Seeded Impurity Radiation and Divertor Plasma Detachment. *Plasma Phys. Rep* **2020**, *46*.

(135) Hudoba, A.; Newton, S.; Voss, G.; Cunningham, G.; Henderson, S. Divertor optimisation and power handling in spherical tokamak reactors. *Nuclear Materials and Energy* **2023**, 101410.

(136) Masline, R.; Krasheninnikov, S. Mechanisms behind impurity spreading in a channeled, long-leg divertor configuration. *Physics of Plasmas* **2023**, *Submitted*.

(137) Keilhacker, M.; Simonini, R.; Taroni, A.; Watkins, M. Scrape-off layer model for the study of impurity retention in the pumped divertor planned for JET. *Nuclear Fusion* **1991**, *31*, 535.

(138) Igitkhanov, Y. L. Impurity Transport at Arbitrary Densities in the Divertor Plasma. *Contributions to Plasma Physics* **1988**, *28*, 477–482.

(139) Kotov, V. SOLPS4.3 short handbook (Draft), 2012.

(140) Huba, J. D., *NRL plasma formulary*; 98-358; Naval Research Laboratory: 1998; Vol. 6790.

(141) Spitzer, L.; Härm, R. Transport Phenomena in a Completely Ionized Gas. *Phys. Rev.* **1953**, *89*, 977–981.